A-0187
a-15

ONE.0016

9/15

Memoria de Inundación por Tsunami en la Bahía de Quintero (Texto en Inglés).

Patricio Winckler Grez

REPUBLICA DE CHILE
OFICINA NACIONAL DE EMERGENCIA
BIBLIOTECA
CENTRO NACIONAL DE DOCUMENTACION
PROTECCION CIVIL

Diciembre 2001

INV.811

TSUNAMI RISK ASSESSMENT IN QUINTERO BAY, CHILE.

PATRICIO WINCKLER GREZ

DECEMBER 2001

REPUBLICA DE CHILE - MINISTERIO DEL INTERIOR
OFICINA NACIONAL DE EMERGENCIA
BIBLIOTECA
CENTRO NACIONAL DE DOCUMENTACION
PROTECCION CIVIL

This thesis is presented in partial fulfilment of the assessment requirements of the MSc. in Environmental Technology of the University of Wolverhampton.

Supervisor: Dr. Paul Giess. University of Wolverhampton

Assessor: Dr. Adrian Neal. University of Wolverhampton

To my parents,
for the devoted support during the work

and to Finland,
the country that gave me strength to develop this project.

"A veces, cuando ya rodaron
los muros y los techos entre el polvo y las llamas,
entre los gritos y el silencio, cuando ya todo
parecía definitivamente quieto en la muerte, salió
del mar, como el último espanto, la gran ola, la
inmensa mano verde que, alta y amenazante,
sube como una torre de venganza barriendo la
vida a su alcance."

"Confieso que he vivido", PABLO NERUDA

Chilean Nobel Price, 1971

Abastecimientos

From: "Patricio Winckler G." <pwinckler@prdw.co.cl>
To: <onemicompras@terra.cl>
Sent: Miércoles, 13 de Marzo de 2002 05:14 p.m.
Attach: Chapter 1 - Introduction.zip; Abstract and Index.zip
Subject: RV: Evaluación de Riesgo de Tsunami en
Para: Sra. Carmen Fernández
Jefa de Protección Civil - ONEMI

Estimada Sra. Carmen

Esta mañana visité el Centro de Documentación de la ONEMI con el propósito de buscar el *Carta de Inundación por Tsunami en Iquique*. Por esas cosas de la vida, terminamos conversando con la Sra. Estrella del Valle sobre mis actividades académicas y me comprometí a hacerle llegar una copia de mi tesis de maestría (MSc. in Environmental technology and Management, de la Universidad de Wolverhampton, Inglaterra) que versa sobre la evaluación de riesgo de tsunami en Quintero (Tsunami Risk Assessment in Quintero, Chile).

Adjunto envío dicho documento, que imagino le interesará, para que lo examine y deje a disposición de la comunidad.

Si es de vuestro interés, podemos conversar del tema cuando usted disponga.

Atentamente,

Patricio

Patricio Winckler Grez

PRDW SudAmérica Ingenieros Ltda.
Consultores en Ingeniería Hidráulica y Marítima
Fidel Oteíza 1941, Of. 301
Providencia, Santiago
CHILE
tel: +56 (2) 374 9811
tel/fax: +56 (2) 225 0591
e-mail: pwinckler@prdw.co.cl
web: www.prdw.co.za

DECLARATION

This work has not previously been presented in any form to the university or to any other institutional body whether for assessment or other purposes. Save for any express acknowledgements, references and/or bibliographies cited in the work, I confirm that the intellectual content of the work is the result of my own effort and of no other person.

It is acknowledged that the author of this project work shall own copyright. However, by submitting this copyright work for assessment, the author grants to the University a perpetual royalty-free licence to do all or any of those things referred to in section 16(i) of the Copyright, Designs and Patents Act 1988 (viz; to copy work; to issue to the public; to perform or show or play the work in public; to broadcast the work or make an adaptation of the work).

ABSTRACT

The developing importance of Quintero harbour and the extensive land use in the bay have prompted the assessment of tsunami risk in order to better understand the phenomena and risks involved and to advise upon mitigating measures for the area. This report presents the theory and technique for the evaluation of the potential effects of tsunamis striking the area, as part of an extensive research commissioned by the Chilean Hydrographic and Oceanographic Service (SHOA) which is currently evaluating tsunami risk in the Chilean harbours.

To study tsunami hydrodynamics, TUNAMI-N code was used[1]. This is a numerical facility for the modelling of near-field tsunamis, developed by Dr. Nuobo Shuto in Tohoku University, Japan (1997). It is based on a leap frog finite difference scheme and includes the generation, propagation and run-up of tsunami waves by means of the shallow water wave theory. The seismic events were selected from historical records of earthquakes occurred in the area. Results are presented as a tsunami flooding map, velocity fields and wave height time series, within 3-hours simulations. TUNAMI-N code in combination with Matlab 5.3 graphical facilities showed an efficient performance concerning time and memory consumption.

Results show that the North-eastern portion of the bay would be severely affected by potentially destructive tsunamis (Mo $5x10^{21}$) with run-ups of up to 8 m and velocities of 8m/s. Downtown Quintero is relatively protected by Peninsula Los Molles and would not be very damaged by these events. Minor tsunamis (10^{21} $5x10^{21}$) signify negligible impacts with run-ups of about 2 m and maximum velocities of 1m/s. It is concluded that flooded areas are strongly dependent on the seismic moment of the triggering earthquake (Mo) and, until improved information about seismic features in Central Chile is available, obtained results provide a good approach to evaluate tsunami-flooding levels.

A site-specific set of mitigating measures includes soil stability improvement, storage tanks anchoring and the protection, or relocation of critical lifelines and buildings in Puerto Ventanas. Terminales Oxiquim require minor mitigating measures because of its safe location. Providing frictional characteristics to the coastline, by landscaping with tsunami forests or drainage nets, would be an economic and sustainable alternative to mitigate inundation risks in residential areas. It is recommended to prepare a communication plan in order to encourage public awareness of the tsunami threat.

---

[1] *TUNAMI-N is the acronym for Tohoku University's Numerical Analysis Model for Investigation of Near-Field Tsunamis.*

CONTENTS

		PAGE
CHAPTER 1	**INTRODUCTION**	
1.1	GENERAL REMARKS	1.1
1.2	SCOPE OF THE REPORT	1.3
1.3	QUINTERO BAY	1.4
1.4	LITERATURE REVIEW	1.7
1.4.1	HISTORICAL REMARKS	1.7
1.4.2	SEISMICITY IN THE CHILE-PERU TRENCH	1.9
1.4.3	TSUNAMI MODELS	1.14
CHAPTER 2	**TSUNAMI HYDRODYNAMICS**	
2.1	TSUNAMI WAVE GENERATION	2.1
2.1.1	SOURCE MECHANISM	2.1
2.1.2	OTHER TYPES OF SURFACE WAVES	2.3
2.2	PROPAGATION IN OPEN OCEAN	2.4
2.2.1	GENERAL REMARKS	2.4
2.2.2	ENERGY LOSSES AND SPREADING	2.5
2.2.3	REFRACTION	2.6
2.3	COAST AMPLIFICATION AND RUN-UP	2.7
2.3.1	GENERAL REMARKS	2.7
2.3.2	SHOALING EFFECT	2.7
2.3.3	THE EFFECT OF BATHYMETRY	2.9
2.3.4	RESONANCE	2.9
2.3.5	DIFRACTION	2.10
2.3.6	BREAKING MECHANISM	2.10
2.3.7	RUN-UP VELOCITY	2.11
2.4	TSUNAMI AND RELATED PARAMETERS	2.12
2.4.1	GENERAL REMARKS	2.12
2.4.2	WAVE HEIGHT	2.12
2.4.3	RUN-UP	2.13
2.4.4	CELERITY	2.15
2.4.5	WAVELENGTH	2.15
2.4.6	PERIOD	2.16
2.4.7	ESTIMATED ARRIVAL TIME	2.16
2.4.8	TSUNAMI MAGNITUDE	2.17
2.4.9	SEISMIC MOMENT	2.17
CHAPTER 3	**METHODOLOGY**	
3.1	GENERAL REMARKS	3.1
3.2	MATHEMATICAL MODEL	3.6
3.3	NUMERICAL MODEL	3.9
3.3.1	LINEAR LONG WAVE THEORY	3.10
3.3.2	NON LINEAR SHALLOW WATER THEORY	3.13
3.3.3	INITIAL CONDITIONS	3.16
3.3.4	BOUNDARY CONDITIONS	3.16
3.4	SOURCES OF DATA	3.19
3.4.1	BATHYMETRY	3.19
3.4.2	TOPOGRAPHY	3.19

CHAPTER 3 METHODOLOGY PAGE

3.4.3 SEISMOLOGIC DATA 3.20
3.4.4 CASES ANALYSED 3.24
3.5 GRIDS GENERATION 3.26
3.5.1 DIGITATION OF GRID A 3.30
3.5.2 DIGITATION OF GRIDS B AND C 3.31
3.5.3 DIGITATION OF GRID D 3.32
3.6 CALIBRATION 3.33

CHAPTER 4 RESULTS

4.1 GENERAL REMARKS 4.1
4.2 SENSITIVITY ANALYSIS 4.2
4.3 TIME HISTORY 4.8
4.3.1 GRID A 4.8
4.3.2 GRID D 4.13
4.4 MAXIMUM ELEVATIONS AND VELOCITY 4.23
4.5 TSUNAMI FLOODING MAP 4.28

CHAPTER 5 CONCLUSIONS

CHAPTER 6 REFERENCES

APPENDICES

A.1 TYPE OF DAMAGE CAUSED BY TSUNAMIS A1.1
A.2 TSUNAMI WARNING NETWORK A2.1
A.3 SHALLOW WATER THEORY - INTEGRAL VERSION A3.1
A.4 GRIDS GENERATION A4.1
A.5 PROGRAMS AND ALGORITHMS A5.1
A.5.1 FILTRO.FOR A5.1
A.5.2 NODOS.M A5.2
A.5.3 BIVAR.FOR A5.4
A.5.4 INTERPAB.FOR A5.30
A.5.5 SMYLIE.FOR A5.34
A.5.6 TUNAMI.FOR A5.37
A.5.7 AANIMATION.M A5.53
A.5.8 DANIMATION.M A5.54
A.5.9 VECTOR.M A5.55
A.6 RUPTURE ZONE IN GRID A A6.1
A.7 TIME HISTORY IN GRID D A7.1
A.8 COASTAL STRUCTURES IN QUINTERO BAY A8.1
A.9 GLOSSARY A9.1
A.10 SUMMARY OF TSUNAMIS IN CHILE A10.1
A.11 TOPOGRAPHIC AND HYDROGRAPHIC MAPS A11.1

LIST OF FIGURES

CHAPTER 1 INTRODUCTION

		PAGE
1.1	CENTRAL CHILE COASTAL ZONE	1.4
1.2	QUINTERO BAY	1.5
1.3	AERIAL VIEW OF QUINTERO	1.6
1.4	TECHTONIC PLATES IN SOUTH AMERICA	1.9
1.5	SUBDUCTION ALONG THE CHILE-PERU TRENCH	1.10
1.6	SPACE-TIME DIAGRAM OF CENTRAL CHILE EARTHQUAKES	1.13

CHAPTER 2 TSUNAMI HYDRODYNAMICS

2.1	ENERGY DENSITY SPECTRUM OF SURFACE WAVES	2.3
2.2	REFRACTION EFFECT ON IRREGULAR COASTS	2.6
2.3	THEORETICAL WAVE TRANSFORMATION	2.8
2.4	TSUNAMI PARAMETERS	2.12
2.5	RUN-UP V/S EPICENTRAL DISTANCE FOR GREAT CHILEAN AND PERUVIAN TSUNAMIS	2.14

CHAPTER 3 METHODOLOGY

3.1	ALTIMETRIC REFERENCE LEVEL	3.4
3.2	CO-ORDINATE LEVEL	3.6
3.3	GRID POINTS ARRENGEMENT IN THE LEAP-FROG SCHEME	3.11
3.4	THE LEAP FROG SCHEME. LINEAR LONG WAVE THEORY	3.12
3.5	THE LEAP FROG SCHEME. NON-LINEAR LONG WAVE THEORY	3.15
3.6	OFFSHORE BOUNDARY CONDITIONS	3.17
3.7	RUN-UP BOUNDARY CONDITIONS	3.18
3.8	RUPTURE PARAMETERS	3.20
3.9	DISTRIBUTION OF UPLIFT AND SUBSIDENCE IN THE SOURCE REGION (GRID A). CASE 1730-1	3.23
3.10	PARTIAL VIEW OF GRIDS A, B, C AND GRID D	3.28
3.11	GRID A	3.30
3.12	GRID C	3.31
3.13	GRID B	3.31
3.14	GRID D	3.32
3.15	ORIGINAL 1985 TSUNAMI RECORD IN VALPARAISO	3.33

CHAPTER 4 RESULTS

4.1	LOCATION OF THE MARIGRAM	4.2
4.2	MAXIMUM ELEVATIONS IN GRID POINT (5,98), GRID D	4.3
4.3	MARIGRAMS FOR CASES 1730-1, 1730-2 AND 1730-3. S1	4.4
4.4	MAXIMUM HEIGHT V/S DEPTH	4.5
4.5	MARIGRAMS FOR CASES 1730-1, 1730-4 AND 1730-5. S1	4.5
4.6	MARIGRAMS FOR CASES 1730-1, 1730-6 AND 1730-7. S1	4.6
4.7	MARIGRAMS FOR CASES 1730-1 AND 1730-8. S1.	4.7
4.8	TIME HISTORY IN GRID A. T=0 min	4.9
4.9	TIME HISTORY IN GRID A. T=5 min	4.9
4.10	TIME HISTORY IN GRID A. T=10 min	4.9
4.11	TIME HISTORY IN GRID A. T=15 min	4.10
4.12	TIME HISTORY IN GRID A. T=20 min	4.10
4.13	TIME HISTORY IN GRID A. T=25 min	4.10

CHAPTER 4 **RESULTS**

		PAGE
4.14	TIME HISTORY IN GRID A. T =30 min	4.11
4.15	TIME HISTORY IN GRID A. T =35 min	4.11
4.16	TIME HISTORY IN GRID A. T =40 min	4.11
4.17	TIME HISTORY IN GRID A. T =45 min	4.12
4.18	TIME HISTORY IN GRID A. T =50 min	4.12
4.19	TIME HISTORY IN GRID A. T =55 min	4.12
4.20	LOCATION OF THE MARIGRAMS	4.13
4.21	HYPOTHETICAL MARIGRAMS ALONG QUINTERO BAY	4.14
4.22	VELOCITY FIELDS. T=0 min	4.15
4.23	SURFACE ELEVATIONS. T= 20 min	4.15
4.24	VELOCITY FIELDS. T=25 min	4.15
4.25	SURFACE ELEVATIONS. T=40 min	4.16
4.26	VELOCITY FIELDS. T =45 min	4.16
4.27	SURFACE ELEVATIONS. T=50 min	4.16
4.28	VELOCITY FIELDS. T=75 min	4.17
4.29	SURFACE ELVATIONS. T=80 min	4.17
4.30	VELOCITY FIELDS. T=100 min	4.17
4.31	SURFACE ELEVATIONS. T =105 min	4.18
4.32	VELOCITY FIELDS. T =115 min	4.18
4.33	SURFACE ELEVATIONS. T =125 min	4.18
4.34	VELOCITY FIELDS. T =130 min	4.19
4.35	SURFACE ELEVATIONS. T =135 min	4.19
4.36	VELOCITY FIELDS. T =140 min	4.19
4.37	WAVE HEIGHT V/S VELOCITY IN GRID D (40,30)	4.20
4.38	3D VIEW OF 1730 TSUNAMI IN QUINTERO BAY. T=0 min	4.21
4.39	3D VIEW OF 1730 TSUNAMI IN QUINTERO BAY. T=20 min	4.22
4.40	3D VIEW OF 1730 TSUNAMI IN QUINTERO BAY. T=30 min	4.22
4.41	FLOODING LINE 1730. CASE 1730-10	4.26
4.42	FLOODING LINE 1906. CASE 1906-1	4.26
4.43	FLOODING LINE 1985. CASE 1985-1	4.26
4.44	FLOODING LINES FOR THE 1730, 1906 AND 1985 TSUNAMIS	4.27
4.45	TSUMANI FLOODING MAP	4.29

LIST OF TABLES

CHAPTER 1 INTRODUCTION		PAGE
1.1	TSUNAMIS IN QUINTERO	1.6
1.2	TSUNAMI MODELS IN CHILEAN HARBOURS	1.8
1.3	GREAT EARTHQUAKES IN QUINTERO AREA	1.12
CHAPTER 2 TSUNAMI HYDRAULICS		
2.1	TSUNAMI CELERITY, WAVELENGTH AND PERIOD	2.16
2.2	TSUNAMI GRADE SCALE OF IIDA AND IMAMURA	2.17
2.3	TSUNAMI POTENTIAL AS A FUNCTION OF THE SEISMIC MOMENT	2.18
CHAPTER 3 METHODOLOGY		
3.1	HYDROGRAPHIC CHARTS	3.19
3.2	DEFINITION OF THE RUPTURE ZONE PARAMETERS	3.20
3.3	PARAMETERS OF THE 8TH JULY 1730 EARTHQUAKE	3.21
3.4	PARAMETERS OF THE 1906 AND 1985 EARTHQUAKES	3.22
3.5	CASES OF ANALYSIS	3.24
3.6	MAXIMUM UPLIFT ON EACH CASE	3.25
3.7	COURANT'S STABILITY CONDITION	3.27
3.8	DIMENSIONS OF THE GRIDS	3.29
3.9	SPACE INCREMENTS AND GRID POINTS	3.29
CHAPTER 4 RESULTS		
4.1	SENSITIVITY OF WAVE HEIGHT TO INPUT VARIABLES	4.2
4.2	PARAMETERS FOR THE 1730 EARTHQUAKE	4.7
4.2	MAXIMUM HEIGH AND SPEED IN STATION S2	4.23
4.3	MAXIMUM HEIGH AND SPEED IN STATION S3	4.24
4.4	MAXIMUM HEIGH AND SPEED IN STATION S4	4.25

ACKNOWLEDGEMENTS

This project was possible with the constant support of the Hydrographic and Oceanographic Service of the Chilean Navy. I would like to give special thanks to Dr. Rodrigo Nuñez, Director of the Department of Oceanography, to Prof. Dante Gutierrez, chief of the CITSU Project and Cecilia Zelaya, who has contributed in providing with figures and guidance for the elaboration of the document.

With special emphasis, I would like to thank Prof. Eng. Javier Vásquez, from Universidad Técnica Federico Santa María, who assumed the supervision of the project in Chile and guided me throughout my initial training in coastal and maritime engineering.

I would like to express my sincere gratitude and appreciation to Dr. Roger Dackombe for the facilities provided during the Master courses in the University of Wolverhampton and to Dr. Paul Giess and Dr. Adrian Neal who assumed the tutorial of the project in the institution.

I am grateful also to the many experts who had devoted their lives to the research of Tsunamis. Without their contributions, it would have been impossible to conduct this work to a safe harbour.

CHAPTER 1
INTRODUCTION

1.1 GENERAL REMARKS

A tsunami is the Japanese name for the gravity wave system formed in the sea following any large-scale, short duration disturbance of the free surface (Van Dorn, 1968). The phenomenon is associated primarily with submarine earthquakes, landslides or underwater volcanic eruptions occurring below or near the ocean floor but may be caused by other mechanisms as well. These waves may reach extremely long lengths and periods and have sufficient energy to travel across entire oceans. They behave as ordinary gravity waves - with typical periods in the range of 5 minutes to 2 hours - and increase their height as they approach the coast. Because of their eventual catastrophic destructiveness, tsunamis have important impacts on human, social and economic sectors of coastal communities. This is especially relevant for a country such as Chile that holds a 4.500 km coastline in the Pacific Ring of Fire (a series of mountain chains, deep ocean trenches and island arcs in the margins of the Pacific Ocean).

The damage may result in life losses, flooding and damage to public utilities such as transport systems, energy networks and water supply installations. Coastal, marine and port infrastructure is also expected to collapse under tsunami attack. Drifting materials and substances may cause environmental pollution and the outbreak of epidemic diseases that could be critic in populated areas.

Tsunami is a Japanese coupled-word meaning ***harbour wave*** (represented by the characters ***tsu***, meaning harbour and ***nami***, meaning wave). In the past, tsunamis were referred to as tidal waves by the public and as seismic sea waves by the scientific community. The term tidal wave is incorrect since tsunamis are unrelated to the tide (mechanism that results from the unbalanced gravitational influences of the moon, sun and planets, among other effects). The term seismic sea wave is also misleading since it implies an earthquake-related generation mechanism, omitting the fact that tsunamis can also be caused by non-seismic events, such as landslides, a meteorite impact or other.



Historically, there has been a quite frequent occurrence of destructive tsunamis in the Pacific Ocean, as a consequence of the many earthquakes that occur along the Ring of Fire. It is estimated that at least four considerable tsunamis take place within a three years period around the world, 60-70% of which are located in the Pacific Basin (Godoy and Monge, 1975). Newmark and

Rosenblueth (1971) estimated that 62% of historical tsunamis occurred in the Pacific Ocean, 20% in the Indian Ocean, 9% in the Mediterranean Sea and 9% in the northern Atlantic Ocean.

The deep ocean trenches located in Japan, Alaska, and South America are known for their seismic activity, accounting for more than 500 recorded tsunamis and 50.000 life losses only in the past century. One of the first documented events occurred in June 15TH 1896 along the Japanese coast; the main waves reached 30 m, resulting in a legacy of 27.000 deaths and 10.000 houses destroyed (Newmark and Rosenblueth, 1971). The Alaskan Earthquake of March 28TH 1964 registered 8.3 in Richter scale and affected a vast extension of North America. The earthquake caused areas to be lifted by as much as 10 m while many other areas subsided. The tsunami produced 7 m waves from Crescent City to Monterey and intensely affected Alaska, Northern California and Hawaii. The 1992 Nicaragua tsunami generated a devastating effect with localised damage to coastal communities. In July 1993, a tsunami generated in the Sea of Japan killed over 120 people, and caused damage in Korea and Russia. This episode caused an impact to the regional area in the proximity of the earthquake, similar to the tsunamis which took place in Indonesia (1992 and 1994) and the Philippines (1994).

Since 1562, more than 30 near-field tsunamis impacted Chilean coast, producing, in some cases, the complete devastation of cities such as Arica in 1604 and Concepción in 1751. In both episodes, damage was of such magnitude that was necessary to relocate both cities (Godoy and Monge, 1975). On May 22ND 1960, a Pacific-wide tsunami was triggered off the Chilean coast by an earthquake of 8.6° in the Richter scale. The epicentre was located in 39.5°S and 74.5°W, with a focal depth of 33 km and an estimated rupture length of 900 km. Local people, fearing the earthquake, took small boats to escape the shaking. The tsunami arrived around 15 min after the earthquake and, upon the return of the sea in a thunderous breaker, all boats collapsed. The disaster claimed 330 lives in Chile, 61 in Hawaii, 20 in Philippines and 180 in Japan, with an estimated material loss of 30 millions USD. The earthquake is the largest recorded by instruments in modern times and is considered as an emblematic event among the scientific community.

The great destruction caused by both the 1960 Chilean and 1964 Alaskan Earthquake prompted a number of countries to encourage bilateral co-operation and tsunami research. In Chile, the Hydrographic and Oceanographic Service of the Chilean Navy[1] (SHOA) has developed the CITSU project ("Processing of Inundation Maps by Tsunamis for the Chilean Coast) under which the present research is carried out.

---

[1] *The official name of the institution is Servicio Hidrográfico y Oceanográfico de la Armada de Chile and will be referred in the report under the acronym SHOA.*

1.2 SCOPE OF THE REPORT

The following report presents the theory and methodology for the assessment of tsunami risk associated to a potential near-field tsunami (i.e. tsunami from a nearby source, generally less than 200 km away from a particular site) in the coastal area of Quintero Bay, Chile. The development pressures in the area have motivated the investigation in order to propose measures to diminish the tsunami risk (i.e. the exposure to loss, or injury caused by the tsunami hazard) posed to the coastal communities and port facilities in the harbour. The hypothesis under which this project is carried out is the following:

Since central Chile has been impacted by a series of large earthquakes of $M_O > 5x10^{21}$ Nm[2] during historical times, it is probable that the tsunami flooding areas produced by this types of events may reach residential, commercial and industrial areas of Quintero harbour within the next few decades, thus posing a potential risk to the local community and harbour activities in the area.

The evaluation of the flooded area is achieved with TUNAMI-N model, a numerical code developed by Dr. Nuobo Shuto in the Disaster Control Research Center, Tohoku University, Japan. The model is thoroughly described in the IOC's Time Project entitled *"Numerical Method of Tsunami Simulation with the Leap-Frog Scheme"* (IUGG/IOC, 1997). The input earthquakes are selected from a historical analysis of seismic events in the area bounded by 30°S to 37°S, along the Chile-Peru Trench. The 3RD March 1985 earthquake is used to calibrate the model whereas the 16TH August 1906 and 8TH July 1730 events are selected for the analysis.

The main objectives of this work are to:

- Design a tsunami flooding map for a range of possible scenarios based on historical near-field tsunami records and to define areas with different levels of tsunami risk.
- Produce velocity fields and wave height time series, giving a prediction of the wave arrival, evolution and maximum values within a 3 hours simulation.
- Establish a site-specific risk assessment for the coastal area, proposing public evacuation routes and safety areas for a potentially catastrophic tsunami in Quintero Bay.

Distant tsunamis, volcanic tsunamis and other type of uncommon tsunamis are not considered.

---

[2] *M_O is the Seismic Moment of the earthquake, defined by Talandier (1993; cited by SHOA, 1999) and reproduced in Section 2.4 of this report.*

1.3 QUINTERO BAY

Quintero Bay (Figure 1.1) was selected due to its high seismicity, the intense port activities of Puerto Ventanas and Terminales Químicos Oxiquim, and the growing development pressures in commercial and residential areas exhibited during the last decade. Quintero has a population of 16.119 inhabitants; it administratively belongs to V Región - Valparaíso and is located approximately 33 km North of Viña del Mar. Ventanas has 5029 inhabitants and is placed 8 km North of Quintero, belonging to the Puchuncaví Council (INE, 1992).

Valuable industrial facilities are located in relatively flat areas of Quintero bay (Figure 1.2), thus being affected by a high tsunami risk. The most important are: *Las Ventanas thermoelectric station*, which generates around 300.000 kW/hr (1996) satisfying the requirements of V Región and part of the metropolitan area of Santiago; *Las Ventanas Refinery*, with an annual capacity of 400.000 tonnes of 99.97% pure copper and *Oxiquim S.A.*, company which provide the Chilean and Latin American markets with chemical products and related services.

Climate is conditioned by the Humboldt Current, which regulates the sea surface temperature between 10°C and 18°C during the year. Daily and annual atmospheric temperature oscillations are moderate, with an annual average of approximately 14°C. Air temperatures fluctuate between 13°C to 20°C during summer and 9.5°C to 15°C in winter. The temperature gradient of 6° C/km is typical of the Chilean coast. The mean annual relative humidity is 82% and the precipitation is 462 mm, occurring between May and October. Atmospheric pressures range from 1025 mb in October to 1018 mb in May.

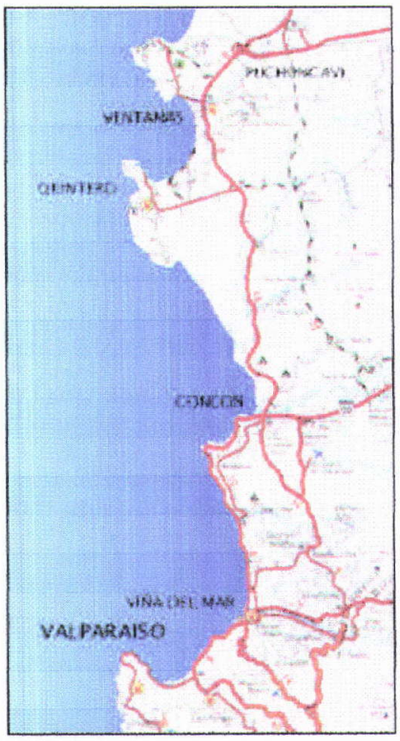


FIGURE 1.1.- CENTRAL CHILE COASTAL ZONE.
(Turistel, 1997).

The bay is oriented to the NW, being limited to the North by the rocky cliffs of Pta. Ventanilla and by Peninsula Los Molles to the S (Figure 1.3). The mouth of the bay has a length of approximately 4200 m, whereas the width of the bay is of about 2500 m. The ocean bottom presents an estimated bottom slope of m=0.03, with maximum depths of 70 m in the entrance of the bay. The city of Quintero is located in Peninsula Los Molles, a rocky formation of a maximum elevation of 85 m. Between Ventanas and downtown Quintero, the coast encompasses sandy beaches in Playa Herradura and Playa Loncura. Puerto Ventanas and the small town are located in a flat area defined by the basin of Estero Puchuncaví, on the NE limit of the bay.

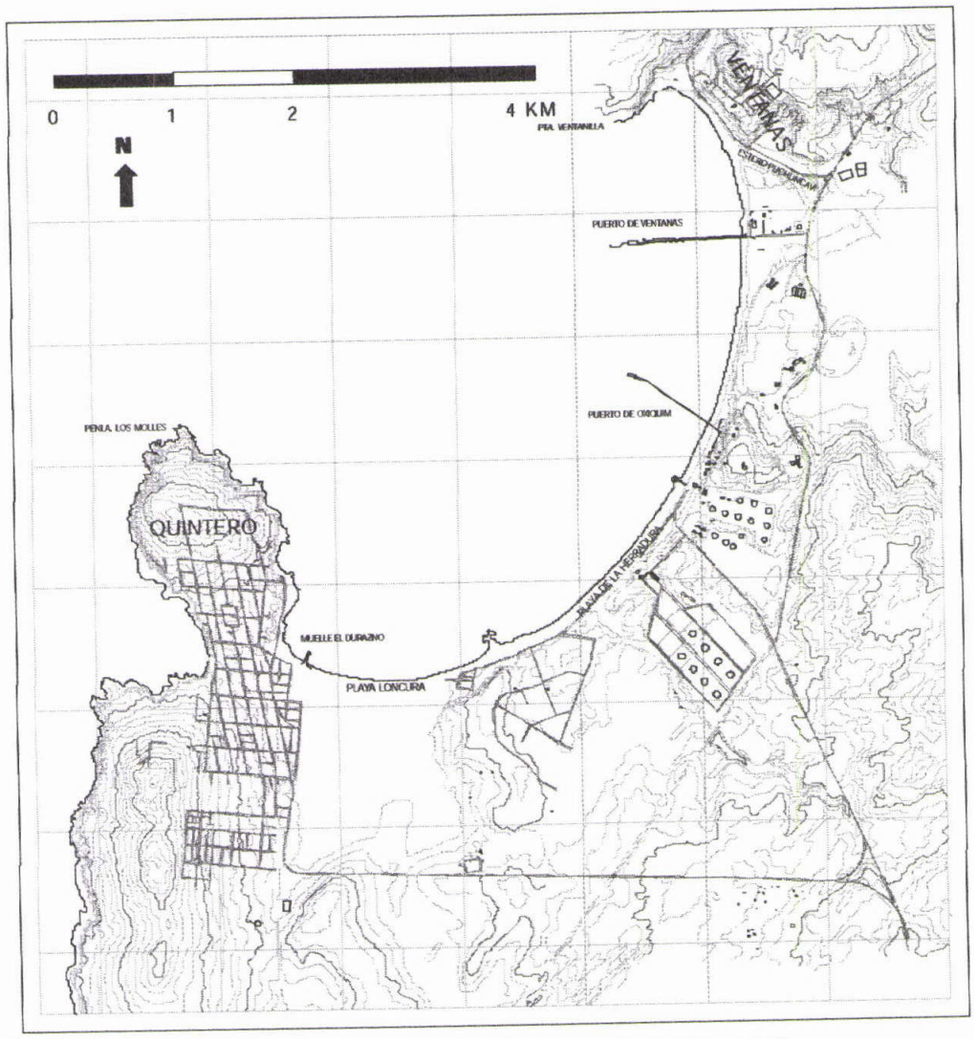


FIGURE 1.2.- QUINTERO BAY. (MINVU, 1996).



FIGURE 1.3.- AERIAL VIEW OF QUINTERO.

Tsunami history is not adequately recorded in Quintero. However, a chronological list of tsunamis that probably affected the bay can be extracted from those events recorded in Valparaíso (Table 1.1).

DATE	FAULT ZONE	RICHTER MAGNITUDE[3]	TSUNAMI MAGNITUDE[4]	TSUNAMI HEIGHT[5]
1562, Oct.28	Between 37° and 39°S		3	
1657, Mar.15	Between 36° and 39°S	$M_R = 8$	3	
1730, Jul.8	Between 31° and 34°S	$M_R = 8^3/_4$	4	
1822, Nov.19	Similar to 1906	$M_R = 8^1/_2$	2	4m
1835, Feb. 20	Concepción (off shore)	$M_R = 8 - 8^1/_4$	3	
1868, Aug.13	Southern Peru	$M_R = 8^1/_2$	4	
1877, May 9	20°15'S	$M_R = 8 - 8^1/_2$	4	
1906, Ago.16	33°S 72°O	$M_R = 8.6$	1	1m
1943, Apr.6	33°01'S 71°38'W	$M_R = 8.3$	1	0.91m
1971, Jul.8	32°5'S 71°2'W	$M_R =$		1.5m
1985, Mar.3	33.13°S 71.87°W	$M_R = 7.8$		1.15m

TABLE 1.1.- TSUNAMIS IN QUINTERO. Compiled from PILASI (1978) and MONGE (1996).

[3] *Richter Scale is analysed in Section 2.4.2*
[4] *Imamura's Tsunami Magnitude Scale is detailed in Section 2.4.9*
[5] *Values recorded in Valparaíso.*

1.4 LITERATURE REVIEW

1.4.1 HISTORICAL REMARKS

Tsunami research commenced in Japan as a consequence of the devastating effects of the phenomena in coastal areas. Although records concerning tsunamis can be found since the 17TH century, Hammack (1972) quotes that the scientific effort started in with the work of Takahasi (1942, 1945, 1947), Ichiye (1950) and Honda and Nakamura (1951), who contributed to the conception of a two dimensional linear theory to describe the waves resulting from bed deformations. Takahasi and Hatori (1962) first developed experiments on the mechanism of generation of tsunamis with a small-scale model using bed deformations for the simulation.

During the sixties, the significance of tsunamis interested an outstanding group of occidental scientists. Wilson and Torum (1968) combined computational facilities and theoretical principles to estimate the wave profile near the disturbance for the 1964 Alaskan earthquake. Gradually, numerical techniques, such as finite differences and boundary integral methods, were introduced for both near and far-field tsunamis (Hwang and Divoky, 1970; Hwang, Butlerand and Divoky, 1972; Houston and García, 1974).

The first field-applicable flooding predictions simulated the waves from their generation up to a 10 m depth boundary and used the computed wave height to estimate the inland flooding. These models solved relatively simple equations in different stages of the propagation and provided reasonable simulations of tsunamis for engineering purposes. Outcomes were nevertheless, inaccurate. During 1992-1995, post tsunami field surveys revealed that these models sometimes produced deviations of up to 1000% from field observations (Titov and Synolakis, 1996). With the availability of increasing computer power, scientists are nowadays able to model with improved accuracy and resolution tsunami generation, ocean propagation and coastal run-up of tsunamis with sophisticated numerical methods and acceptable accuracy.

Chile has been involved in tsunami research since 1964, when the National Tsunami Warning System begun its operations. In the academic field, Monge (1975) proposed a methodology for tsunami risk assessment, applied in Antofagasta, Quintero, Constitución, Bahía Laredo and Canutillar. Pilasi (1978) developed the first flooding risk assessment in Quintero harbour with a refraction diagram construction-orthogonal method. Since then, the advances in the subject have been significant. SHOA commenced the CITSU project ("Processing of Inundation Maps by Tsunamis for the Chilean Coast") in 1997 and has produced and published inundation maps for various Chilean harbours based on TUNAMI-N software and historical events (Table 1.2).

LOCATION	EARTHQUAKE	MAX. HEIGHT (m)	MAX. VELOCITY[6] (m/s)
Arica	1868	11.0	6.0
Arica	1877	12.0	7.0
Iquique	1868	7.0	7.0
Iquique	1877	18.5	7.0
Tocopilla	1877	9.0	7.0
Mejillones	1877	18.0	7.0
Antofagasta	1877	7.0	6.0
Antofagasta	1995	1.8	5.0
Caldera	1992	5.5	4.5
Valparaíso	1906	N.A.	N.A.
Valparaíso	1985	1.15	N.A.

TABLE 1.2.- TSUNAMI MODELS IN CHILEAN HARBOURS. SHOA (1997-2000).
N.A. : Not available information.

These maps show the flooded areas associated to one specific historical event and are not intended to provide a site-specific assessment of tsunami risk for each coastal community. The contribution of the present study is therefore to produce a tsunami flooding map considering a range of possible scenarios and advise upon mitigating measures for urban planning purposes.

[6] *According to the specialised bibliography, the term velocity will be used to characterise the magnitude (with no direction) of the currents generated by a tsunami.*

1.4.2 SEISMICITY IN THE CHILE-PERU TRENCH

The numerical simulation adopted in this project requires an extensive study of the seismological features of the area of interest, essentially because the selection of the characteristic set of modelling earthquakes will define the inundation areas and tsunami risk in the coastal zone of Quintero bay.

According to the Plate Tectonics Theory the Earth's crust (***Lithosphere***) consists of a system of viscous plates in continuous motion over a molten rock substrate (***Astenosphere***) as a consequence of the convection currents produced by temperature and pressure differentials in the upper layers of the Earth's mantle. The boundaries between plates, known as Benioff zones, show heterogeneous formations where a progressive accumulation of elastic stress shape up the seismic activity. The energy discharge may turn out in the form of low magnitude earthquakes, great events and/or non-seismic episodes, depending on the mechanism in which adjacent plates slide against each other and on the way in which accumulated potential energy built up over long periods of time is released.

In Chile, the Nazca Plate subducts the South American Plate at a relative motion of 10 cm/year (Figure 1.4).

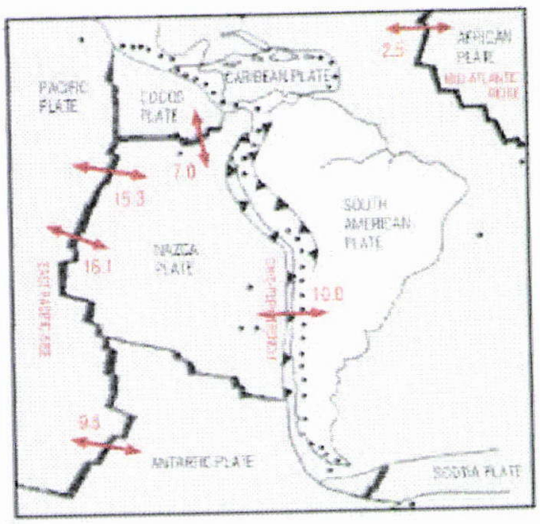


FIGURE 1.4.- TECTONIC PLATES IN SOUTH AMERICA. The total spreading data in cm/year is depicted in red. Active volcanoes are shown in black spots.

As a result of this progressive strain accumulation, great earthquakes of considerable extension have historically shocked the region. In recent geological ages, the subduction mechanism (Figure 1.5) has created the Andes Mountains and incidentally, the uplift of coastal areas by as much as a few meters as a result of seismic events.

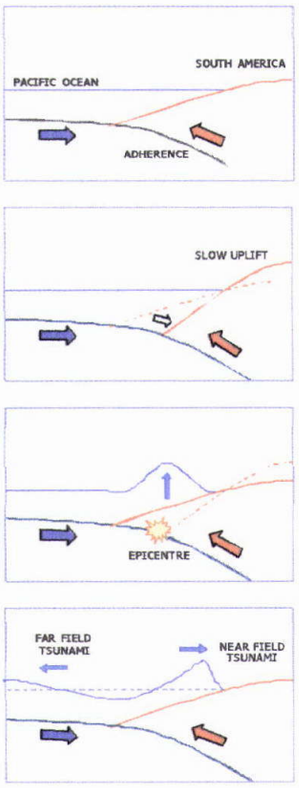


FIGURE 1.5.- SUBDUCTION IN THE CHILE-PERU TRENCH.

The need for a statistical approach to estimate the frequency of earthquakes in Central Chile has resulted in the application of the recurrence interval concept[7] and empirical relations obtained from near-field earthquake activity. For example, Kausel (1986) stated that the area limited by 33°S and 33.5°S has historically been affected to a 82±6 years recurrence interval of $M_R>7.8$ earthquakes, as obtained by considering the great-recorded events of 1575, 1647, 1730, 1822, 1906 and 1985. Alternatively, Pardo, Comte and Eisemberg (1989) proposed the following relation to evaluate occurrence probability for the area limited by 30.5°S-36.0°S to 71.0°W-73.0°W, as obtained from a data set of 578 events of $M_R>4$ in the area:

$$Log\,N = 4.756\ 0.828M$$

N: *Average occurrence of events with Richter's Magnitude $M_R>M$ in a year's period*
M: *Richter's Magnitude*

[7] *The recurrence interval is the estimated time between the occurrence of events of particular characteristics at a given site.*

The question to be answered is whether the type and frequency of tsunamis expected in Quintero bay could be estimated following the seismic history in the area. Adam and Furumoto (1970) recognised that the relation between earthquakes and tsunamis is not direct, and "*either very large tsunamis are generated or none at all*". Monge (1975) emphasised that tsunami amplitude is not necessarily proportional to the magnitude of the earthquake or, in other words, there is no reciprocity between both. Therefore, seismic records do not provide a reliable estimation of tsunami occurrence.

If tsunami records are taken into account, the problem deals with the reliability on the estimation of the occurrence probability of a phenomena that is not on the human time scale. It is not trustworthy to make statement about probabilities by extrapolating, even with sophisticated methods, sparse data. Extrapolation based on two or three points (which are not necessarily available in Quintero) is fraught with dangers.

From the engineering point of view however, the question of whether a tsunami of particular characteristics will affect a specific site during the design life of a structure still requires an answer and the disaster prediction must be anyway evaluated in important projects. The estimation of the expected damage, determined as the product of the economic losses times the occurrence probability of a particular event is not a rationale approach since slight differences in the estimation of the occurrence probability may result in dramatic variations of the expected damage. This approach, commonly used in well-documented phenomena, is not trustworthy for tsunamis.

The alternative approach is to use the best available technology to mitigate tsunami risk and to locate important facilities and infrastructure in high areas when possible. For example, a rule of thumb historically used in Chile is that the main building blocks of thermoelectric power stations have been placed in the range of 8 to 10 m above NRS to avoid tsunami impact (Vásquez, 2001).

Based on the above-mentioned facts, a purely probabilistic approach has been excluded from this investigation. Therefore, the methodology herein adopted is to analyse a range of possible scenarios based on the seismic characteristics of great earthquakes in Central Chile (i.e. the seismic moment of each event modelled) and to use them as the initial condition for tsunami numerical modelling, without assigning any occurrence probability to each event.

Great events occurred in Central Chile which are used in the preliminary analysis are generally described in Table 1.3.

DATE	RUPTURE LENGHT (km)	WIDTH (km)	MEAN DISLOCATION (m)	MAGNITUDE	SEISMIC MOMENT 10^{27} (dinas-cm)
1575	-	-	-	7 - 7.5	-
1647	365	-	-	8.5	-
1730	350 – 550	100 - 150	6 – 8	8.75	-
1822	200 – 330	100 – 150	3 – 6	8.5	-
1906	365 – 330	100 - 150	3 – 6	8.2 - 8.3	29 – 50
1985	170	100	1.23 – 1.60	7.8	10 - 11.5

TABLE 1.3.- GREAT EARTHQUAKES IN QUINTERO. Compiled from many authors. Further information of the 1730, 1906 and 1985 events may be found in Tables 3.3 and 3.4 (Chapter 3).

The selection of the modelling earthquakes (1730, 1906 and 1985) was based on the following arguments:

- The seismic information of the 1575 and 1647 events was insufficient and thus disregarded. The 1822 earthquake showed no tsunamigenic features and only general information concerning a possible tsunami is found in the bibliography.

- The 1730 earthquake produced the larger tsunami in the region during historical time. The main waves devastated a large part of El Almendral, in Valparaíso, and damaged other coastal communities in central Chile. Because of its considerable magnitude, it was used as an extreme case in the range of scenarios modelled.

- The characterisation of the 1730 rupture mechanism, thoroughly described in Section 3.4.3, was a demanding task during this research due to the scarcity and ambiguity of the historical information available. This effort was a contribution to the CITSU project, which historically used the 1985 and 1906 earthquake for the production of Inundation Maps in Central Chile.

- The 16TH August 1906 earthquake was already characterised (SHOA, 1999). As a consequence of the displacement the coast was uplifted about 0.5 m in Quintero; information, which was useful in the definition of the rupture, zone distribution (Tables 3.4 and 3.6).

- The 1985 earthquake was thoroughly characterised with the actual seismological network and therefore it was used for calibration purposes (SHOA, 1999). Calibration was achieved considering that the maximum uplift of the ocean crust was estimated in 0.5 m (Barrientos, 1987) and only tsunami amplitudes of 1.4 m were recorded in Valparaíso (SHOA, 2001).

A space time diagram of seismic history in Central Chile Coastal Zone is presented as follows:

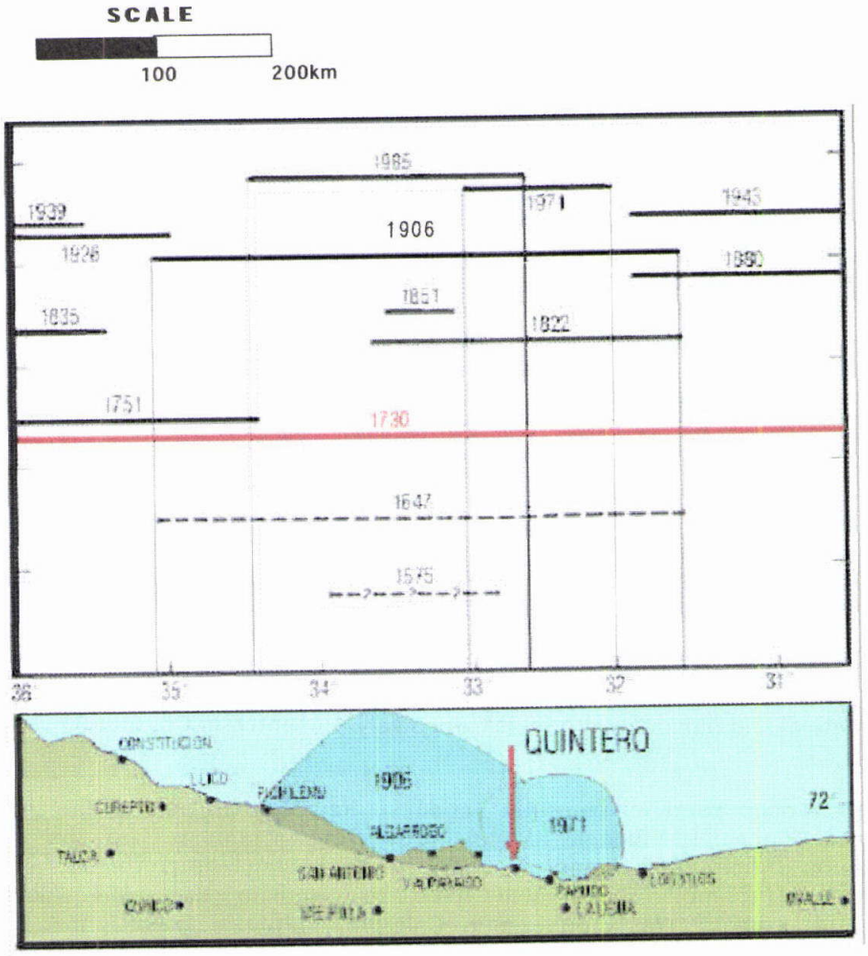


FIGURE 1.6.- SPACE-TIME DIAGRAM OF CENTRAL CHILE EARTHQUAKES. (Comte et al., 1986). Solid horizontal lines represent estimated rupture lengths.

1.4.3 TSUNAMI MODELS

An overall view of the numerical techniques and currently available models for tsunami generation, propagation and run-up is presented as follows. The numerical code used in this project, TUNAMI-N, is introduced in this section and thoroughly described in Section 3.

Generally speaking, **Finite Element Techniques** provide a suitable representation of solid mechanics and structural engineering, allowing a considerable freedom in modelling irregular geometries. For tsunami modelling, finite elements represent the domain of integration with different resolution according to the degree of accuracy required, thus allowing the representation of small-scale topographic features, which are difficult to represent with orthogonal grids. Unluckily, this technique is based in relatively complex algorithms resulting in longer computation times. The ADCIRC model, for example, has been extensively utilised by Myers, Baptista and Priest (1999), of the Oregon Graduate Institute, in the development of inundation maps in Oregon and Washington. **Finite Difference Techniques** provide a simple and efficient alternative in the discrete representation of continuum mediums, especially in fluid mechanics. Equations in tsunami models are relatively simple and algorithms efficient. However, they are implemented with orthogonal grids which require finer grids in the area of interest to obtain better precision in the results. The most popular models currently in use are the following:

TUNAMI-N

The TUNAMI-N code, developed in the Disaster Control Research Center of Tohoku University (Japan), simulates tsunami waves occurring over a model basin consisting of four nested grids, with coarse space increments in deep-ocean and finer ones in the shallow sea. The model uses an orthogonal staggered grid allowing a 3-Dimensional representation of the ocean bottom. The mathematical and numerical model is extensively presented in Chapter 3.

TUNAMI-N has been used in important Japanese harbours as part of the Japan Meteorological Agency's tsunami forecasting system. Examples are the 1983 Nihonkai-Chubu (Shuto, 1983) and the 1990 Mariana simulations (Imamura and Shuto, 1991). The model was also used to simulate the 1964 Alaskan earthquake in Kodiak, Washington and California (Preuss, 1988), the 1985 Mexican earthquake (Preuss, 1988) and various scenarios in Colombia (OSSO, 1999), Costa Rica, Perú (DHN, 1999) and Hawaii. It is currently being tested by Koshimura of JSPS/PMEL for Puget Sound, Washington. In Chile, SHOA has published a series of inundation maps for Chilean harbours based on the corresponding software (Table 1.2).

MOST (METHOD OF SPLITTING TSUNAMI)

The model is a suite of numerical simulation codes capable of simulating tsunami generation by a source near Alaska, its propagation across the Pacific Ocean and its subsequent run-up onto the Hawaiian shoreline. It was developed by in the Pacific Marine Environmental Laboratory, Seattle (USA) as part of the Early Detection and Forecast Tsunami (EDFT) project (Titov and Gonzalez, 1997). The model uses a finite difference method to divide its computational domain and uses different codes to simulate the generation by an earthquake, transoceanic propagation and coastal inundation.

The fault plane model utilises a formula for static sea-floor deformation to calculate the initial conditions required. The propagation includes the Earth's curvature, accounts for dispersive effects and permits the use of non-dispersive linear or non-linear equations. The dispersion scheme and the non-linear shallow water wave equations in spherical co-ordinates were proposed by Murty (1984; cited by Titov and Gonzalez, 1997):

$$h_t + \frac{(uh)_\lambda (vh\cos\phi)_\phi}{R\cos\phi} = 0$$

$$u_t + \frac{uu_\lambda}{R\cos\phi} + \frac{vu_\phi}{R} + \frac{gh_\lambda}{R\cos\phi} = \frac{gd_\lambda}{R\cos\phi} + fv$$

$$v_t + \frac{uv_\lambda}{R\cos\phi} + \frac{vv_\phi}{R} + \frac{gh_\phi}{R} = \frac{gd_\phi}{R} - fu$$

λ:	*Longitude*
ϕ:	*Latitude*
h:	*Amplitude*
d:	*Undisturbed water depth*
u, v:	*Depth averaged velocities in the longitude and latitude directions*
g:	*Gravity acceleration*
R:	*Earth's radius*
f:	*Coriolis parameters*

The equations are solved numerically using a splitting method described by Titov (1997). Unfortunately, the MOST domain for simulation is restricted to the North Pacific, from 15°N to 65°N and from 180°W to 120°W, with a global bathymetry data of 4 minutes does not considers Chilean coasts.

This capability is nowadays used to run multiple sensitivity studies based on the offshore wave dependence on distant earthquake magnitude and position, to evaluate site-specific inundation dependence on offshore wave characteristics and to produce inundation charts in California and Hawaii.

MIKE 21

The Danish Hydraulic Institute has developed the numerical model MIKE 21 NHD (Nested HydroDynamic Module) for applications on estuaries, coastal waters and seas, which was later adapted for tsunami simulation (DHI, 2000). It includes a graphical package for visual data checking, graphs and animations of figures and a variety of facilities.

MIKE 21 NHD uses a finite difference model in a user-defined number of dynamically nested grids (*dynamically* means that there is feedback from the fine resolution grid to the enclosing coarser grid during the calculations). The model can work with up to nine bathymetries of different resolution, allowing more than one grid at each level of equal spatial resolution. This is a great advantage compared with TUNAMI-N model since it eventually allows a simultaneous simulation of relatively close harbours. Besides, the digitation can be done on a digitising tablet compatible with the model and using the Bathymetry Editor

The model solves unsteady two-dimensional flow in a vertically homogeneous fluid layer on a 3-Dimensional bathymetry.

$$\frac{\partial \eta}{\partial t}+\frac{\partial M}{\partial x}+\frac{\partial N}{\partial y}=0$$

$$\frac{\partial M}{\partial t}+\frac{\partial}{\partial x}\left(\frac{M^2}{D}\right)+\frac{\partial}{\partial y}\left(\frac{M\,N}{D}\right)+g\,D\frac{\partial \eta}{\partial x}+\frac{g}{D^2}\frac{M\sqrt{M^2+N^2}}{C^2}-fVV_x-\frac{D}{\rho w}\frac{\partial p_a}{\partial x}-\Omega N-E\left(\frac{\partial^2 M}{\partial x^2}+\frac{\partial^2 N}{\partial y^2}\right)=Sx$$

$$\frac{\partial N}{\partial t}+\frac{\partial}{\partial x}\left(\frac{M\,N}{D}\right)+\frac{\partial}{\partial y}\left(\frac{N^2}{D}\right)+g\,D\frac{\partial \eta}{\partial y}+\frac{g}{D^2}\frac{N\sqrt{M^2+N^2}}{C^2}-fVV_y-\frac{D}{\rho w}\frac{\partial p_a}{\partial y}-\Omega M-E\left(\frac{\partial^2 M}{\partial x^2}+\frac{\partial^2 N}{\partial y^2}\right)=Sy$$

x, y, t:	*Horizontal co-ordinates and time*
M, N:	*Discharge fluxes in x and y axes*
Sx, Sy:	*Source magnitude and components*
η:	*Vertical displacement, referenced to the still water level*
C:	*Chezy resistance number*
g:	*Gravity acceleration*
D:	*Total depth*
f:	*Wind friction factor*
V, Vx:	*Wind velocity and components*
p_a:	*Barometric pressure*
ρw:	*Density of water*
Ω:	*Coriolis coefficient*
E:	*Eddy viscosity coefficient*

The *conservation of momentum* incorporates turbulence effects, subgrid scale fluctuations and effective shear stresses due to vertical integration of the Saint Venant equations in a velocity based formulation.

MIKE 21 allows the incorporation of wind friction factors, wave radiation stresses and two ways of describing the bed resistance, either as a Chezy or Manning number, on each grid point separately. The boundary condition inputs may be specified as **a)** *water levels and direction of the flow* or **b)** *total flow and direction* on each point of the boundary, **c)** sinusoidal variations (specially for tidal models) or **d)** *user defined* boundary conditions. Moving boundaries, an essential feature in tsunami modelling, can also be included to simulate the possibility of tsunami flooding and drying of areas.

MIKE 21 can work with Courant numbers up to about 5 without presenting stability problems (Section 3.5). A soft start (warming) is achieved by introducing the hydrodynamic forcing parameters in a gentle way (linear variation), thus avoiding numerical shock at the beginning of the simulation. From the engineering viewpoint, it may include the effect on bridge piers, rivers or outlets from power stations on the hydrodynamic calculation by using a subgrid scaling technique.

CHAPTER 2
TSUNAMI HYDRODYNAMICS

This chapter introduces the reader to the complex phenomena of tsunamis by presenting the general features associated to tsunami wave generation (Section 2.1), propagation in open ocean (Section 2.2) and coastal amplification and run-up (Section 2.3). Tsunami parameters are also introduced (Section 2.4).

2.1 TSUNAMI WAVE GENERATION

2.1.1 SOURCE MECHANISMS

Sea states present a spectrum of surface oscillations caused by a variety of geophysical mechanisms, mentioned as follows:

- **SUBMARINE EARTHQUAKES**

Tectonic dislocations along subduction areas produce vertical variations (uplift or depression) of the Earth's crust and infringe potential energy into the overlying water mass, radiated away from the source region in the form of long period waves. Tsunamigenic earthquakes are characterised by shallow focus[1] (<60km) generated on dip-slip faults and are mainly activated by the vertical component of the crust dislocation.

The generation is a complex phenomenon that depends upon the earthquake's magnitude, distribution and orientation of the rupture zone; rupture dimensions, epicentre location and vertical displacement. The rupture zone is characterised by an approximately parabolic area with the major axis running parallel to the fault line. The velocity of the dislocation in which energy is transferred to ocean water is important in the generation and waveform of the tsunami.

In terms of the energy relation between earthquakes and tsunamis, only about 0.5% to 10% of the seismic energy is converted into tsunami energy. Van Dorn (1968) estimated that only 0.65% of the seismic energy is transmitted to the overlying mass of water, whereas Iida (1970) gave a significantly higher estimation of 10%.

---

[1] *The focus corresponds to the estimated point where the earthquake is initiated. For the purposes of this investigation, earthquakes will be characterised by the entire rupture zone, defined by a series of parameters as shown in Table 3.2 (Section 3.4.3).*

- **VOLCANIC ACTIVITY**

Volcanic tsunamis are characterised by a small origin, with divergent waves that rapidly decrease in height due to the spreading of energy. A clear example is the August 1883 eruption of the island of Krakatoa, in the Sunda Strait, Indonesia. The explosion destroyed approximately 8 km^3 of the island and caused large shoreline subsidence. Tsunami waves were up to 30 m, destroyed 295 villages and killed about 36.000 people on the coasts of Java and Sumatra (Murty, 1977).

- **SUBMARINE AVALANCHES AND LANDSLIDES**

Submarines avalanches are often a consequence of earthquakes but can be activated by other mechanisms as well. Waves spread from the point source, with considerable heights near the origin and decay gradually as they advance in the open ocean. A dramatic example of water waves generated by rock falls is found in the 9TH July 1958 Alaskan Tsunami, where waves reached an estimated maximum surge elevation of about 518 m in Lituya Bay and 61 m waves seaward in the bay (Murty, 1977).

- **NUCLEAR EXPLOSIONS**

Nuclear explosions represent an impulsive-generating mechanism from a point source. It has been observed that the wave height is dependent on the depth of the explosion and is inversely proportional to the distance from the origin. Van Dorn (1961) studied tsunami propagation caused by underground nuclear explosions at Eniwetok Atoll, Wake Island, and measured the decay with distance. He observed that the linear wave theory was adequate for the description of the phenomenon in open ocean.

- **OTHER SOURCES**

Tsunamis can be produced by the resonance of trench water, generated when the dominant frequency of seismic waves coincides with the natural frequency of a particular trench. Long-period surface earthquake waves (so called Rayleigh waves) have a vertical component responsible for the transmission earthquake energy to the overlying water mass.

Atmospheric tsunamis are tsunami-like waves generated by a rapidly moving atmospheric pressure front over a shallow sea at about the same speed as the waves, allowing them to couple.

2.1.2 OTHER TYPE OF SURFACE WAVES

A number of mechanisms for tsunami wave generation were briefly analysed in the previous section. It should be stated however, that sea states present a complex arrangement of a variety of other types of surface waves. Among them, wind-generated waves, storm surge, tides, hurricanes and other cyclonic meteorological events should be considered when evaluating the possible consequences of tsunami attack. Many authors have studied other types of waves (Ippen, 1966; Sorensen, 1978; *Shore Protection Manual*, 1984, among others) so for the sake of brevity, their study is excluded from this research.

A summary of different type of waves and cause-mechanisms are depicted in Figure 2.1.

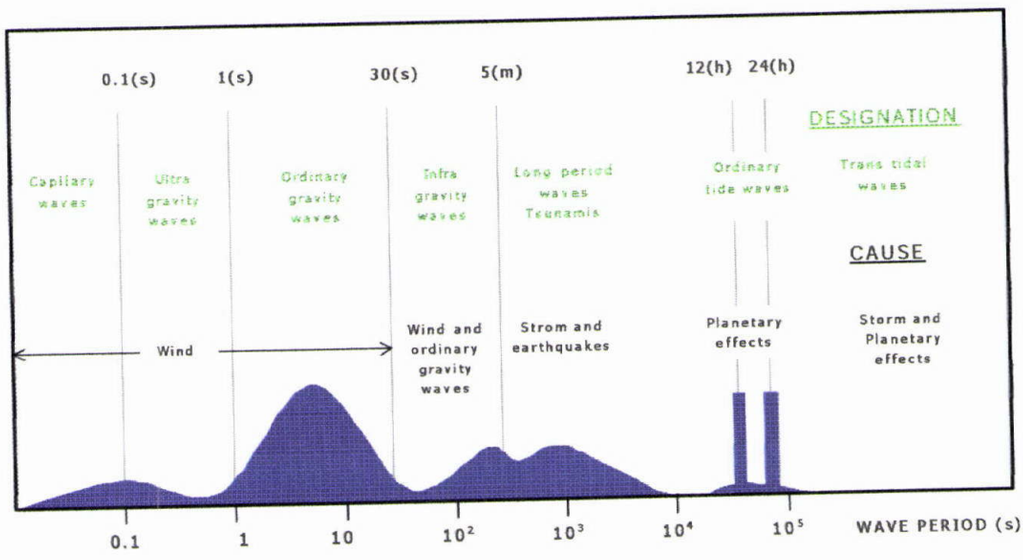


FIGURE 2.1.- ENERGY DENSITY SPECTRUM OF SURFACE WAVES. (Munk; cited by Murty, 1977)

2.2 PROPAGATION IN OPEN OCEAN

2.2.1 GENERAL REMARKS

To determine tsunami wave elevations and current speeds in Quintero bay, it is necessary to propagate tsunamis across the ocean by means of the numerical code herein used. The initial mound of water generated by the earthquake in the Chile-Peru Trench will evolve into a wave train as approaching the bay and will be modified by refraction, diffraction, scattering, energy losses and reflection caused by offshore and coastal features, resulting in variations of the celerity of the wave group, wave height and approaching direction.

Tsunamis generally present a wide spectrum of periods in the immediate rupture zone and, as the wave front propagates, short periods tend to attenuate, prevailing longer ones (*non-linear wave to wave transfer*; Sorensen, 1978). The propagation impulse is generally stronger in one direction because of orientation of the rupture zone, mechanism which results in waves travelling from the source in all directions, with the main energy propagation generally being orthogonal to the direction of the main axis of the fracture zone.

Wavefronts propagate in deep oceans with 30 to 60 cm in height and neither can be felt aboard ships nor can be easily detected from air. Wavelength may be as long as 650 km, with a period ranging from 5 min to 2 h as they travel across the ocean. Far-field tsunamis can take up to 22 h to arrive at coastal areas within the Pacific Basin, depending on the distance to the source, whereas near-field tsunamis can take few minutes to reach the coast.

The celerity of the wave group (C_g) represents the rate at which wave energy is propagated. The equation for the wave group provided by the small amplitude wave theory (Airy, 1845) is the following.

$$C_g = nC \qquad C^2 = \frac{gL}{2\pi}\tanh\left(\frac{2\pi h}{L}\right)$$

C_g: *celerity of the wave group*
C: *phase celerity*
n: *ratio of wave group to phase celerity* [2]
g: *acceleration of gravity*
L: *wave length*
h: *depth*

[2] *The term n ranges from 0.5 in deep water (h/L > 1/2) to 1 in shallow water (h/L < 1/25). This means that n*

It is observed that in deep and transitional waters (i.e. $1/25 < h/L$), the celerity of the wave group is generally lower to the phase celerity of individual waves within the group. *"An observer that follows a group of waves at group celerity will see waves that originate at the rear of the group move forward through the group travelling at the phase celerity and disappear at the front of the wave group"* (Shore Protection Manual, 1984). This is a typical behaviour occurring in the propagation of wind-generated waves, where slightly longer waves travel faster than smaller ones. Tsunamis however, do not show this behaviour since celerity is determined by the relation:

$$C_g = (gh)^{1/2}$$

The celerity is dependent only on the depth and is not conditioned by the wavelength (or period). As a consequence, group and phase velocities are equal and each component of the wave front travels at the same speed, showing no dispersion effects.

2.2.2 ENERGY LOSSES AND SPREADING

Tsunami energy is dissipated by friction forces on the sea bottom, internal shear stresses (viscosity and turbulence), interaction with the air above and other secondary effects. The wave bottom boundary layer is often the dominant dissipative mechanism of energy loss during propagation. According to Tsuruta (cited by Godoy, 1975), the head loss caused by bottom friction presents an inverse proportionality to ocean depth.

$$\Delta H \propto \frac{1}{d^{2/3}}$$

Based on this finding, energy dissipation is expected to be important in shallow waters but minor in the deep ocean, fact that could explain the ability of tsunamis generated in the Chile-Peru Trench to reach the Japanese coast with significant heights and destructive potential. The present research explicitly considers bottom friction only in the vicinity of Quintero bay and neglects dissipation in the offshore computation[3].

The lateral spreading of energy is another important effect in the propagation of far-field tsunamis, extended over a wide geographical area due to the sphericity of the earth. This effect however, is negligible in near-field tsunamis as the propagation area is generally small (lateral spreading is not included in TUNAMI-N code).

---

[3] *The bottom friction term is included as a non-linear term in the equations of momentum for Grid D and is neglected in Grids A, B and C. For detailed information see Section 3.3.*

2.2.3 REFRACTION

Tsunami waves undergo changes due to refraction during propagation as though they were shallow water waves[4]. According to conventional theories, wave celerity is proportional to the ocean depth; hence the front moves faster in deep waters and changes its direction gradually as it approaches the coast. *"If the waves are long crested and are moving obliquely towards a shoreline, those portions of the wave front which gradually feel bottom first are retarded first, so that the wave becomes subject to a progressive curving of refraction which, in its overall effect, tends to align the wave front to the depth contours"* (Bretschneider cited by Ippen, 1966). As the ocean waves enter shallow waters, the different frequencies are sorted, and the resulting spectrum undergoes a transformation.

In general terms, bays produce a divergence in the wave rays, resulting in a reduction of the energy density and wave height. In peninsulas, the increasing of distance between orthogonals in the direction of wave travel denotes an area affected by a concentration of energy and a considerable amplification (Figure 2.2). Therefore, refraction has relevant influence in wave height, direction and energy distribution along the coast.

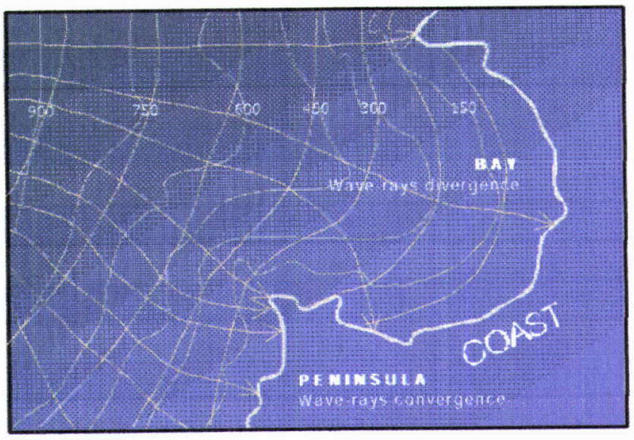


FIGURE 2.2.- REFRACTION ON IRREGULAR COASTS.

---

[4] *Tsunamis are unique in that the waveform extends through the entire water column from sea surface to the ocean bottom. Their small relative depth (ocean depth/wavelength) is responsible for refraction in the open ocean. Ordinary wind waves, in contrast, are not affected by refraction in deep waters.*

2.3 COAST AMPLIFICATION AND RUN-UP

2.3.1 GENERAL REMARKS

When tsunami waves propagate into coastal areas they interact with the coastal topographic features in a variety of ways, including reflection, shoaling and refraction, and under certain conditions may locally be reflected, trapped, or focused. Tsunamis entering bay could be subjected to resonant conditions and wave energy may become trapped, resulting in a substantial increase of wave heights at particular coastal points.

With regards to the time history, the arrival of a tsunami is sometimes preceded by short-period, low-amplitude oscillations, known as forerunners. These may be sometimes followed by an initial withdrawal caused by the trough preceding the first wave crest, or an elevation resembling a strong surge, which increases the sea level. Takahashi (1961) stated that the rupture zone may present a simultaneous uplift and downfall of the ocean floor in opposite limits of the fault, thus producing an initial elevation along the coast adjacent to the uplifted zone and a depression in the zone located near the downfall of the ocean floor.

2.3.2 SHOALING EFFECT

When a tsunami reaches the coastline, decreases in celerity and wavelength and increases in height as a consequence of the effect of the ocean bottom. This effect, known as shoaling is explained in the following terms: the energy of a wave system is the sum of its kinetic and potential energy, defined as:

$$E = \rho g H^2 L / 8$$

E: *Total energy of a wave per unit of width*
ρ: *Density*
L: *Wavelength*
g: *Acceleration of gravity*
H: *Wave height*

According to the small amplitude wave theory, in shallow waters (i.e. tsunamis) the wavelength is:

$$L = T C = T (gh)^{1/2}$$

C: *Phase celerity*
T: *Wave period*
h: *Depth*

The above equation shows that as the wave advances towards shallow waters, it decreases its wavelength, with a constant period. Then, if energy reflection, generation and dissipation are considered negligible along a short path, the total energy per unit crest *(E)* is approximately constant and consequently wave height *(H)* increases on approaching the coast. This is known as shoaling.

With supplementary algebraic work it can be shown that the final wave height *(H)* will depend on the wave height offshore (Ho), the shoaling effect $(\sqrt[4]{d_o/d})$ and refraction (b_o/b) and may be computed by the following equation (Shore Protection Manual,1984):

$$\frac{H}{H_o} = \sqrt{\frac{b_o}{b}} \quad \sqrt[4]{\frac{d_o}{d}}$$

H: *Wave height (H_o means offshore wave height)*
b: *Distance between two wave rays.*
d: *Depth*

It follows that, as the wave approaches shallow waters (i.e. decreasing h/Lo), wavelength and celerity gradually decrease, wave height increases as a result of shoaling and wave steepness (H/L) increases considerably. Ippen (1966) plotted these results in a log-log paper, as shown in Figure 2.3.

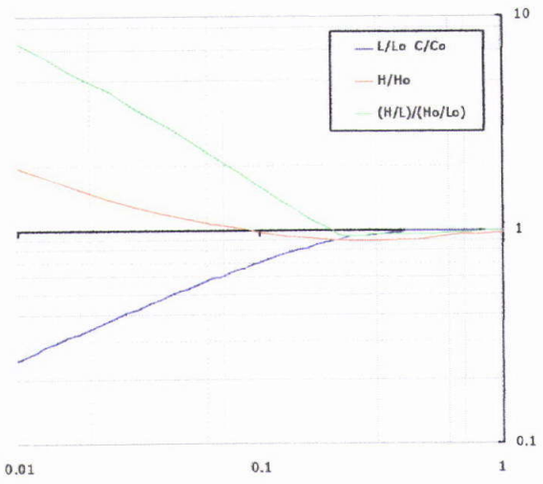


FIGURE 2.3.- THEORETICAL WAVE TRANSFORMATION. (Ippen, 1966). Derived in channels of regular section based on the Small Amplitude Wave Theory, assuming no generation, dissipation and reflection of energy, and referred to offshore conditions (Lo, Co, Ho and Ho/Lo).

2.3.3 THE EFFECT OF BATHYMETRY

Bathymetry is significant in controlling diffraction, refraction, resonance, reflection and interference, effects that determine the final height and celerity of the incident wave. With regards to the effects of the ocean bottom configuration, it is accepted that in large shallow bays, the energy may become trapped and, as the wave increases in height, it can break before reaching the coast.

In steep coastal slopes, the flooding advances as non-breaking waves without exceeding a few metres. Wave energy may be reflected offshore in the coast and on man-made structures (breakwaters and coastal installations) but may also come up as a huge mass of water when reaching the coastline. The presence of coral reef, energy dissipating breakwaters and other obstacles reduce the effect of the wave reaching the coast.

In some cases, relatively protected bays are subjected to severe tsunami effects because of the constricted morphology of the coastline. The presence of islands in the mouth of a bay does not necessarily mean that the tsunami effect will be minor in the coast. In fact, flow could eventually be conducted through narrow inlets that tend to increase the wave celerity and the hydrodynamic energy may become trapped in the bay due to reflection effects.

2.3.4 RESONANCE

The main tsunami waves are followed by secondary undulations that can be a consequence of resonance in partially closed bays. It is recognised that when an external force acts over a confined body of water, it oscillates according to its natural period. If the tsunami period is close to the natural period of the bay, it is expected that as the second tsunami wavefront reaches the bay, the reflected leading wave will be summed with the latter, producing a superposition with significant amplitudes. Consequently, when the natural period of the bay coincides with the main period of the tsunami wave spectrum, resonance may result in a considerable higher run-up than expected.

This may result in an increase of energy in harbours and in bays where dissipation is insignificant and may often be as important as refraction and diffraction. This effect may become significant in Quintero because of the semi-confined characteristic of the bay.

2.3.5 DIFFRACTION

Diffraction is the effect by which the energy is transmitted along the wave front. It is noticeable where regular waves are interrupted by natural obstacles (peninsulas, islands, submarine mountains, etc.) or man-made structures (breakwaters, ports, etc.) and occurs simultaneously with refraction. For a complex wave spectrum, each component is diffracted according to its wavelength in a continuous process.

2.3.6 BREAKING MECHANISM

The level of damage caused by a tsunami varies notably with the wave breaking mechanism. Breaking limits the height of surface waves, dissipates surface wave energy, transfers momentum flux from waves to currents, and makes energy available for mixing the water column. In shallow waters, where tsunami heights are similar in magnitude to the still water depth, the peak of the wave will propagated inward faster than the trough because of the greater depth at high water. Then, breaking may eventually occur if the peak overtakes the trough, with the high-water crest finally falling forward as the tsunami continues to advance.

From many authors, the following classification of tsunami waveforms approaching the coast is proposed:

- **BREAKING WAVES,** which collapse violently near the shoreline with uneven height. Damage is enormous, basically because of the high flow velocities involved. Major structures are destroyed and rolled over and the vegetation is damaged. Inland flat areas are largely flooded.

- **NON-BREAKING WAVES,** which behave as rapidly rising tides. The effect inland is similar to a flooding; the vegetation cover is not disturbed by the flow but may have a secondary impact due to the high salinity of the intrusion. Light structures may be flooded and damaged.

- **BORE-TYPE GENERATED WAVES** in estuaries, rivers and coastal lagoons that show a very rapid rise in which the advancing water presents an abrupt front of considerable height. They show an intermediate damage compared to the above-mentioned mechanisms.

2.3.7 RUN-UP VELOCITY

During tsunami run-up, the kinetic energy is transformed either to potential energy or reduced by dissipation, having great erosion ability due to the flow velocity. Several authors have estimated maximum velocities due to great tsunamis. According to Goody and Monte (1975), the inland flow may reach up to 10 m/s. Titov and Synolakis (1996) and Tsutsumi et al. (2000) estimated a velocity of up to 18 m/s at Okushiri, Japan, for the July 12TH 1993 Southwest Hokkaido earthquake tsunami. Table 1.2 shows a summary of heights and maximum velocities of numerical simulations in Chile.

Overland flow is usually considered as supercritical with bore-like dynamics and capable of removing sand beaches and coastal vegetation that may have taken years to grow. In relatively flat areas, the flooding may largely extend inland, covering extensions of land with water and debris.

The development of tsunami waves inland and its impact in coastal structures is difficult to simulate due complexity of the overland flow. Some authors suggest that the flooding is more correlated with velocities rather than wave heights, but the majority observe that damage is a combination of flow velocity, the advancing direction and the height of the incoming tsunami. As Shimamoto et al. stated (1995; cited by Tsutsumi et al., 2000) if these variables were predicted quantitatively beforehand, this analysis would be a powerful tool for the future assessment of tsunami disasters in other areas.

2.4 TSUNAMI AND RELATED PARAMETERS

2.4.1 GENERAL REMARKS

The definition of wave parameters is presented as follows. Some empirical formulas have been included in the section to give an order of magnitude of each variable. However, it must be emphasised that these formulas are restricted to the set of hypothesis, physical constrains and geographical location considered in their derivation.

2.4.2 WAVE HEIGHT

Wave height (H) is the vertical difference between two consecutive peaks and troughs, corrected for the change of tide of both measurements (Figure 2.4).

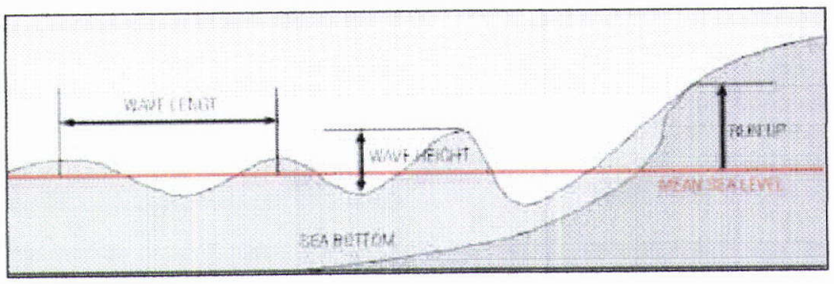


FIGURE 2.4.- TSUNAMI PARAMETERS

Empirical formulas correlating wave height with seismic and tsunami parameters have been, for example, derived by Imamura and Wilson (cited by Pilasi, 1978).

$\log_{10} H = 0.375m$ (Imamura) $\log_{10} H = 0.75M - 5.07$ (Wilson)

H: *Wave height, in metres*
m: *Imamura's tsunami magnitude (Table 2.1)*
M: *Richter's Magnitude*

These relations are obsolete because Richter's Magnitude underestimates the tsunamigenic potential of large earthquakes and Imamura's magnitude does not considers the local variability of maximum heights (Farreras, 1995).

2.4.3 RUN-UP

Run-up *(R)* is the vertical level difference between the maximum tsunami penetration, or flooding line, reached by seawater at the time of the tsunami attack and a reference datum, ideally measured at a point that is a local maximum of the horizontal flooding. (the *mean sea level*[5] is here adopted as the reference datum). In practical terms, run-up is only measured where there is a clear evidence of the flooding limit on the shore and its definition requires a rigorous protocol extensively explained in IOC (1998).

The following empirical relations were obtained from the references. Unluckily, only basic facts on the limitations and methodologies by which they were obtained is cited, so their application does not provide a reliable estimation of run-up on a particular site. Wilson and Torum (1968) proposed an equation based on the Richter's magnitude, obtained from field measurements of the 1964 Alaskan Earthquake, which seems to be conservative for Chilean tsunamis:

$$\log_{10} R = 0.75M - 4.82$$

R: *Run-up, in metres*
M: *Richter's Magnitude*

According to Godoy and Monge (1975), run-up may be estimated based on the wave height and wavelength of the tsunami:

$R = 0.206\, H^{0.685} L^{0.315}$ (slope of 1:60) $\qquad R = 0.381\, H^{0.684} L^{0.316}$ (slope of 1:30)

R: *Run up, in metres*
H: *Wave height, in metres*
L: *Wavelength, in metres*

This relation gives no detail of where the height and wavelength should be considered. Alternatively, Wiegel (cited by Godoy, 1975) proposed an equation based on the bottom slope and wave height:

$$R = 0.5\, Ho\sqrt{2\pi/\alpha}$$

R: *Run up, in metres*
Ho: *Wave height, in metres*
α: *Slope angle*

---

[5] *The mean sea level is defined as the average height of the sea surface, based upon observation of tide height on the open coast or in adjacent waters which have free access to the sea, over a nineteen-year period.*

As stated above, these equations are not considered as a good estimate for tsunami flooding prediction in Quintero bay because of the scarcity and ambiguity of their empirical methods.

When empirical formulas are not appropriate, it is possible to obtain important data from historical records. Maximum run-ups versus distance to the epicentre for major Chilean tsunamis are shown in Figure 2.5. With particular exceptions, run-up attenuation with the distance to the epicentre can be observed.

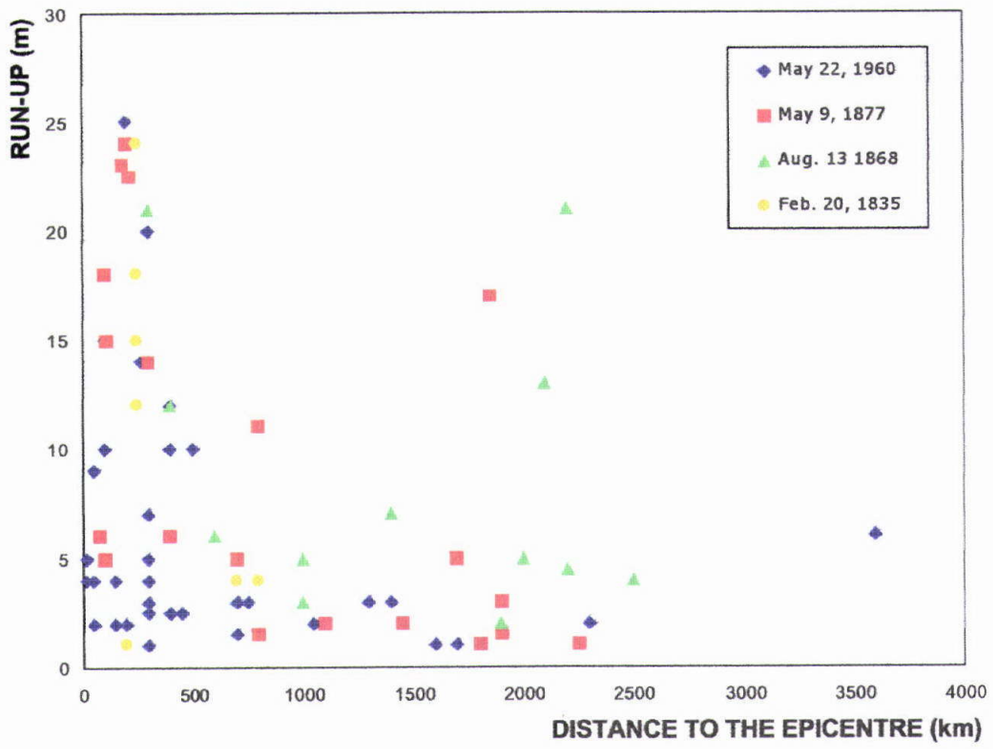


FIGURE 2.5.- RUN-UP V/S EPICENTRAL DISTANCE FOR GREAT CHILEAN AND PERUVIAN TSUNAMIS. (Lizana, 2000)

2.4.4 CELERITY

Tsunami celerity *(C)* is the rate of propagation of a surface wave, which, according to the small amplitude wave theory, is dependent only on the water depth and independent on the wavelength and period (Table 2.1). It is determined by the relation:

$$C = \sqrt{gh}$$

g: *Acceleration of gravity*
h: *Depth*

It should be noted that celerity demotes the rate of propagation of a surface wave and does not represent the orbital velocity of each individual particle of fluid. However, in deep waters the crest particle velocity is proportional to the wave height for a given wave period, being typically much lower than the wave celerity. As approaching the coast, wave heights increase and orbital velocity of particles will eventually equal the wave celerity (Sorensen, 1978).

Based on this, it should be noted that velocity fields obtained with TUNAMI-N code within Quintero bay represent individual particle velocities, as referred in Section 2.3.7.

2.4.5 WAVE LENGTH

The wavelength *(L)* is the horizontal distance between any two corresponding positions on successive waves. According to the small amplitude wave theory, wavelength is defined by the relation:

$$L = T\sqrt{\frac{gL}{2\pi}\tanh\left(\frac{2\pi h}{L}\right)}$$

g: *acceleration of gravity*
L: *slope angle*
h: *depth*

For shallow water waves (i.e. tsunamis) the above equation is simplified to $L=T(gh)^{1/2}$ and the wavelength is dependent on the depth and period (Table 2.1).

2.4.6 PERIOD

The period is the amount of time that a tsunami wave takes to complete a cycle. The period remains constant and independent of depth for oscillatory waves (Shore Protection Manual, 1984).

Celerity and wavelength as a function of the depth and period are computed with the above equations are shown in Table 2.1.

DEPTH (m)	WAVE PERIOD (min)	CELERITY (km/h)	WAVELENGTH (km)
4000	5	713	59
2000	5	504	42
500	5	252	21
100	5	113	9
4000	30	713	356
2000	30	504	252
500	30	252	126
100	30	113	56
4000	60	713	713
2000	60	504	504
500	60	252	252
100	60	113	113
4000	120	713	1426
2000	120	504	1008
500	120	252	504
100	120	113	225

TABLE 2.1.- TSUNAMI CELERITY, WAVELENGTH AND PERIOD.

2.4.7 ESTIMATED ARRIVAL TIME

The estimated arrival time is the time the first tsunami waves reach a fixed location, as estimated from modelling propagation and run-up. Monge (1975) and Pilasi (1978) predicted that near-field tsunami would take about 14 to 20 min to reach Quintero, depending on the location of the source mechanism.

2.4.8 TSUNAMI MAGNITUDE

Despite their many limitations, magnitude scales are essential in areas were no mareographs have been installed and they afford the only means for interpreting historical data. Many authors have proposed tsunami magnitude scales (Iida and Imamura, 1956; Iida, 1970; Abe, 1981) which have become obsolete with the development of numerical models and sophisticated methods. Iida and Imamura, for example (extracted from Lizana, 2000) proposed the following magnitude scale:

GRADE SCALE	RUN-UP (m)	ENERGY (erg x 10^{23})	DESCRIPTION
-1	-	0.003	Minor tsunami.
0	1 – 1.5	0.025	No damage.
1	2 – 3	0.1	House damage along coast; ships washed ashore.
2	4 – 6	0.4	Some destruction of houses; considerable loss of life.
3	8 – 12	1.6	Damaged area along coast about 400km.
4	16 – 24	6.4	Damaged area along coast about 500km.

TABLE 2.2.- TSUNAMI GRADE SCALE OF IIDA AND IMAMURA. Depending on the requirement, this scale has been extended occasionally from -3 to 5 (Lizana, 2000).

2.4.9 SEISMIC MOMENT

Since Richter's Magnitude tends to underestimate the source dimensions and the uplift of earthquakes above M_R=7.5 in the scale (Lorca, 2001), it is not a very reliable parameter to characterise the tsunamigenic potential of earthquakes. The approach herein adopted is to characterise earthquakes by their Seismic Moment (M_O), defined in MKS metric system, as:

$$M_o = \mu L W \overline{\Delta D}$$

L: *Length of the rupture zone*
W: *Width of the rupture zone*
μ *Stiffness of the crustal strata*
$\overline{\Delta D}$: *Mean dislocation*

This parameter better defines the amount of energy released and the potential for tsunami generation of earthquakes above M_R=7.5 (M_O>10^{22} Nm), for the reason that the volume of seawater in motion is directly proportional to the fault dislocation and rupture area, therefore is proportional to the Seismic Moment. Its determination is done through the analysis of long period seismic waves; fact that implies that high frequencies that do not have influence on tsunami wave generation are removed and only the macroseismic features of the rupture mechanism are considered.

Many authors have suggested that the Seismic Moment is the best parameter to characterise the tsunamigenic potential of earthquakes (Abe, 1973; Abe,1975; Okal, 1988; Talandier y Okal, 1989; Reymond, Hyvernaud y Talandier, 1993; cited by SHOA, 1999). According to Talandier (1993; cited by SHOA, 1999) the relation between the Seismic Moment and the tsunamigenic potential is given in Table 2.3:

SEISMIC MOMENT (Nm)	DESCRIPTION
$Mo < 10^{21}$	No tsunami generated
$10^{21} \leq Mo < 5x10^{21}$	Minor tsunami
$5x10^{21} \leq Mo < 2x10^{22}$	Potentially destructive tsunami
$Mo \geq 2x10^{22}$	Great and destructive tsunami

TABLE 2.3.- TSUNAMI POTENTIAL AS A FUNCTION OF THE SEISMIC MOMENT

On the succeeding analysis, tsunami risk assessment in Quintero bay will be based on the above-mentioned classification.

CHAPTER 3
METHODOLOGY

This chapter presents the mathematical and numerical principles of TUNAMI-N code, providing some comments of the limitations, extent and possibilities of its application for tsunami risk assessment in Quintero bay. A summary of the bathymetric and topographic information used on the grids generation process and the seismologic data for the seismic events used in the numerical simulation is also presented.

3.1 GENERAL REMARKS

In recent years, a significant effort has been done to quantitatively evaluate tsunami risk in coastal areas. This is generally achieved through inter-disciplinary studies in seismology, geology and oceanography, as well as including the revision of the historical sources. Tsunami modelling is then used to discriminate among the different possible scenarios (i.e. source locations and rupture mechanisms) that can affect a particular site. Above all, numerical simulation has become the best available technique for risk assessment in areas where historical records are insufficient. The model herein applied, TUNAMI-N, is based on the IOC's Time Project entitled *"Numerical Method of Tsunami Simulation with the Leap-Frog Scheme"*, developed by Dr. Nuobo Shuto in the Disaster Control Research Center, Tohoku University, Japan (IUGG/IOC, 1997).

TUNAMI-N simulates the generation, propagation and run-up of tsunami waves occurring over a model basin consisting of four nested spatial grids, with coarse space increments in deep-ocean and finer ones in the shallow sea. The model uses a set of discrete points arranged in an orthogonal staggered grid representing a 3D image of the ocean bottom where wave mechanics equations are solved. The following assumptions are implicit in the model:

- The vertical displacement of the sea bottom is calculated with the Mansinha and Smylie method (1971).
- Tsunami propagation is modelled with the Goto y Ogawa (1982) method, consisting of the numerical integration of the shallow water wave equations by means of a leap frog finite difference scheme with upwind convection terms.
- Coastal flooding is determined using the moving boundary condition proposed by Iwasaki and Mano (1979).

The model was developed in Fortran and compiled with the *Microsoft Developer Studio. Fortran Power Station 4.0 (Copyright© 1994-95)*. Graphical outputs and some algorithms used in the digitisation of the bathymetry were implemented with *Matlab 5.3 (Copyright©1984-99)*.

The numerical code is based upon the shallow water wave theory, obtained by vertically integrating the equations of continuity and conservation of momentum along the water column in an orthogonal co-ordinate system.
Some comments concerning the equations of conservation of momentum are reviewed in this section to show the advantages and limitations of TUNAMI-N code (wave mechanics equations will be then deduced in Section 3.2). The equation of conservation of momentum, integrated along the water column is (DHI, 2000):

$$\frac{\partial M}{\partial t}+\frac{\partial}{\partial x}\left(\frac{M^2}{D}\right)+\frac{\partial}{\partial y}\left(\frac{M\,N}{D}\right)+g\,D\frac{\partial \eta}{\partial x}+\frac{g\,n^2}{D^{7/3}}M\sqrt{M^2+N^2}-fVV_x-\frac{D}{\rho w}\frac{\partial p_a}{\partial x}-\Omega N-E\left(\frac{\partial^2 M}{\partial x^2}+\frac{\partial^2 M}{\partial x^2}\right)=0$$

$$\frac{\partial N}{\partial t}+\frac{\partial}{\partial x}\left(\frac{M\,N}{D}\right)+\frac{\partial}{\partial y}\left(\frac{N^2}{D}\right)+g\,D\frac{\partial \eta}{\partial y}+\frac{g\,n^2}{D^{7/3}}N\sqrt{M^2+N^2}-fVV_y-\frac{D}{\rho w}\frac{\partial p_a}{\partial y}-\Omega M-E\left(\frac{\partial^2 M}{\partial x^2}+\frac{\partial^2 N}{\partial y^2}\right)=S$$

x, y, t:	*Horizontal co-ordinates and time*
M, N:	*Discharge fluxes in x and y axis respectively*
η:	*Vertical displacement, referenced to the still water level*
n:	*Manning's factor*
g:	*Acceleration of gravity*
D:	*Total depth. ($D=h+\eta$, where h is the still water depth)*
f:	*Wind friction factor*
V, Vx:	*Wind velocity and components*
p_a:	*Barometric pressure*
ρw:	*Density of water*
Ω:	*Coriolis coefficient*
E:	*Eddy viscosity coefficient*

TUNAMI-N code considers the following simplification:

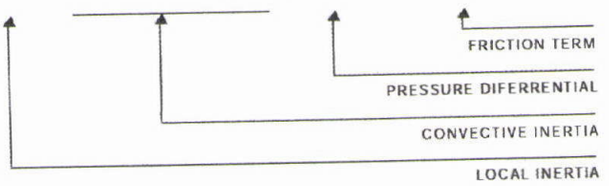
- The effective shear stress due to viscosity and turbulence is considered as a sub-grid scale effect in the model and is therefore neglected $(E \to 0)$. The contribution to the shear force, caused by the temporal variation of flow velocities in the direction of the flow Streeter (1962), is also disregarded. The wind force is considered irrelevant also $(f \to 0)$.

- The Coriolis force $(\Omega \to 0)$, barometric differentials $(\partial p_a/\partial x \to 0 \text{ and } \partial p_a/\partial y \to 0)$ and wave dispersion are considered large-scale phenomena and therefore are excluded from the simulation.

Based on the above mentioned simplifications, the conservation of momentum for a two-dimensional dominion considering inertial forces, pressure, gravitational and bottom friction forces is the following:

$$\frac{\partial M}{\partial t}+\frac{\partial}{\partial x}\left(\frac{M^2}{D}\right)+\frac{\partial}{\partial y}\left(\frac{M\,N}{D}\right)+g\,D\frac{\partial \eta}{\partial x}+\frac{g\,n^2}{D^{7/3}}M\sqrt{M^2+N^2}=0$$

$$\frac{\partial N}{\partial t}+\frac{\partial}{\partial x}\left(\frac{M\,N}{D}\right)+\frac{\partial}{\partial y}\left(\frac{N^2}{D}\right)+g\,D\frac{\partial \eta}{\partial y}+\frac{g\,n^2}{D^{7/3}}N\sqrt{M^2+N^2}=0$$



x, y, t:	*Horizontal co-ordinates and time*
M, N:	*Discharge fluxes in x and y axis respectively*
η:	*Vertical displacement, referenced to the still water level*
n:	*Manning's factor*
g:	*Acceleration of gravity*
D:	*Total depth ($D=h+\eta$, where h is the still water depth)*

These equations provide a simplification of the wave mechanics, based on the fact that disregarded terms are negligible in the near-field tsunami phenomena.

Other comments concerning the limitations of the programme are:

- Bed resistance is modelled through the Manning's coefficient defined, for the purposes of the present research, constant in time and space in Grid D (Section 3.5). Sensitivity analyses were carried out to estimate the variability of computed heights under a range of possible conditions (n=0.02-0.03; Lorca 2001) showing minor differences of ±1.5% in the final wave run-ups. Therefore, areas with different land use, soil structure and vegetation, or those where small-scale topographic features or coastal structures are found were represented with a single value of n=0.025.

- Surface tension, evaporation and other surface effects are neglected.

- No alterations to the seabed are caused by sediment transport (erosion or siltation) and the ocean bottom is considered impermeable during the simulation.

- The astronomical tide does not vary with respect to time during the simulation and is set equal to the *mean sea level*[1] (MSL); selected as the reference level for the evaluation of the flooding line in the model. According to SHOA (2001), the maximum high tide recorded in Quintero is 1.66 m above the *lowest astronomical tide*[2] (LAT), and the difference between MSL and LAT is of 0.90 m (Figure 3.1).

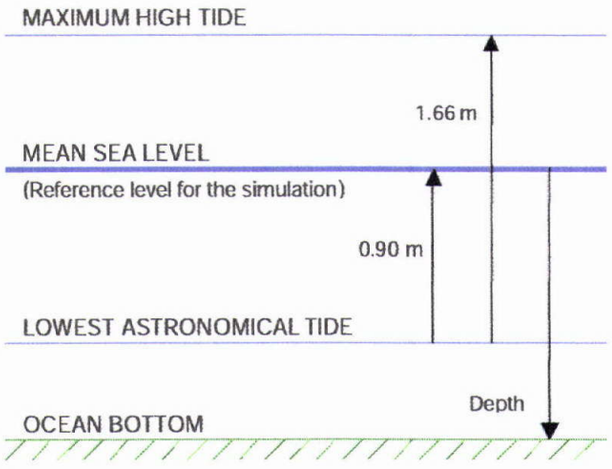


FIGURE 3.1.- ALTIMETRIC REFERENCE LEVEL

Since the depth on the hydrographic charts (Table 3.1) is given relative to the LAT and were digitised relative to this datum, 0.90 m were added to the bathymetry data to have the same reference datum than the topographic information (Appendix 4).

Since probable maximum tsunami flooding is a result of a combination of hydrometeorological and geophysical factors considered reasonably possible for the area, tidal effect could be roughly accounted as the difference between the existing water level at the time of tsunami attack, which, in the worst case is of 0.76 m (i.e. the difference between the maximum high tide and the mean sea level, as shown in Figure 3.1). This is however, a gross estimation since tide interacts non-linearly with the tsunami, thus making a simple superposition of waves invalid.

---

[1] *The mean sea level (MSL) is defined as the average height of the sea surface, based upon observation of tide height on the open coast over a nineteen-year period.*

[2] *The lowest astronomical level (LAT) corresponds to the datum plane (or chart datum) above which tidal levels are given in Chilean tide tables and below which ocean depths are referred.*

- The model does not include the loss of energy and momentum by breaking in the coast. Breaking conditions and bore-type tsunami development are neglected and only non-breaking waves are modelled.

- An orthogonal co-ordinate system is suitable to solve the proposed equations because of the local scale of the simulation. In far-field tsunamis, the polar co-ordinate system is used since the transoceanic effects are important.

At this point it must be said that at the actual state of the art, no model can explicitly include all the physical processes governing tsunamis. The above restrictions provide a simple model keeping precision in an acceptable level. Accordingly with previous simulations, the model is not accurate enough so as to simulate the wave profile but produces satisfactory results for the maximum run-up heights and inundated areas. The final error in the run-up, as estimated from calibration processes in Japan is usually within 15% (Aida and Hatori, 1984; Hasegawa, 1986; Shuto et al., 1987; cited by Shuto, 1991).

3.2 MATHEMATICAL MODEL

The numerical simulation is comprised by a mathematical model and the corresponding numerical model (Section 3.3) to give a sufficiently accurate solution to tsunami generation, propagation and run-up. It should be noted that the numerical simulation is, at best, as good as the mathematical model adopted. For near-field tsunamis, TUNAMI-N uses the linear shallow water wave theory in deep-ocean and incorporates non-linear terms (bottom friction and convection) in coastal areas, according to the relative importance of these effects in the phenomena. The basic assumptions that support this theory are:

- Horizontal velocity of particles is uniform along the water column.
- Vertical acceleration is negligible compared to gravitational acceleration.
- Curvature of the trajectories of water particles is sufficiently small.
- Physical properties (density, temperature, salinity, etc.) are constant along the depth.

Based upon these approximations, it is assumed that the vertical motion of water particles has no effect on pressure distribution, considered as hydrostatic. Set (3.1) represents the governing equations in the shallow water wave theory.

$$(3.1a) \quad \frac{\partial u}{\partial x}+\frac{\partial v}{\partial y}+\frac{\partial w}{\partial z}=0$$

$$(3.1b) \quad \frac{\partial u}{\partial t}+u\frac{\partial u}{\partial x}+v\frac{\partial u}{\partial y}+g\frac{\partial \eta}{\partial x}+\frac{\tau_x}{\rho}=0$$

$$(3.1c) \quad \frac{\partial v}{\partial t}+u\frac{\partial v}{\partial x}+v\frac{\partial v}{\partial y}+g\frac{\partial \eta}{\partial y}+\frac{\tau_y}{\rho}=0$$

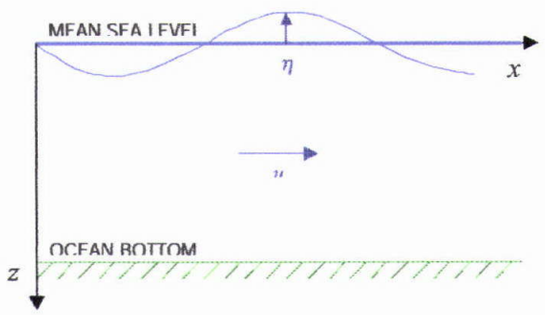


FIGURE 3.2.- CO-ORDINATE LEVEL

x, y, t:	*Horizontal co-ordinates and time*
u, v:	*Water particle velocities in x and y axis*
η:	*Vertical displacement, referenced to the still water level*
h:	*Water depth, referenced to the still water level*
g:	*Acceleration of gravity*
ρ:	*Density*
τ_x, τ_y:	*Bottom frictions in x and y axis.*

Equation (3.1.*a*) represents the vertically integrated version of the principle of conservation *of mass*.

Equations (3.1.*b*) and (3.1.*c*) result from the formal statement of the principle of conservation of momentum in the x and y directions respectively, considering bottom friction, hydrostatic pressure profiles and convection terms.

The unknown quantities are the vertical displacement of the water surface (η) and the water particle velocities (u and v). The water depth is obtained for each grid point from hydrographic charts and is thus considered constant in the calculation. Bottom friction terms (τ_x, τ_y) are explicitly defined in terms of (η, u and v), in analogy to the uniform flow, as follows:

$$(3.2.a) \quad \frac{\tau_x}{\rho} = \frac{1}{2g}\frac{f}{D}u\sqrt{u^2+v^2}$$

$$(3.2.b) \quad \frac{\tau_y}{\rho} = \frac{1}{2g}\frac{f}{D}v\sqrt{u^2+v^2}$$

f:	*Friction coefficient*
u, v:	*Water particle velocities in x and y axis*
g:	*Acceleration of gravity*
D:	*Total depth ($D=h+\eta$, where h is the still water depth)*

Equations (3.2.*a*) and (3.2.*b*) can be defined in terms of the Manning's roughness coefficient:

$$(3.3) \quad n = \sqrt{\frac{f\,D^{1/3}}{2g}}$$

Combining (3.2) and (3.3), the bottom friction terms are expressed by the formulas:

$$(3.4.a) \quad \frac{\tau_x}{\rho} = \frac{g\,n^2}{D^{4/3}}u\sqrt{u^2+v^2}$$

$$(3.4.b) \quad \frac{\tau_y}{\rho} = \frac{g\,n^2}{D^{4/3}}v\sqrt{u^2+v^2}$$

It should be noted that because of their relative depth (η/h), tsunamis present a channel-type flow in which Manning's coefficient becomes a suitable parameter to represent the interaction of the water flow and the ocean surface.

The assumptions that the horizontal velocity of particles is uniform along the depth and that the vertical acceleration is negligible allow the vertical integration of set (3.1) to obtain a 2D model. The domain of computation $D(x,y,z,t)$ is therefore reduced to an integral version $D(x,y,t)$, thus reducing the computation time and simplifying the equations to simple terms without incorporating a significant error in the results.

The integration is not trivial and is therefore explained in Appendix 3. The integral version accepts the introduction of new target variables, the average discharge fluxes along the depth (*M*) and (*N*) which together with the vertical displacement of the water surface (η) define the problem with sufficient precision.

$$(3.5.a) \quad M = u(h+\eta) = u\,D$$

$$(3.5.b) \quad N = v(h+\eta) = v\,D$$

The shallow water wave theory with quadratic friction and convection of momentum is composed by the equation of continuity (3.6.*a*) and the equations of motion (3.6.*b*) and (3.6.*c*). This set is used in the near-shore computation of tsunami propagation and run-up (Grid D, Section 3.4).

$$(3.6.a) \quad \frac{\partial \eta}{\partial t} + \frac{\partial M}{\partial x} + \frac{\partial N}{\partial y} = 0$$

$$(3.6.b) \quad \frac{\partial M}{\partial t} + \frac{\partial}{\partial x}\left(\frac{M^2}{D}\right) + \frac{\partial}{\partial y}\left(\frac{M\,N}{D}\right) + g\,D\frac{\partial \eta}{\partial x} + \frac{g\,n^2}{D^{7/3}} M\sqrt{M^2+N^2} = 0$$

$$(3.6.c) \quad \frac{\partial N}{\partial t} + \frac{\partial}{\partial x}\left(\frac{M\,N}{D}\right) + \frac{\partial}{\partial y}\left(\frac{N^2}{D}\right) + g\,D\frac{\partial \eta}{\partial y} + \frac{g\,n^2}{D^{7/3}} N\sqrt{M^2+N^2} = 0$$

In Grids A, B and C (Section 3.4), the relatively smooth bathymetry and the absence of important topographic formations in deep oceans produce minor effects. Therefore, convection and bottom friction terms are neglected and set equations (3.6) become the linear long wave theory.

$$(3.7.a) \quad \frac{\partial \eta}{\partial t} + \frac{\partial M}{\partial x} + \frac{\partial N}{\partial y} = 0$$

$$(3.7.b) \quad \frac{\partial M}{\partial t} + g\,D\frac{\partial \eta}{\partial x} = 0$$

$$(3.7.c) \quad \frac{\partial N}{\partial t} + g\,D\frac{\partial \eta}{\partial y} = 0$$

Linearity allows the reduction of the computational time. Historical records show that the depth-to-length ratio is on the order of 10^{-2} and the wave steepness is of order 10^{-4} for a tsunami wave, values that suggest that the linear long wave theory gives satisfactory results in seas deeper than 50 m (Shuto, 1991).

3.3 NUMERICAL MODEL

The leap-frog scheme with a truncation error of second order in a staggered grid is presented in the following section. To obtain the discrete wave mechanic equations, the classical numerical theory proposed by Taylor (1715) is used.

A function $F(x)$ can be represented by a power series in an open interval containing $(x=c)$ as follows:

$$(3.8)\quad F(x)=F(c)+\frac{\partial F(c)}{\partial x}(x-c)+\frac{\partial^2 F(c)}{\partial x^2}\frac{(x-c)^2}{2!}+\ldots+\frac{\partial^n F(c)}{\partial x^n}\frac{(x-c)^n}{n!}+\ldots$$

Considering consecutive values in the x-axis, with a spatial interval (Δx), the values of $F(x)$ are:

$$(3.9a)\quad F_{(i-1)}=F_{(i)}-\frac{\partial F_{(i)}}{\partial x}\Delta x+\frac{\partial^2 F_{(i)}}{\partial x^2}\frac{\Delta x^2}{2!}+O(\Delta x^3)$$

$$(3.9b)\quad F_{(i+1)}=F_{(i)}+\frac{\partial F_{(i)}}{\partial x}\Delta x+\frac{\partial^2 F_{(i)}}{\partial x^2}\frac{\Delta x^2}{2!}+O(\Delta x^3)$$

The difference between these series not considering higher order terms yields the central difference expression (3.10). It is evident that a set of equations of higher-order would provide better results, especially if used with fine spatial grids, but this provides a sufficiently precise approximation to this phenomenon.

$$(3.10)\quad \frac{\partial F_{(i)}}{\partial x}=\frac{1}{2\Delta x}\left(F_{(i+1)}-F_{(i-1)}\right)+O(\Delta x^2)$$

3.3.1 LINEAR LONG WAVE THEORY

From expression (3.10) it is possible to establish a finite difference algorithm to solve the linear long wave equations (3.7) with a step-by-step methodology. Each term in equation (3.7.*a*) is represented as[3]:

$$(3.11.a)\quad \frac{\partial \eta}{\partial t} = \frac{1}{\Delta t}\left(\eta_{(i,j)}^{k+1} - \eta_{(i,j)}^{k}\right)$$

$$(3.11.b)\quad \frac{\partial M}{\partial x} = \frac{1}{\Delta x}\left(M_{\left(i+\frac{1}{2},j\right)}^{k+\frac{1}{2}} - M_{\left(i-\frac{1}{2},j\right)}^{k+\frac{1}{2}}\right)$$

$$(3.11.c)\quad \frac{\partial N}{\partial y} = \frac{1}{\Delta y}\left(N_{\left(i,j+\frac{1}{2}\right)}^{k+\frac{1}{2}} - N_{\left(i,j-\frac{1}{2}\right)}^{k+\frac{1}{2}}\right)$$

It is convenient to define the unknown variables (M), (N) and (η) in separate grids. Substituting (3.11) in (3.7.*a*) yields a discrete version for the conservation of mass.

$$(3.12)\quad \eta_{(i,j)}^{k+1} = \eta_{(i,j)}^{k} - \frac{\Delta t}{\Delta x}\left(M_{\left(i+\frac{1}{2},j\right)}^{k+\frac{1}{2}} - M_{\left(i-\frac{1}{2},j\right)}^{k+\frac{1}{2}}\right) - \frac{\Delta t}{\Delta y}\left(N_{\left(i,j+\frac{1}{2}\right)}^{k+\frac{1}{2}} - N_{\left(i,j-\frac{1}{2}\right)}^{k+\frac{1}{2}}\right)$$

Discharge fluxes are computed according to equations (3.13) and (3.14):

$$(3.13)\quad M_{\left(i+\frac{1}{2},j\right)}^{k+\frac{1}{2}} = M_{\left(i+\frac{1}{2},j\right)}^{k-\frac{1}{2}} - g\, D_{\left(i+\frac{1}{2},j\right)}^{k} \frac{\Delta t}{\Delta x}\left(\eta_{(i+1,j)}^{k} - \eta_{(i,j)}^{k}\right)$$

$$D_{\left(i+\frac{1}{2},j\right)}^{k} = h_{\left(i+\frac{1}{2},j\right)} + \eta_{\left(i+\frac{1}{2},j\right)}^{k} = h_{\left(i+\frac{1}{2},j\right)} + \frac{1}{2}\left(\eta_{(i+1,j)}^{k} + \eta_{(i,j)}^{k}\right)$$

$$(3.14)\quad N_{\left(i,j+\frac{1}{2}\right)}^{k+\frac{1}{2}} = N_{\left(i,j+\frac{1}{2}\right)}^{k-\frac{1}{2}} - g\, D_{\left(i,j+\frac{1}{2}\right)}^{k} \frac{\Delta t}{\Delta y}\left(\eta_{(i,j+1)}^{k} - \eta_{(i,j)}^{k}\right)$$

$$D_{\left(i,j+\frac{1}{2}\right)}^{k} = h_{\left(i,j+\frac{1}{2}\right)} + \eta_{\left(i,j+\frac{1}{2}\right)}^{k} = h_{\left(i,j+\frac{1}{2}\right)} + \frac{1}{2}\left(\eta_{(i,j+1)}^{k} + \eta_{(i,j)}^{k}\right)$$

---

[3] *Equation (3.10) has been modified to allow an improved calculation with a temporal interval ($\Delta t/2$) and spatial intervals ($\Delta x/2$) and ($\Delta y/2$) respectively. Indices (i), (j) and (k) represent the steps of computation in the x-axis, y-axis and time.*

The arrangement of grid points on the staggered grid used in the leap frog scheme is presented in Figure 3.3. The sequence of computation for the linear long wave theory is presented in Figure 3.4.

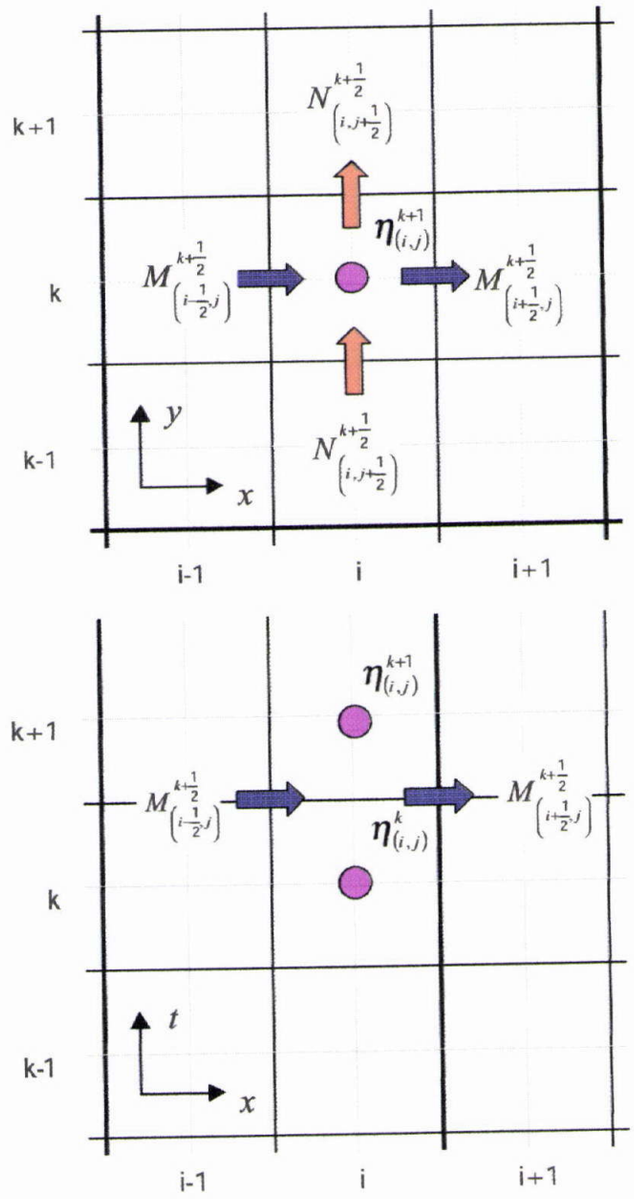
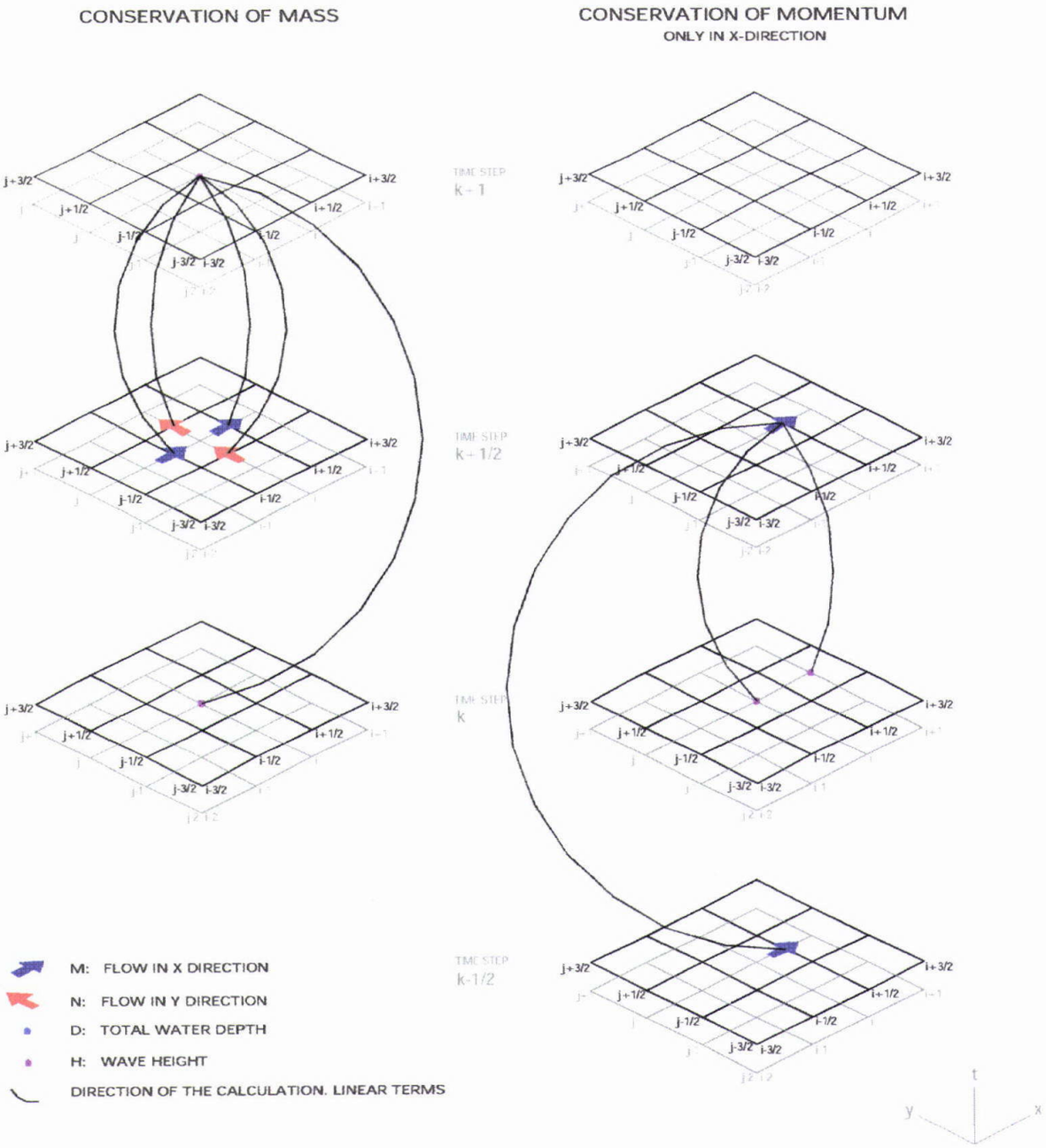


FIGURE 3.3.- GRID POINTS ARRANGEMENT IN THE LEAP FROG-SCHEME

FIGURE 3.4.- THE LEAP-FROG SCHEME: LINEAR LONG WAVE THEORY



3.3.2 NON LINEAR SHALLOW WATER THEORY

The model requires the discretization of convection and friction terms in equations (3.6.*b*) and (3.6.*c*). The conservation of mass remains as equation (3.12).

3.3.2.1 APPROXIMATION OF CONVECTION TERMS.

The approximation of convection terms in equation (3.6.*b*) and (3.6.*c*) is presented in (3.15) to (3.18).

$$(3.15)\quad \frac{\partial}{\partial x}\left(\frac{M^2}{D}\right)=\frac{1}{\Delta x}\left[\lambda_{11}\frac{\left(M^{k-\frac{1}{2}}_{\left(i+\frac{3}{2},j\right)}\right)^2}{D^{k-\frac{1}{2}}_{\left(i+\frac{3}{2},j\right)}}+\lambda_{21}\frac{\left(M^{k-\frac{1}{2}}_{\left(i+\frac{1}{2},j\right)}\right)^2}{D^{k-\frac{1}{2}}_{\left(i+\frac{1}{2},j\right)}}+\lambda_{31}\frac{\left(M^{k-\frac{1}{2}}_{\left(i-\frac{1}{2},j\right)}\right)^2}{D^{k-\frac{1}{2}}_{\left(i-\frac{1}{2},j\right)}}\right]$$

$$(3.16)\quad \frac{\partial}{\partial x}\left(\frac{MN}{D}\right)=\frac{1}{\Delta x}\left[\lambda_{12}\frac{M^{k-\frac{1}{2}}_{\left(i+1,j+\frac{1}{2}\right)}N^{k-\frac{1}{2}}_{\left(i+1,j+\frac{1}{2}\right)}}{D^{k-\frac{1}{2}}_{\left(i+1,j+\frac{1}{2}\right)}}+\lambda_{22}\frac{M^{k-\frac{1}{2}}_{\left(i,j+\frac{1}{2}\right)}N^{k-\frac{1}{2}}_{\left(i,j+\frac{1}{2}\right)}}{D^{k-\frac{1}{2}}_{\left(i,j+\frac{1}{2}\right)}}+\lambda_{32}\frac{M^{k-\frac{1}{2}}_{\left(i-1,j+\frac{1}{2}\right)}N^{k-\frac{1}{2}}_{\left(i-1,j+\frac{1}{2}\right)}}{D^{k-\frac{1}{2}}_{\left(i-1,j+\frac{1}{2}\right)}}\right]$$

$$(3.17)\quad \frac{\partial}{\partial y}\left(\frac{MN}{D}\right)=\frac{1}{\Delta y}\left[\upsilon_{11}\frac{M^{k-\frac{1}{2}}_{\left(i+\frac{1}{2},j+1\right)}N^{k-\frac{1}{2}}_{\left(i+\frac{1}{2},j+1\right)}}{D^{k-\frac{1}{2}}_{\left(i+\frac{1}{2},j+1\right)}}+\upsilon_{21}\frac{M^{k-\frac{1}{2}}_{\left(i+\frac{1}{2},j\right)}N^{k-\frac{1}{2}}_{\left(i+\frac{1}{2},j\right)}}{D^{k-\frac{1}{2}}_{\left(i+\frac{1}{2},j\right)}}+\upsilon_{31}\frac{M^{k-\frac{1}{2}}_{\left(i+\frac{1}{2},j-1\right)}N^{k-\frac{1}{2}}_{\left(i+\frac{1}{2},j-1\right)}}{D^{k-\frac{1}{2}}_{\left(i+\frac{1}{2},j-1\right)}}\right]$$

$$(3.18)\quad \frac{\partial}{\partial y}\left(\frac{N^2}{D}\right)=\frac{1}{\Delta y}\left[\upsilon_{12}\frac{\left(N^{k-\frac{1}{2}}_{\left(i,j+\frac{3}{2}\right)}\right)^2}{D^{k-\frac{1}{2}}_{\left(i,j+\frac{3}{2}\right)}}+\upsilon_{22}\frac{\left(N^{k-\frac{1}{2}}_{\left(i,j+\frac{1}{2}\right)}\right)^2}{D^{k-\frac{1}{2}}_{\left(i,j+\frac{1}{2}\right)}}+\upsilon_{32}\frac{\left(N^{k-\frac{1}{2}}_{\left(i,j-\frac{1}{2}\right)}\right)^2}{D^{k-\frac{1}{2}}_{\left(i,j-\frac{1}{2}\right)}}\right]$$

The values for λ_{ij} and ν_{ij} are selected to give better accuracy to the calculation according to the direction of the flow at a particular time:

$$M^{k-\frac{1}{2}}_{\left(i+\frac{1}{2},j\right)} \geq 0, \quad \lambda_{11}=0, \quad \lambda_{21}=1, \quad \lambda_{31}=-1 \qquad N^{k-\frac{1}{2}}_{\left(i+\frac{1}{2},j\right)} \geq 0, \quad \upsilon_{11}=0, \quad \upsilon_{21}=1, \quad \upsilon_{31}=-1$$

$$M^{k-\frac{1}{2}}_{\left(i+\frac{1}{2},j\right)} < 0, \quad \lambda_{11}=1, \quad \lambda_{21}=-1, \quad \lambda_{31}=0 \qquad N^{k-\frac{1}{2}}_{\left(i+\frac{1}{2},j\right)} < 0, \quad \upsilon_{11}=1, \quad \upsilon_{21}=-1, \quad \upsilon_{31}=0$$

$$M^{k-\frac{1}{2}}_{\left(i,j+\frac{1}{2}\right)} \geq 0, \quad \lambda_{12}=0, \quad \lambda_{22}=1, \quad \lambda_{32}=-1 \qquad N^{k-\frac{1}{2}}_{\left(i,j+\frac{1}{2}\right)} \geq 0, \quad \upsilon_{12}=0, \quad \upsilon_{22}=1, \quad \upsilon_{32}=-1$$

$$M^{k-\frac{1}{2}}_{\left(i,j+\frac{1}{2}\right)} < 0, \quad \lambda_{12}=1, \quad \lambda_{22}=-1, \quad \lambda_{32}=0 \qquad N^{k-\frac{1}{2}}_{\left(i,j+\frac{1}{2}\right)} < 0, \quad \upsilon_{12}=1, \quad \upsilon_{22}=-1, \quad \upsilon_{32}=0$$

The values for λ_{ij}, ν_{ij}, $D^{k-\frac{1}{2}}_{\left(i+\frac{1}{2},j\right)}$ and $D^{k-\frac{1}{2}}_{\left(i,j+\frac{1}{2}\right)}$ are presented as follows:

$$D^{k-\frac{1}{2}}_{\left(i+\frac{1}{2},j\right)} = \frac{1}{4}\left(D^{k}_{(i+1,j)} + D^{k-1}_{(i+1,j)} + D^{k}_{(i,j)} + D^{k-1}_{(i,j)}\right) = h_{\left(i+\frac{1}{2},j\right)} + \frac{1}{4}\left(\eta^{k}_{(i+1,j)} + \eta^{k-1}_{(i+1,j)} + \eta^{k}_{(i,j)} + \eta^{k-1}_{(i,j)}\right)$$

$$D^{k-\frac{1}{2}}_{\left(i,j+\frac{1}{2}\right)} = \frac{1}{4}\left(D^{k}_{(i,j+1)} + D^{k-1}_{(i,j+1)} + D^{k}_{(i,j)} + D^{k-1}_{(i,j)}\right) = h_{\left(i,j+\frac{1}{2}\right)} + \frac{1}{4}\left(\eta^{k}_{(i,j+1)} + \eta^{k-1}_{(i,j+1)} + \eta^{k}_{(i,j)} + \eta^{k-1}_{(i,j)}\right)$$

3.3.2.2 APPROXIMATION OF FRICTION TERMS.

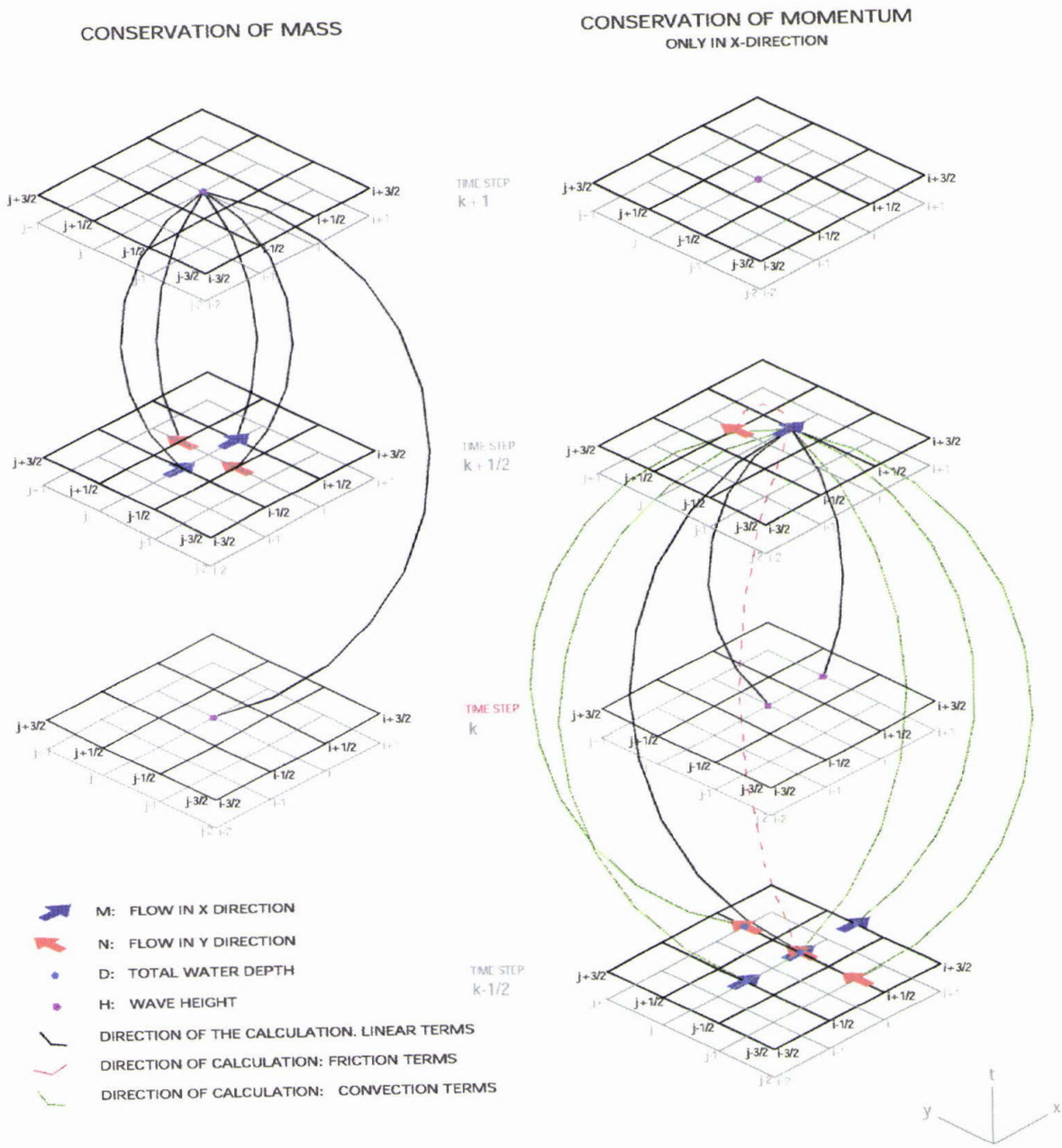
Friction terms in equation (3.6.*b*) and (3.6.*c*) are discretised with an implicit scheme to avoid instabilities (to solve the square root terms), as follows:

(3.19.*a*)
$$\frac{g\,n^2}{D^{7/3}} M\sqrt{M^2+N^2} = \frac{g\,n^2}{\left(D^{k-\frac{1}{2}}_{\left(i+\frac{1}{2},j\right)}\right)^{7/3}} \frac{1}{2}\left(M^{k+\frac{1}{2}}_{\left(i+\frac{1}{2},j\right)} + M^{k-\frac{1}{2}}_{\left(i+\frac{1}{2},j\right)}\right)\sqrt{\left(M^{k-\frac{1}{2}}_{\left(i+\frac{1}{2},j\right)}\right)^2 + \left(N^{k-\frac{1}{2}}_{\left(i+\frac{1}{2},j\right)}\right)^2}$$

(3.19.*b*)
$$\frac{g\,n^2}{D^{7/3}} N\sqrt{M^2+N^2} = \frac{g\,n^2}{\left(D^{k-\frac{1}{2}}_{\left(i,j+\frac{1}{2}\right)}\right)^{7/3}} \frac{1}{2}\left(N^{k+\frac{1}{2}}_{\left(i,j+\frac{1}{2}\right)} + N^{k-\frac{1}{2}}_{\left(i,j+\frac{1}{2}\right)}\right)\sqrt{\left(M^{k-\frac{1}{2}}_{\left(i,j+\frac{1}{2}\right)}\right)^2 + \left(N^{k-\frac{1}{2}}_{\left(i,j+\frac{1}{2}\right)}\right)^2}$$

The computation sequence for the non-linear long wave theory is presented in Figure 3.5.

FIGURE 3.5.- THE LEAP-FROG SCHEME: NON LINEAR LONG WAVE THEORY



3.3.3 INITIAL CONDITIONS

The initial water level is assumed constant and equal to the MSL. Horizontal water velocities and the vertical displacement of the sea surface are set to zero. These assumptions are expressed in set (3.20).

$$(3.20.a) \quad \eta_{(i,j)}^{k-1} = 0$$

$$(3.20.b) \quad M_{\left(i+\frac{1}{2},j\right)}^{k-\frac{1}{2}} = 0$$

$$(3.20.c) \quad N_{\left(i,j+\frac{1}{2}\right)}^{k-\frac{1}{2}} = 0$$

The initial bed deformation (Section 3.4.3) will determine the wave profile immediately after the initiation of the model. Abe (1973) stated that the vertical displacement of the ocean crust is approximately equal to the initial tsunami height throughout the boundary of the rupture zone. Shuto (1991) considered that this is a good approximation when the source is large compared to the water depth and an impulsive mechanism governs the earthquake.

3.3.4 BOUNDARY CONDITIONS

3.3.4.1 OFFSHORE BOUNDARY CONDITION

It is assumed that tsunami energy is transmitted outward in the deep sea with minimal reflection in the open boundary. This is achieved with the use of the method of characteristics at the boundary, extended from the linear long wave in a channel of constant depth. Set of equations 3.6 are reduced to:

$$(3.21.a) \quad \frac{\partial \eta}{\partial t} + \frac{\partial M}{\partial x} = 0 \quad \Big/ \cdot \sqrt{\frac{g}{D}}$$

$$(3.21.b) \quad \frac{\partial M}{\partial t} + gD\frac{\partial \eta}{\partial x} = 0 \quad \Big/ \cdot \frac{1}{D}$$

$$\Rightarrow$$

$$(3.22.a) \quad \frac{\partial}{\partial t}\left(\sqrt{\frac{g}{D}}\eta\right) + \sqrt{gD}\frac{\partial u}{\partial x} = 0$$

$$(3.22.b) \quad \frac{\partial u}{\partial t} + \sqrt{gD}\frac{\partial}{\partial x}\left(\sqrt{\frac{g}{D}}\eta\right) = 0$$

Addition and subtraction of these equations yield:

$$\left(\frac{\partial}{\partial t} \pm \sqrt{gD}\frac{\partial}{\partial x}\right)\left(u \pm \sqrt{\frac{g}{D}}\eta\right) = 0, \quad \text{which implies} \quad u \pm \sqrt{\frac{g}{D}}\eta = const. \quad \text{on} \quad \frac{dx}{dt} = \pm\sqrt{gD}\,.$$

Assume a wave train advancing towards the offshore boundary, in negative x direction (Figure 3.6).

$$(3.23.a) \quad u_2 + \sqrt{\frac{g}{D}}\eta_2 = u_1 + \sqrt{\frac{g}{D}}\eta_1 = 0$$

$$(3.23.a) \quad u_2 - \sqrt{\frac{g}{D}}\eta_2 = u_0 - \sqrt{\frac{g}{D}}\eta_0 = 0$$

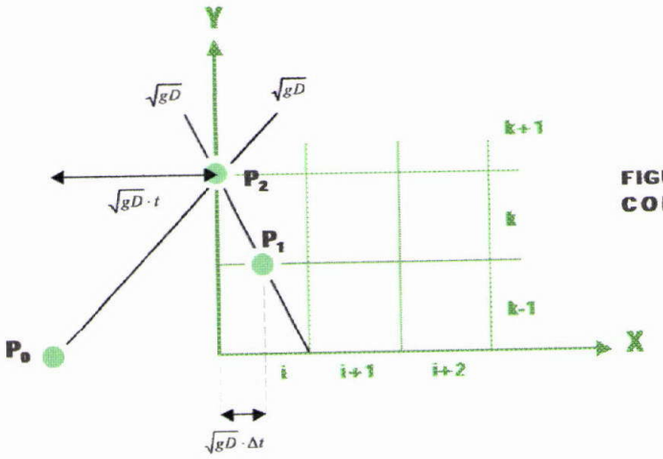


FIGURE 3.6.- OFFSHORE BOUNDARY CONDITIONS

Po is out of the domain of computation, thus $u_0 = 0$ and $\eta_0 = 0$. Addition of equations 3.23 yield the expression of the receding wave train:

$$(3.24) \quad u_2 = \frac{1}{2}\left(u_1 + \sqrt{\frac{g}{D}}\eta_1\right)$$

Integrating along the depth derives the expression for the discharge flux:

$$(3.25) \quad M^{k-\frac{1}{2}}_{\left(i+\frac{1}{2},j\right)} = \frac{1}{2}\left(M_1 + \sqrt{gD}\eta_1\right)$$

$$M_1 = \frac{1}{\Delta x}\left(\sqrt{gD}\cdot\Delta t\cdot M^{k-\frac{1}{2}}_{\left(i-\frac{1}{2},j\right)} + \left(\Delta x - \sqrt{gD}\cdot\Delta t\right)M^{k-\frac{1}{2}}_{\left(i+\frac{1}{2},j\right)}\right)$$

$$\eta_1 = \frac{1}{\Delta x}\left[\frac{1}{2}\left(\sqrt{gD}\cdot\Delta t - \frac{\Delta x}{2}\right)\left(\eta^k_{(i-1,j)} - \eta^{k-1}_{(i-1,j)}\right) + \frac{1}{2}\left(\frac{3}{2}\Delta x - \sqrt{gD}\cdot\Delta t\right)\left(\eta^k_{(i,j)} - \eta^{k-1}_{(i,j)}\right)\right]$$

In the 2-Dimensional model the method of characteristics is given on a characteristic surface. The direction of the positive characteristic is given by the resultant of $M(I,j,k+1/2)$ and $N(I,j,k+1/2)$.

3.3.4.2 RUN-UP BOUNDARY CONDITION

Coastal flooding is determined with the Iwasaki and Mano (1979) boundary condition[4]. The model compares the water level, as computed in the previous step, with the bottom height of the next landward cell (Figure 3.7). Water flow, will be allowed into that cell if the water level is higher than the bottom height. The condition assumes a straight line connecting the water level and the bottom height of the immediate dry cell. Run-up is taken into account only in the non-linear computation of grid D.

In grids A, B and C, the computation is carried out for water depths deeper than 0.1cm, and vertical walls are set instead of the actual slope in the continent. Besides, it should be noted beforehand that the offshore computation in Grids A, B and C assumes perfect reflection from the shoreline, the shape of which is therefore roughly approximated. The computed results in these grids are then reliable only in deep waters, where the effects of run-up and small-scale topography become unimportant.

Consequently, this research omits the use and interpretation of computed results in Grids A, B and C and is only focused in Grid D.

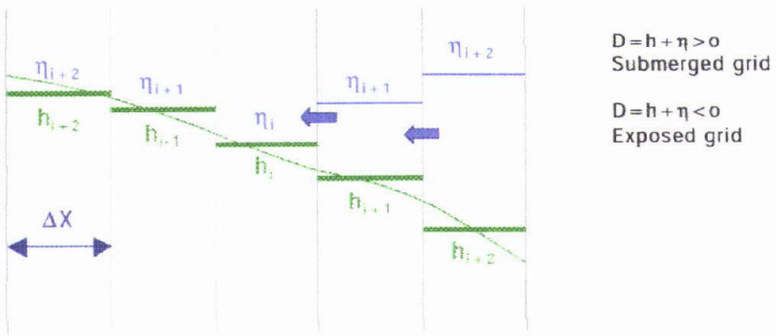


FIGURE 3.7.- RUN-UP BOUNDARY CONDITIONS (Iwasaki and Mano, 1979; cited by SHOA, 1999). Computation during run-up and rundown is dependent on whether the bottom condition is submerged or exposed.

---

[4] *Shuto stated (1990) that the run-up height computed with this method agrees with the theoretical solution with a 5% range of error if the condition* $\Delta x/\alpha g T^2 < 4x10^{-4}$ *is satisfied (*Δx *is the spatial grid length,* α *the angle of the slope, g the acceleration of gravity and T the tsunami period). In all the cases of analysis, this was largely accomplished.*

3.4 SOURCES OF DATA

This section presents the topo-bathymetric information required for the grids generation process and the seismologic data used to characterise the seismic events used in the simulation.

The numerical modelling region was selected considering the most conservative estimation for the 8TH July 1730 rupture zone (Table 3.3). Topo-bathymetric information was restricted to the area defined by 30°-37°S and 71°-74°W.

3.4.1 BATHYMETRY

The following hydrographic charts were provided by SHOA:

MAP N° / AREA	SCALE	LEFT BOTTOM CORNER		RIGHT TOP CORNER	
		Long. W	Lat. S	Long. W	Lat. S
N°424 Quintero Bay	1:10.000	71°33'	32°47'16''	71°28'34''	32°43'40''
N°4250 Quintero to Valparaíso	1:50.000	71°50'	33°03'40''	71°26'	32°40'00''
N°400 Coquimbo to Valparaíso	1:500.000	74°00'	33°20'	71°00'	29°40'
N°500 Valparaíso to Arauco Gulf	1:500.000	74°50'	37°20'	71°20'	32°40'

TABLE 3.1.- HYDROGRAPHIC CHARTS. Technical specifications are detailed in Appendix 7.

Charts were referenced to the LAT. For modelling purposes, soundings were defined as positive.

3.4.2 TOPOGRAPHY

The geographic chart of the area was available in AutoCad version and was plotted at a scale 1:5000 from which the land information was digitised. The map is attached in Appendix 11. The superposition of the topography and bathymetry required a selective work in order to match both sources of data in a smooth 3-Dimensional surface (Appendix 4).

3.4.3 SEISMOLOGIC DATA

The seismic parameters required to characterise the rupture zone and the initial wave profile in the Mansinha and Smylie method were the following (Figure 3.8):

PARAMETER	DEFINITION
Location	Projection of the southwestern corner of the rupture zone on the surface (co-ordinates in Grid A)
Length (L)	Dimension of the mayor axis of the fault plane
Width (W)	Dimension of the minor axis of the fault plane
Dislocation (u)	Mean relative displacement between plates
Depth (H)	Vertical distance between the origin of the rupture zone and the ocean bottom
Strike Angle (θ)	Direction of the principal axis of the fault measured clockwise from the North
Direction of dislocation (λ)	Direction of the relative displacement referred to the strike angle along the fault plane
Dip angle (δ)	Inclination of the fault plane with respect to the horizontal surface

TABLE 3.2.- DEFINITION OF THE RUPTURE ZONE PARAMETERS

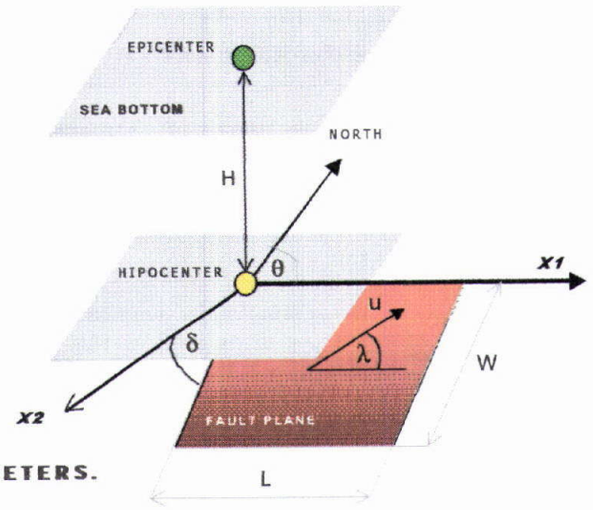


FIGURE 3.8.- RUPTURE PARAMETERS.

The seismological characteristics for the 1730 earthquake were obtained from Lomnitz (1970), Comte et al. (1986), Nishenko (1985), Kausel (1986), Pardo, Comte, and Eisemberg (1989), and SHOA (1999). The 1906 and 1985 earthquakes ware reproduced from the numerical simulation of Valparaíso (SHOA, 1999). The estimated bed deformation for the 1730 Earthquake is not known with the confidence of the events of 1906 and 1985. A summary of the relevant information used in the simulation is shown in Tables 3.3 and 3.4.

Crustal rigidity (μ) was selected as $4x10^{11}$din/cm^2 (Plafker, 1985; Lorca, 2001). The sensibility of the model to this factor was assessed with a preliminary analysis of results (being the rest of the variables *ceteris paribus*), which produced minor divergences.

PARAMETER	ESTIMATION
South-western corner of the rupture zone	36°S 73°W Grid A (23,23) *Pardo, Comte and Eisemberg, 1989* 34°S Grid A (67,112) *Nishenko, 1985*
Length (L)	350 – 450 km *Kausel, 1985* 550km *Comte et al., 1986* *Pardo, Comte and Eisemberg, 1989*
Width (W)	100-150km *Nishenko, 1985*
Dislocation (u)	6-8m *Nishenko, 1985*
Depth (H)	15 – 40 km *Lorca, 2001*
Strike Angle (θ)	N10°E *SHOA, 1999*
Direction of dislocation (λ)	90° *SHOA, 1999*
Dip angle (δ)	18° *SHOA, 1999*

TABLE 3.3.- PARAMETERS OF THE 8TH JULY 1730 EARTHQUAKE

PARAMETER	ESTIMATION **16TH AUGUST 1906**	ESTIMATION **3RD MAY 1985**
South-western corner of the rupture zone	34.9°S 72°W Grid A (67,72)	34.4°S 72°W Grid A (67,94)
Length (L)	330 km	200 km
Width (W)	130 km	90 km
Dislocation (u)	3.3 m	2.8 m
Depth (H)	15 km	15 km
Strike Angle (θ)	N10°E	N10°E
Direction of dislocation (λ)	90°	105°
Dip angle (δ)	18°	18°

TABLE 3.4.- PARAMETERS OF THE 1906 AND 1985 EARTHQUAKES

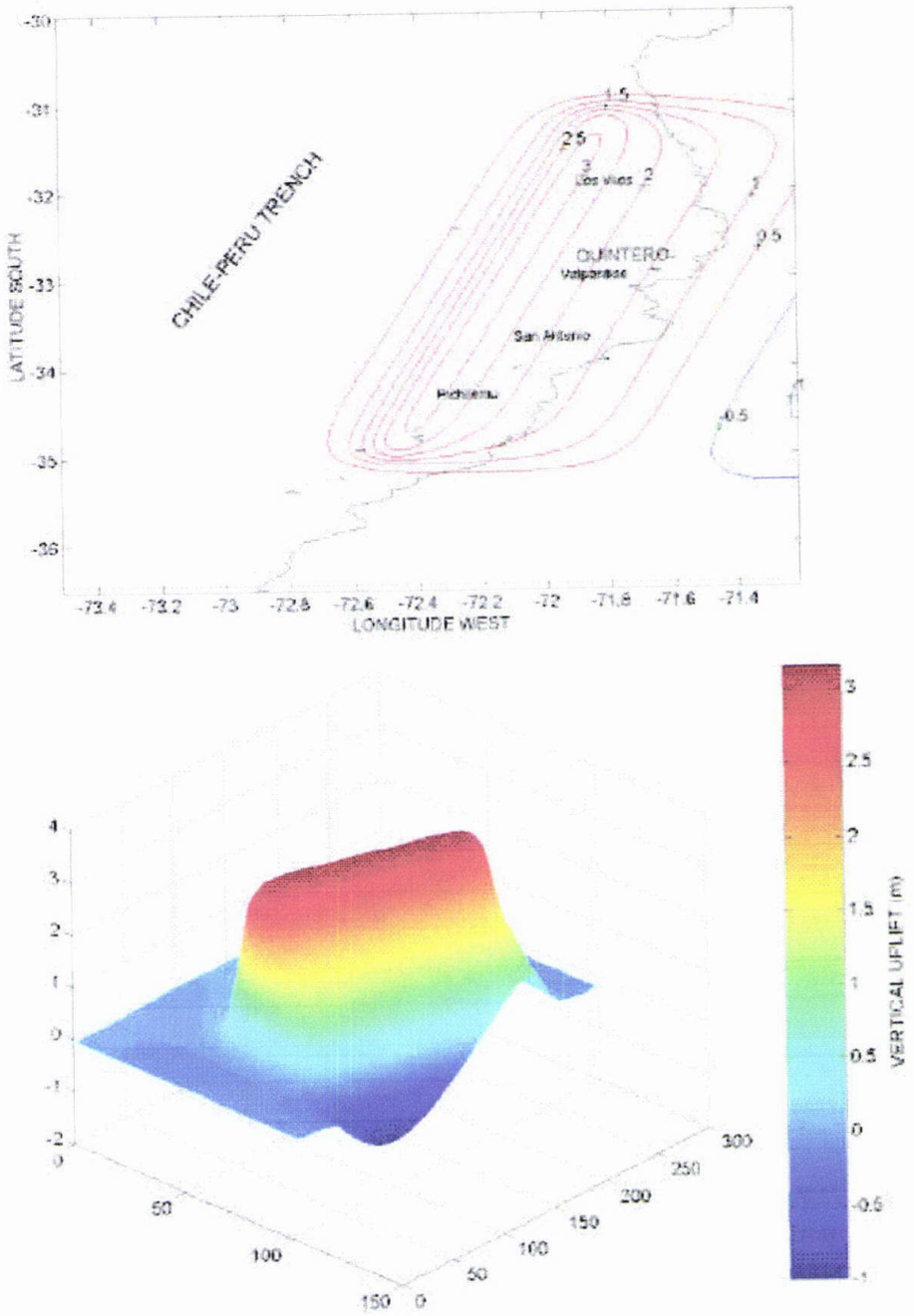
The vertical displacement of the sea bottom was calculated for the presented parameters with the Mansinha and Smylie method (1971), as an image of the ocean bottom displacement. For a dip-slip fault:

$$(3.21)\quad \frac{\partial h}{\partial t} = \mu U \int\left(\left(\frac{\partial u_i^{\,2}}{\partial \xi_2} - \frac{\partial u_i^{\,3}}{\partial \xi_3}\right) sen 2\delta - \left(\frac{\partial u_i^{\,2}}{\partial \xi_3} - \frac{\partial u_i^{\,3}}{\partial \xi_2}\right)\cos 2\delta\right)\partial\xi_2\,\partial\xi_3$$

δ: Dip angle
μ: Lame constant
$u_i^{\,j}$ i-st component of the displacement in (x_1,x_2,x_3) caused by a unitary force in (ξ_1,ξ_2,ξ_3), acting in the j-st direction

The distribution of uplift and subsidence in the source region is characterised by two approximately elliptical lobes, positive in the Western portion and negative towards the East, oriented with a longer axis in a North-South direction. The positive lobe presents bigger amplitudes than the negative one. Crustal deformations for all the cases of analysis are depicted in Appendix 6. Case 1730-10 is shown as a representative model in Figure 3.9. The Mansinha and Smylie method provides an estimation of the displacement of the ocean bottom, which might differs substantially from the real phenomena. Time dependency (i.e. the temporal propagation of the rupture) is not fairly reproduced in the initial slip displacement, assumption that may be representative of impulsive earthquakes but not precise in other cases.

FIGURE 3.9.- DISTRIBUTION OF UPLIFT AND SUBSIDENCE IN THE SOURCE REGION (GRID A). CASE 1730-10.



3.4.4 CASES ANALYSED

Numerical tests were performed to evaluate a range of possible scenarios representing the 8TH July 1730 earthquake. This process permitted as a by-product, the assessment the sensitivity of the model to the input variables required in the Mansinha and Smylie method.

The cases of analyses range from extreme scenarios to conservative ones, including the best estimation (1730-10). Cases 1906-1 and 1985-1 are also included in Table 3.5.

CASE	LENGTH (km)	WIDTH (km)	DISLOC. (m)	DEPTH (km)	STRIKE A. (deg)	DISL. AN. (deg)	DIP AN. (deg)
1730-1	550	150	8	15	N10°E	90°	18°
1730-2	550	150	8	15	N10°E	90°	20°
1730-3	550	150	8	15	N10°E	80°	18°
1730-4	550	150	8	15	N5°E	90°	18°
1730-5	550	150	8	40	N10°E	90°	18°
1730-6	550	150	6	15	N10°E	90°	18°
1730-7	550	100	8	15	N10°E	90°	18°
1730-8	350	150	8	15	N10°E	90°	18°
1730-9	350	150	6	40	N10°E	90°	18°
1730-10	450	125	7	15	N10°E	90°	18°
1906-1	330	130	3.3	15	N10°E	90°	18°
1985-1	200	90	2.8	17	N10°E	105°	18°

TABLE 3.5.- CASES OF ANALYSIS.

For the above-mentioned cases, maximum values of the vertical displacement of the sea bottom, calculated with the Mansinha and Smylie method, are presented in Table 3.6.

CASE	MAXIMUM UPLIFT IN RUPTURE ZONE (m)	MAXIMUM UPLIFT IN QUINTERO (cm)
1730-1	3.7	80
1730-2	3.7	87
1730-3	3.6	80
1730-4	3.6	12
1730-5	3.2	58
1730-6	2.7	60
1730-7	3.5	106
1730-8	3.7	260
1730-9	2.2	176
1730-10	3.2	126
1906-1	1.5	67
1985-1	1.5	79

TABLE 3.6.- MAXIMUM UPLIFT ON EACH CASE.

3.5 GRIDS GENERATION

The regional model was divided into 4 sub-regions, Grids A, B, C and D, with a constant time step of 1(s) and spatial increments of 81" (2498 m), 27" (833 m), 9" (278 m) and 3" (93 m) respectively. Applying a nested scheme is an efficient technique to reduce CPU time and to have satisfactory spatial resolution in Quintero[5].

The procedure used the computed results of the coarser grids in the inner ones by linear interpolation to compute the input values to the finer grids. The limits of the grids were proposed using the following criteria:

- Grid A was selected in order to embody the most conservative scenario for the rupture zone of the 8TH July 1730 earthquake (Pardo, Comte and Eisemberg, 1989), defined by 30°S to 37°S and 71°W to 74°W. This grid was set with an open boundary in the deep sea where boundary conditions were given.

- Grid D circumscribed Quintero Bay and all the topographical features below 25 metres MSL, including the southern Península Los Molles and Pta. Lunes at the north of the bay (Chart 424, Appendix 7). Based on the previous study of tsunami risk in Quintero (Pilasi, 1978), 25 m above MSL is a conservative elevation to evaluate the flooding line within Quintero Bay.

- Grids B and C were defined following a similar pattern of the 16TH August 1906 simulation in Valparaíso (SHOA, 1999) which showed successful results.

The model grids were oriented in the North-East direction. This orientation, selected because of the limitations of the digitation software available in SHOA (Appendix 4), does not coincides with the principal axis of the rupture zone, estimated in N5°E to N10°E. Although it is generally recommended to locate the grid parallel to the approaching wavefront on each grid, only slight numerical disturbances should be expected with this 5° to 10° discrepancy.

---

[5] *The use of a fine grid in the whole regional model (Grid A) would dramatically increase the computational grid points (thus computer time and memory). Besides this, many of these points are located in areas of limited interest.*

The space increment in Grid A (81") was selected in order to cover one tsunami wavelength by more than 20 grid points and at least 50 grid points at the run-up front (Shuto, 1991). The time step of 1 s was selected according to the Courant number:

$$C_R = c\frac{\Delta t}{\Delta x}$$

Δt: *Time step*
Δx: *Space increment*
c: *Celerity*
g: *Acceleration of gravity*

The Courant number expresses how many grid points the information moves in every time step (as the information travels at a speed corresponding to the celerity). A conservative condition to guarantee the stability of the algorithm is:

$$\Delta t < \frac{\Delta x}{\sqrt{2gh_{max}}}$$

Δt: *Time step*
Δx: *Space increment*
g: *Acceleration of gravity*
h_{max}: *Maximum depth in a particular grid*

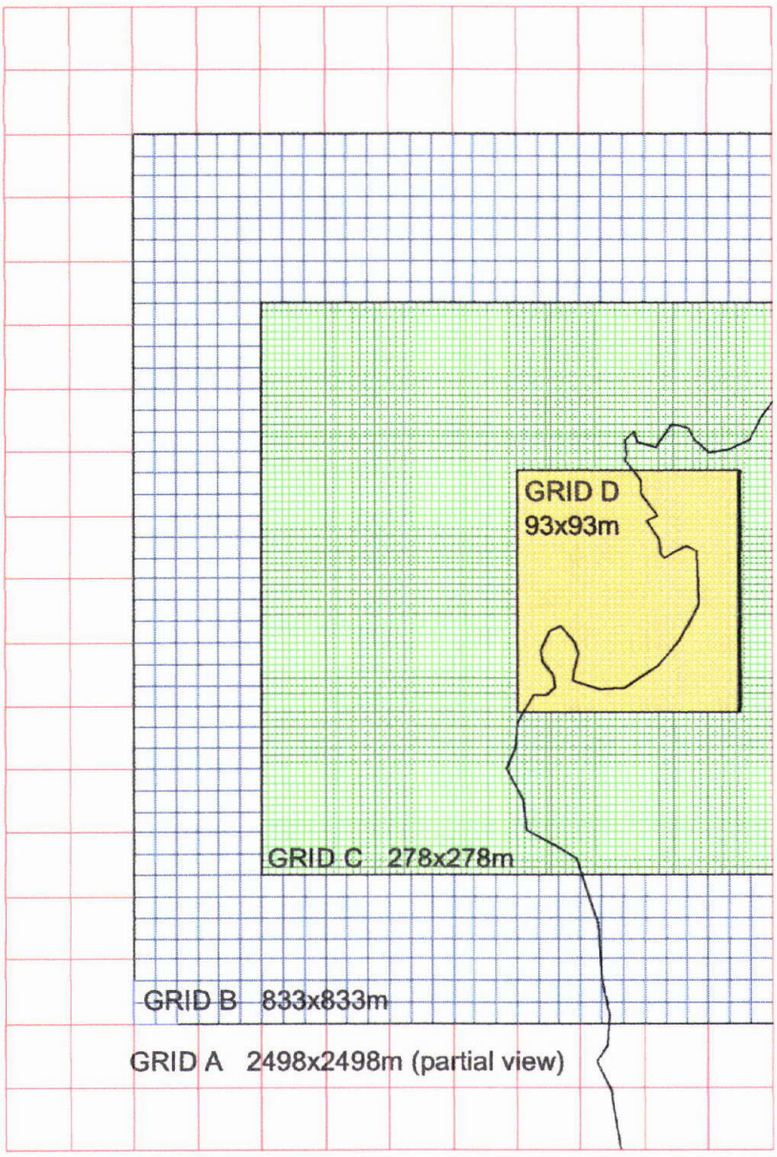
The stability condition is achieved for each grid, as shown in Table 3.7.

GRID	Δt (s)	Δx (m)	h_{max} (m)	$\Delta t < \frac{\Delta x}{\sqrt{2gh_{max}}}$
A	*1*	*2498*	*7600*	*1 < 6.5* ✓
B	*1*	*833*	*730*	*1 < 7.0* ✓
C	*1*	*278*	*421*	*1 < 3.1* ✓
D	*1*	*93*	*119*	*1 < 1.9* ✓

TABLE 3.7.- COURANT´S STABILITY CONDITION.

A partial view of grids A, B, C and the entire grid D is shown in Figure 3.10.

FIGURE 3.10.- PARTIAL VIEW OF GRIDS A, B, C AND GRID D



Grids limits were the following:

GRID	LEFT BOTTOM CORNER		RIGHT TOP CORNER	
	LONGITUDE	LATITUDE	LONGITUDE	LATITUDE
A	-73.5133°	-36.5133°	-71.2183°	-29.9658°
B	-71.7058°	-32.9058°	-71.3008°	-32.5908°
C	-71.6508°	-32.8508°	-71.3508°	-32.6483°
D	-71.5500°	-32.8000°	-71.4725°	-32.7150°

TABLE 3.8.- DIMENSIONS FOR THE GRIDS, IN GEOGRAPHICAL CO-ORDINATES.

The space increment and points of computation of each grid is summarised in Table 3.9.

GRID	SPACE INCREMENT		POINTS OF COMPUTATION	
			I	J
A	81''	(2498 m)	103	292
B	27''	(833 m)	55	43
C	9''	(278 m)	121	82
D	3''	(93 m)	94	103

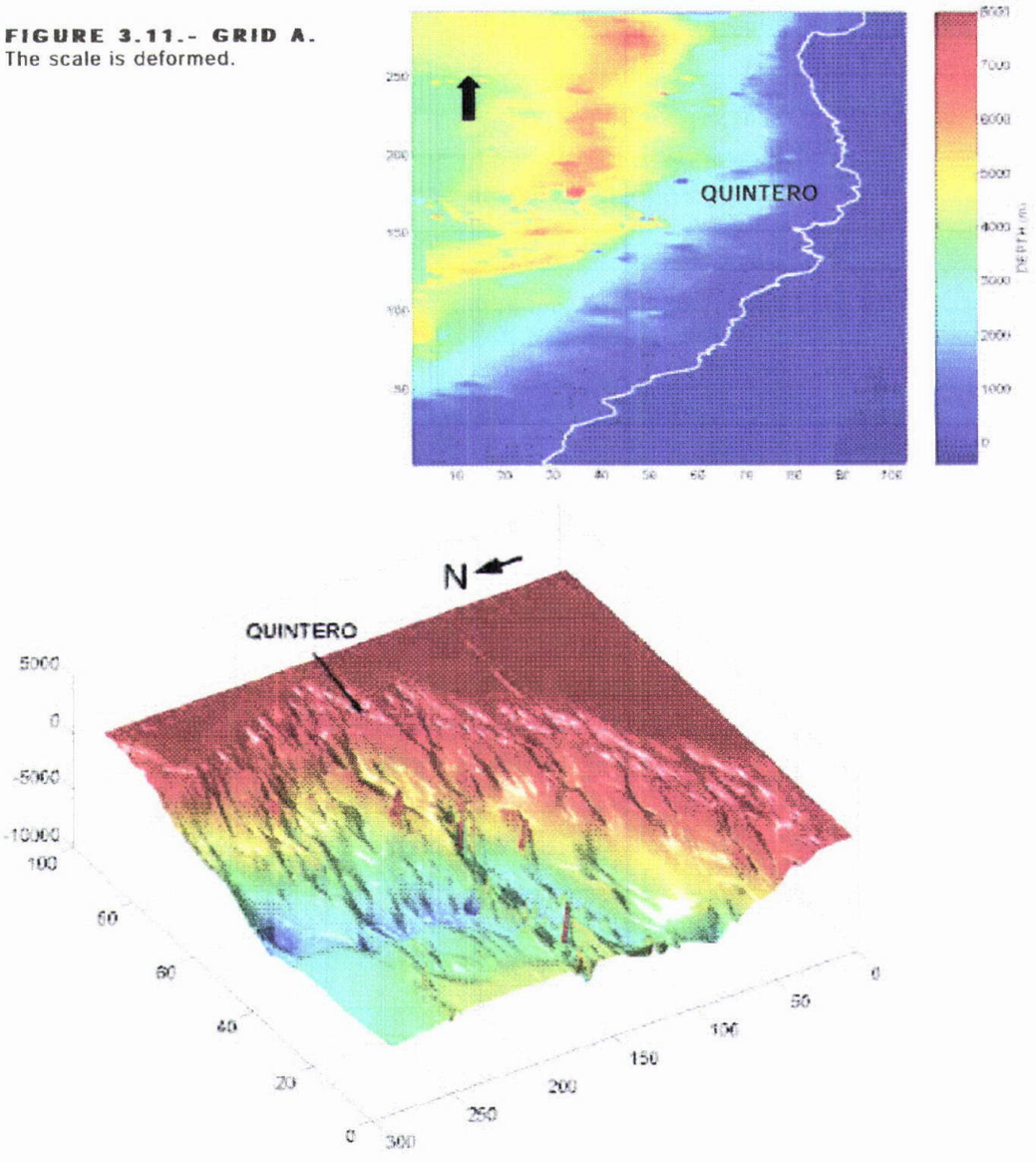
TABLE 3.9.- SPACE INCREMENTS AND GRID POINTS.

The digitised information was smoothed to avoid artificial singularities that could produce errors in the simulation.

3.5.1 DIGITATION OF GRID A

Grid A was built as an assemblage of already digitised data, used in the numerical simulation of the 16TH August 1906 tsunami in Valparaiso (SHOA, 1999) and information obtained from hydrographic charts N°400 and N°500 (Details of the procedure are found in Appendix 4).

FIGURE 3.11.- GRID A.
The scale is deformed.



3.5.2 DIGITATION OF GRIDS B AND C

The digitisation of grids B and C was based on Chart N°4250. The altitudes were assumed constant (100 m MSL) in both cases.

FIGURE 3.12.- GRID C. The horizontal scale is deformed.

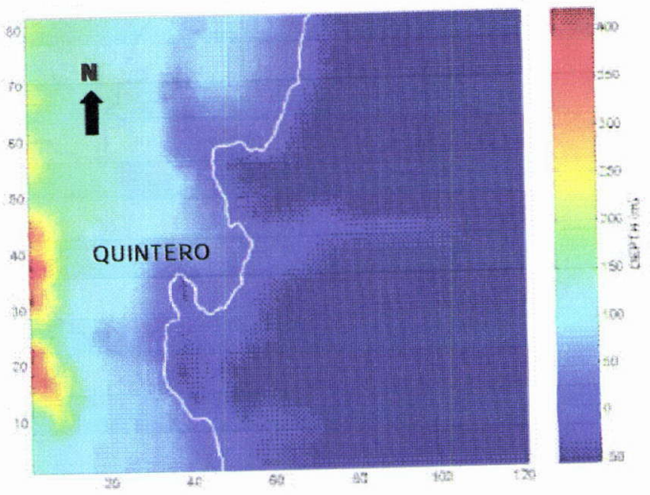
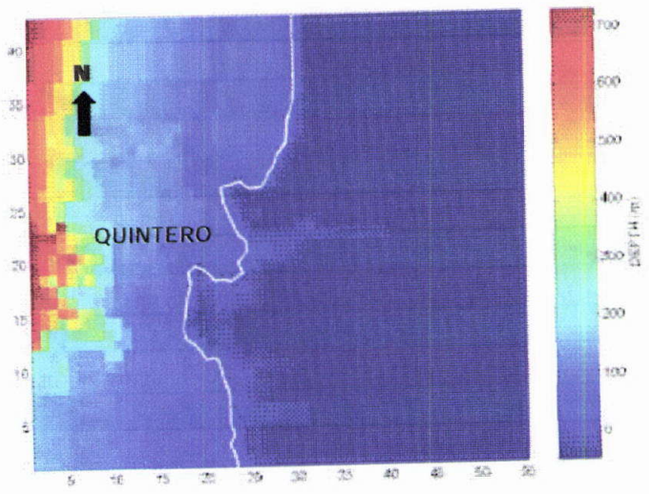


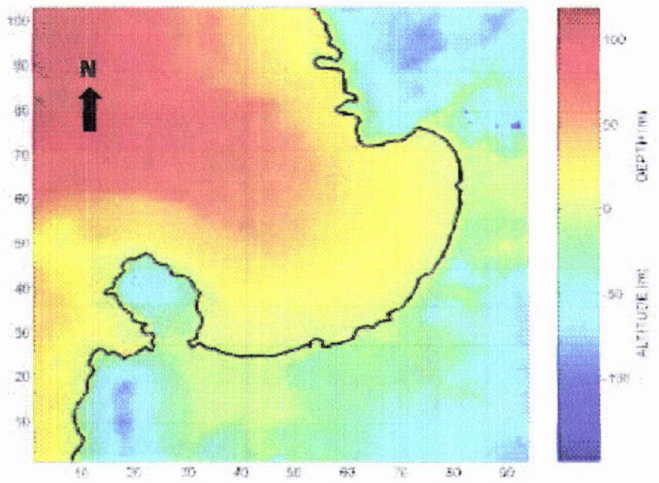
FIGURE 3.13.- GRID B. The horizontal scale is deformed.

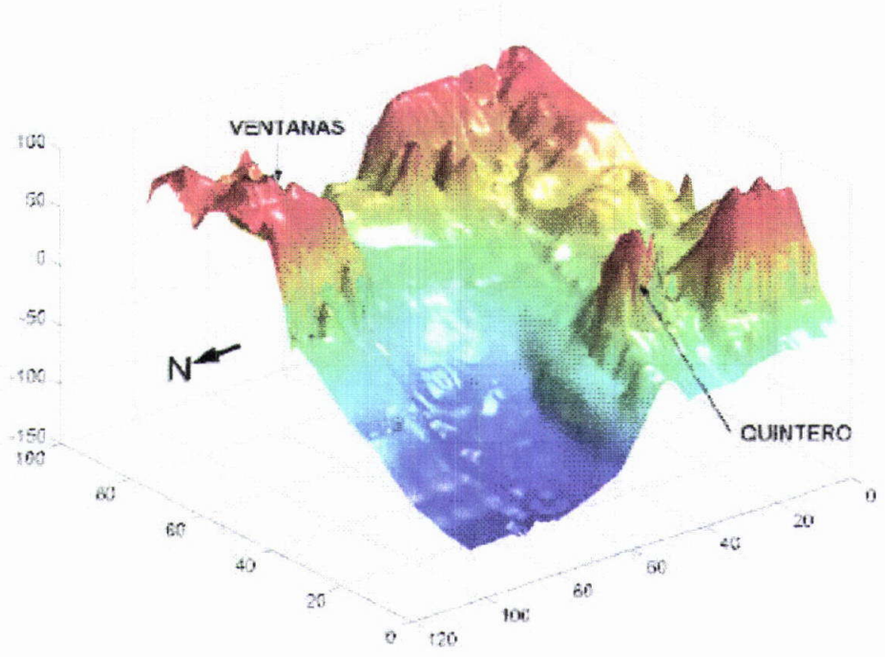


3.5.3 DIGITATION OF GRID D

The digitisation of Quintero Bay was based on topographic information and Chart N°424, using special software and equipment (Appendix 4). The superposition of topography and bathymetry required the removal of overlapped points along the coastline, caused by the different surveying techniques, chart datum, geographic references and data processes used in their production.

FIGURE 3.14.- GRID D.
(The scale is deformed)





3.6 CALIBRATION

The validation of the hydrodynamic model was preceded by a calibration procedure using tide-gauge information from the 3RD March 1985 earthquake, considered as a well-documented historical event. At the moment, the calibration process is not possible with in situ information in Quintero because there are no records in the bay.

As a consequence, the calibration was achieved with information collected in the closer station, Valparaíso, using data obtained in the local mareograph for the 1985 earthquake (Figure 3.15). This event is in fact a thoroughly studied earthquake with regards to its seismic parameters and is the only important near-field tsunami registered in Valparaíso.

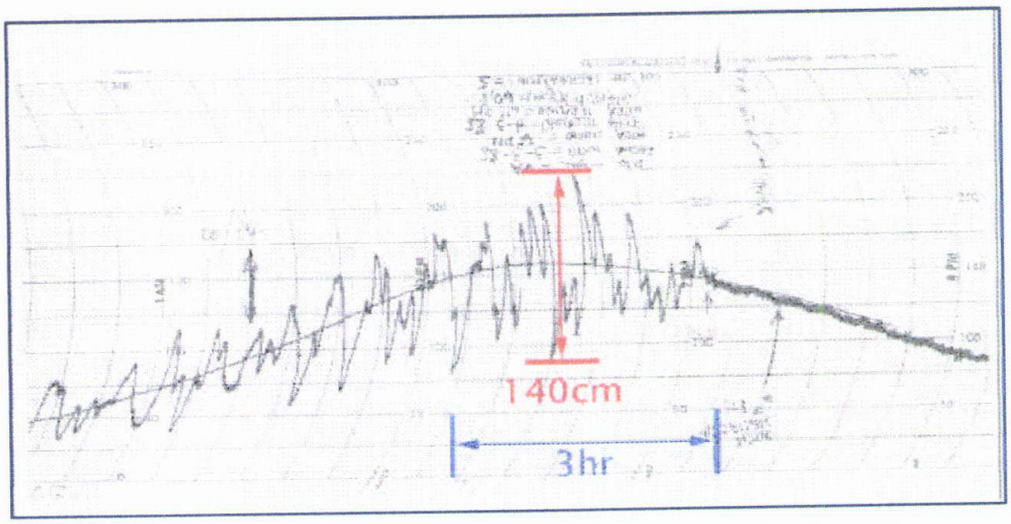


FIGURE 3.15.- ORIGINAL 1985 TSUNAMI RECORD IN VALPARAISO .

The record shows that the maximum peak coincided with high tide approximately 2 h after the earthquake shock and secondary undulations, probably caused by resonance were experimented for about 24 h. The maximum wave heights (i.e. difference between two consecutive peaks and troughs) computed with TUNAMI-N in a hypothetical station located outside Valparaíso bay was of about 115 cm. This value, compared with the 140 cm registered in the original record offshore, showed a relative decrease of 17%.

This is a good quality result which allows an estimation of the accumulated numerical error in tsunami run-ups of the model in Quintero. Results are similar to previous simulations where final error in the run-up of well-documented tsunamigenic earthquakes was usually about 15% (Shuto, 1991).

Tsunami run-up will consequently be strongly conditioned by the initial bed displacement, estimated according to the current knowledge on the seismic features of the Chile-Peru Trench. Larger errors would eventually be conditioned by an inadequate estimation of the seismic features of the seismic event used on each particular simulation but would not fully rely of the numerical code.

CHAPTER 4
RESULTS

4.1 GENERAL REMARKS

This chapter presents the analysis and discussion of the modelling results for various scenarios in the form of 2-Dimensional predictions of the wave evolution, displaying elevations and velocity fields during a 180-min simulation. Graphic-aided video animations were produced in Matlab 5.3 to present the dynamic evolution of ***a)*** wave amplitudes in grids A and D and ***b)*** velocity fields in Grid D[1].

Numerical tests were performed to investigate the effects of the variables required by the Mansinha and Smylie method in the final wave amplitudes in Quintero, analysis that permitted the election of the most probable scenario for the 1730 e vent (Section 4.2). Time history was then represented by 2-D diagrams for grids A (Section 4.3.1) and D (Section 4.3.2) and through hypothetical marigrams predicting wave evolution for the 1730 event within the bay. The expected flooding, estimated as the maximum horizontal penetration of the wave, was calculated for the 1730, 1906 and 1985 events (Section 4.4). These results permitted the elaboration of tsunami flooding maps for the three events and a qualitative classification of flooding risk in terms of the seismic moment (Section 4.5). A site-specific set of recommendations was then proposed, including evacuation routes and safety areas were people should be evacuated under tsunami threat.

The computation time for a 3-h simulation -with a time step of 1second and graphical displays every 5 min- was of 20 min, as computed with a AMD Duron processor 750MHz and 120Mb of RAM. The whole package of executable and output files for a single case spent 25Mb of ROM. Video animations were produced with an enhanced resolution which required 309Mb of ROM. In total, 16 cases were performed in the simulation process, accounting 740 Mb of ROM[2].

---

[1] *The edition of the graphical outputs and animations require basic knowledge in Matlab 5.3 graphic facilities that, for time benefit, are not explained in this project. Executable files (*.m) are included in the CD ROM.*

[2] *Only 12 cases were mentioned in Chapter 3. Other models were employed to assess numerical stability in long term simulations (1730-11), the sensibility to Manning's roughness coefficient (1730-12 and 1730-13) and to produce video animations (1730-14).*

4.2 SENSITIVITY ANALYSIS

Numerical tests were performed to assess the sensitivity of the model to the input variables required in the Mansinha and Smylie method. The near shore propagation and run-up of the wave front was calculated for each case during a 3-h period with a time increment of 1 s. Sensitivity analysis was executed through hypothetical marigrams obtained in S1, co-ordinate (5.98), at a depth approximately 100 m in the entrance of the bay so as to avoid the influence of coastal reflection (Figure 4.1).

Table 4.1 illustrates the maximum wave height of the sea level throughout the computation, H_{MAX}, calculated for cases 1730-1 to 1730-8[3]. The parameter ΔH_{MAX}, defined as:

$$\Delta H_{MAX} = \left(\frac{H_{MAX\_CASE\_i} - H_{MAX1730\text{-}1}}{H_{MAX1730\text{-}1}} \right) \times 100$$

was adopted for the assessment of the sensitivity of the final wave elevations to each tested parameter.

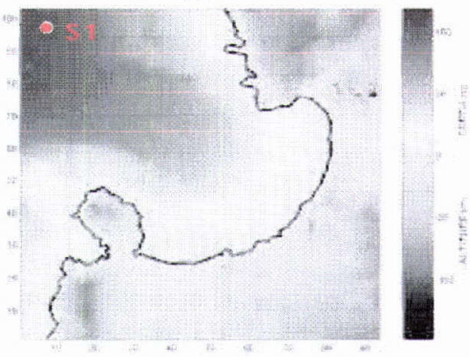


FIGURE 4.1 LOCATION OF THE MARIGRAM.

CASE	H_{MAX} (m)	TESTED PARAMETER	REFERENCE VALUE [1]	TEST VALUE	ΔH_{MAX}
1730-1	*3.84*	[1]			
1730-2	*3.98*	*Dip Angle*	*18°*	*20°*	*+4%*
1730-3	*3.54*	*Disl. Angle*	*90°*	*80°*	*- 8%*
1730-4	*4.63*	*Strike Angle*	*N10°E*	*N5°E*	*+21%*
1730-5	*4.22*	*Depth*	*15km*	*40km*	*+20%*
1730-6	*2.80*	*Dislocation*	*8m*	*6m*	*- 27%*
1730-7	*4.53*	*Width*	*150km*	*100km*	*+18%*
1730-8	*3.16*	*Length*	*550km*	*350km*	*- 17%*

TABLE 4.1.- SENSITIVITY OF WAVE HEIGHT RESULTS TO INPUT VARIABLES.
[1]: Reference values for case 1730-1 are found in Table 3.5.

[3] Model 1730-1 was arbitrarily assumed as the standard case. It is not intended to provide a final judgement of the resulting wave amplitudes and velocities since it is oriented only to assess the sensitivity of the final wave heights to each parameter.

Figure 4.2 depicts the above-mentioned results. Maximum elevations for each case are compared with the reference model 1730-1 and the adopted one 1730-10 (which election will be explained at the end of this section).

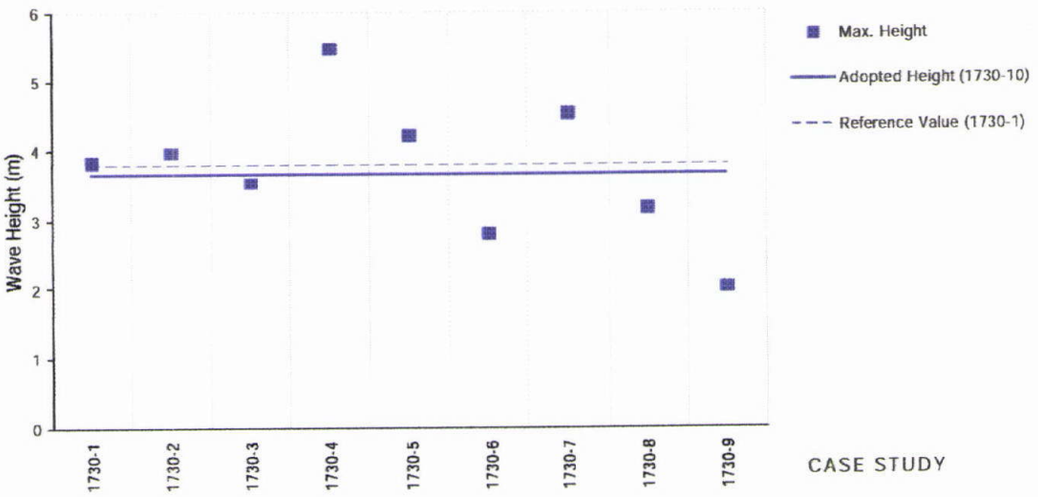


FIGURE 4.2.- MAXIMUM ELEVATIONS IN GRID POINT (5,98), GRID D.

A specific analysis for each parameter is discussed as follows:

DIP ANGLE (1730-2)

The maximum water surface height is not very sensitive to variations in the dip angle. As seen in Table 4.1, an increase from 18° to 20° implies a growth of only 0.14 m in the maximum height ($\Delta H_{MAX} = +4\%$). This rise is expected since a steeper fault plane is associated to larger magnitudes of the vertical component of the bed displacement, which actually produce tsunami waves. The quantitative effect of this variation is nevertheless, very low.

DISLOCATION ANGLE (1730-3)

A variation of 10° in the dislocation angle generates a minor reduction of 0.30 m in the maximum height ($\Delta H_{MAX} = -8\%$). The considerable similarity in time history between cases 1730-1, 1730-2 and 1730-3 indicates that the flooding is not sensitive to the dip and dislocation angles (Figure 4.3).

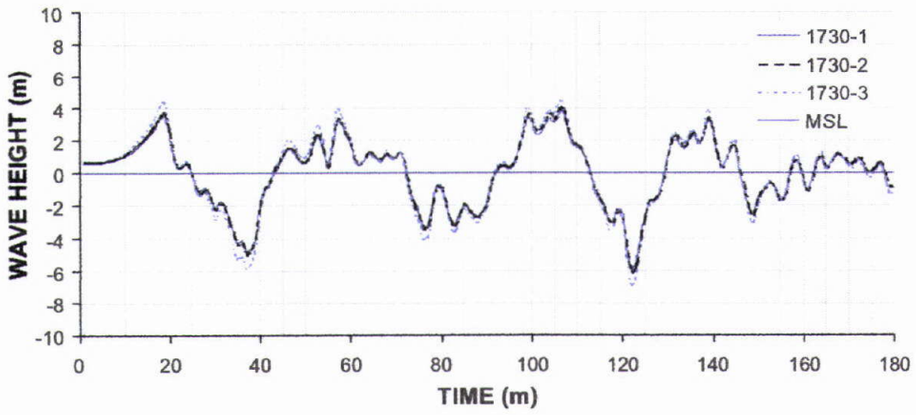


FIGURE 4.3.- MARIGRAMS FOR CASES 1730-1, 1730-2 AND 1730-3. STATION S1.

STRIKE ANGLE (1730-4)

Wave elevations are highly dependent to variations on the strike angle: a change from N10°E to N5°E in the orientation of the principal axis of the rupture zone produces a considerable amplification of 0.79 m in the maximum height compared to the standard case ($\Delta H_{MAX} = +21\%$). The first peak gets retarded approximately 3 min with respect to the standard case because of the larger extension that the leading wave has to travel before reaching the coastline (Figure 4.5). This scenario however, is unlikely to occur because of the orientation of the Benioff plane in central Chile, estimated as N10°E.

At this point it should be stated that hypothetical rupture zones were located so that their principal axis was almost parallel to the coast, allowing slight variations by as much as ±5° (Appendix 6). The advance direction of the wavefronts was therefore almost perpendicular to the coast.

DEPTH (1730-5)

It is generally accepted that shallow earthquakes have a tendency to infringe a larger portion of the seismic energy to the overlaying body of water than deep earthquakes, thus resulting in higher waves (Lorca, personal communication, 2001). This effect is not well predicted by the model. Figure 4.4 shows that as the depth increases from 10 to 40 km, maximum elevations tend to increase whereas for deeper focus, wave elevations decrease. This seems to be contradictory to the general conviction that deep-focus earthquakes (i.e. depth > 60 km) would have negligible tsunamigenic potential, and should be reviewed in the future.

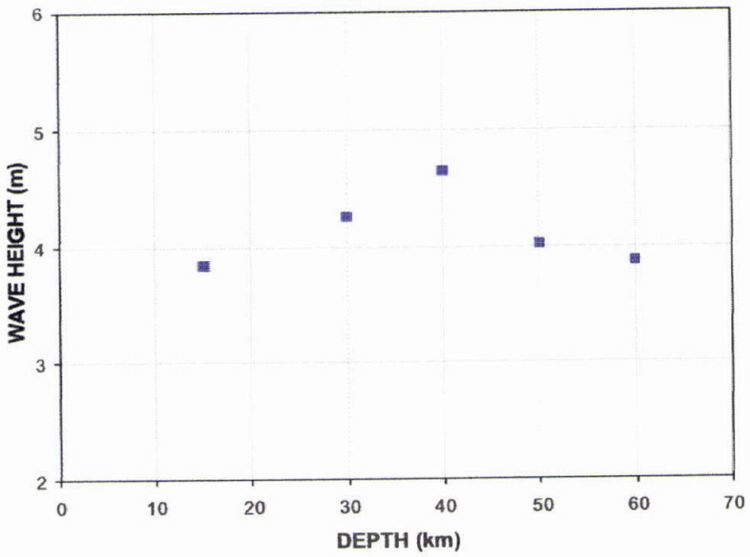


FIGURE 4.4.- MAXIMUM HEIGHT V/S DEPTH

Time history for cases 1730-4 and 1730-5 is shown in Figure 4.5.

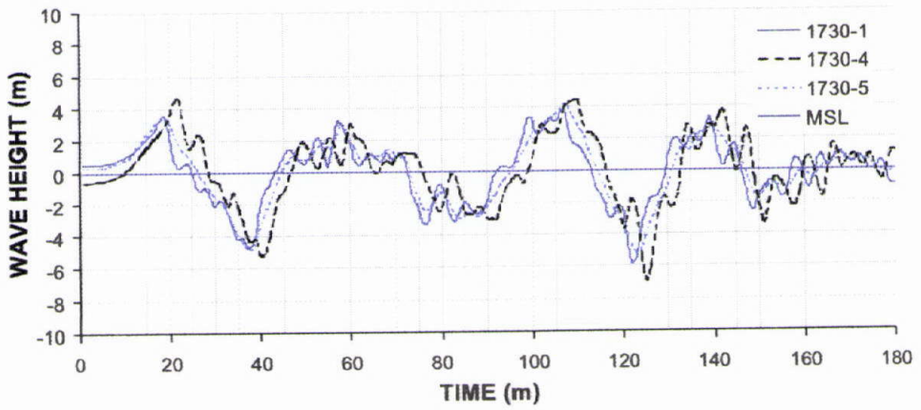


FIGURE 4.5.- MARIGRAMS FOR CASES 1730-1, 1730-4 AND 1730-5. STATION S1.

DISLOCATION (1730-6)

Dislocation is a critical parameter in final tsunami wave elevations. As noticed in Table 4.1, a reduction from 8m to 6m in the average dislocation of the rupture zone induces a considerable 1.04m reduction in the wave height (ΔH_{MAX} =-27%). Special concern was thus taken during the 1730 tsunami simulation before adopting the final value (Table 4.2), by assuming a range of possible scenarios for the mean dislocation.

RUPTURE WIDTH (1730-7)

Variations in the rupture width are moderately decisive in the final tsunami features. A reduction from 150km to 100km implies an increase of 0.69m in the maximum surface elevation (ΔH_{MAX} =+18%) probably caused by the concentration of energy in steeper wave profiles. Time history shows a similar behaviour in the occurrence of long period waves but a significant difference in short period oscillations. Cases 1730-6 and 1730-7 are shown in Figure 4.6.

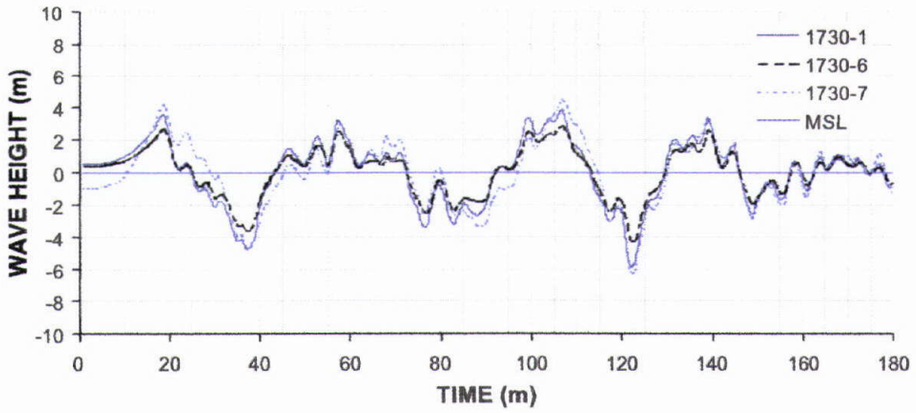


FIGURE 4.6.- MARIGRAMS FOR CASES 1730-1, 1730-6 AND 1730-7. STATION S1.

RUPTURE LENGTH (1730-8)

Alterations in the rupture length are associated with moderate differences in computed wave elevations. In fact, a considerable 200 km decrease in the length induces the reduction of about 1.03 m in the maximum elevations (ΔH_{MAX} =+17%). As seen in Figure 4.7, length reduction results in a temporal relocation of the wave peaks and in a moderate attenuation of tsunami wave amplitudes but maintains the characteristics of short period waves.

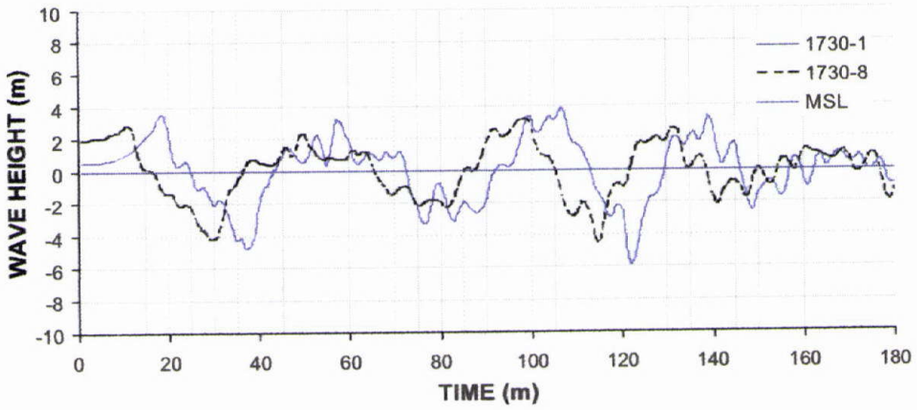


FIGURE 4.7.- MARIGRAMS FOR CASES 1730-1 AND 1730-8. STATION S1.

Based on the previous analysis, case 1730-10 was adopted as the most representative model for the 8TH July 1730 tsunami. The parameters are shown in Table 4.2 and were selected based on the following criteria derived from Section 3.4.3:

- The rupture length was chosen as a compromise between the estimations provided by Kelleher (1972), Kausel (1985) and Pardo, Comte and Eisemberg (1989).
- The dislocation and rupture width were selected according to the values suggested by Nishenko (1985).
- A depth of 15 Km was selected as representative for shallow earthquakes in the Chile-Peru Trench (Lorca, personal communication, 2001).
- The dip, dislocation and strike angles were chosen from the current knowledge from the seismotectonic features of the Chile-Peru Trench (SHOA, 1999) and considering the low sensitivity the model shows with these parameters.

CASE	Length (km)	Width (km)	Disloc. (m)	Depth (km)	Strike an. (deg)	Disl. An. (deg)	Dip an. (deg)
1730-10	*450*	*125*	*7*	*15*	*N10°E*	*90°*	*18°*

TABLE 4.2.- PARAMETERS FOR THE 1730 EARTHQUAKE.

4.3 TIME HISTORY

4.3.1 GRID A

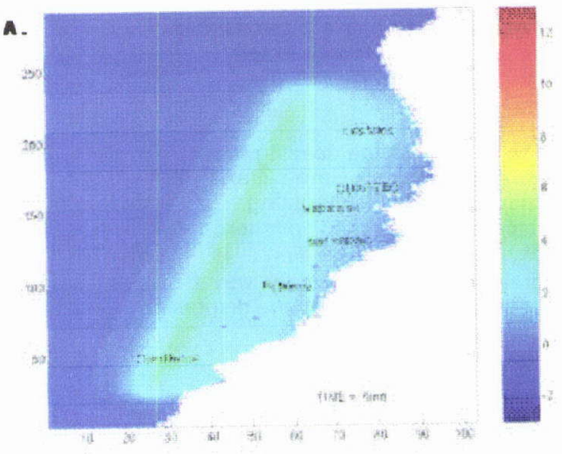
The generation and offshore propagation of the wave front in deep waters was calculated during a 3 h period with a time increment of 1 s. For the sake of brevity, results are depicted in Grid A every 5 min during the first 55 min of computation, time in which the wave front is sharply defined. Descriptive notes are attached to the figures, giving a brief explanation of the phenomena at each time interval.

Propagation followed a similar pattern with regards to the position in time and space of the wave front in all the cases in analysis for the 1730 tsunami. It was therefore decided to present model 1730-10 as representative of the phenomena[4]. 2-dimensional diagrams of the vertical displacement of the water surface in Grid A are depicted in figures 4.8 through 4.19.

A graphic aided 2-dimensional animation for Grid A was produced in Matlab 5.3 with a 1-min time increment during 75 min and is included in the CD-Rom (file:Tunamis/Tunami-N/1730-11/Aanimacion.m).

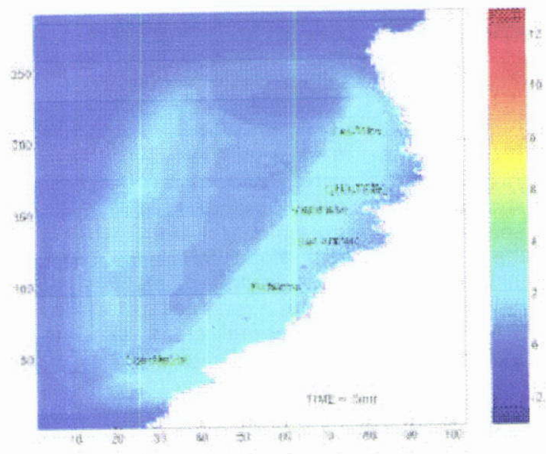
[4] *For time benefit, the set of diagrams for the 1906 and 1985 simulations are included only in digital version in D:\Tunami\Models\1906-1 and D:\Tunami\Models\1906-1, respectively.*

FIGURE 4.8 TIME HISTORY IN GRID A.
Time =0 min
Surface elevation in m.



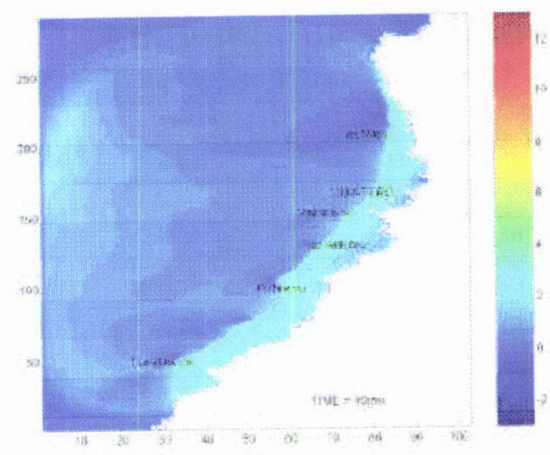
The initial wave profile resembles the actual crustal deformation, defined by the Mansinha and Smylie method, with a maximum wave height of about 3.5 m above MSL. The rupture is oriented almost parallel to the coast in the N°10E strike angle (the image is distorted), as expected from the seismotectonic features of the region.

FIGURE 4.9 TIME HISTORY IN GRID A.
Time =5 min
Surface elevation in m.



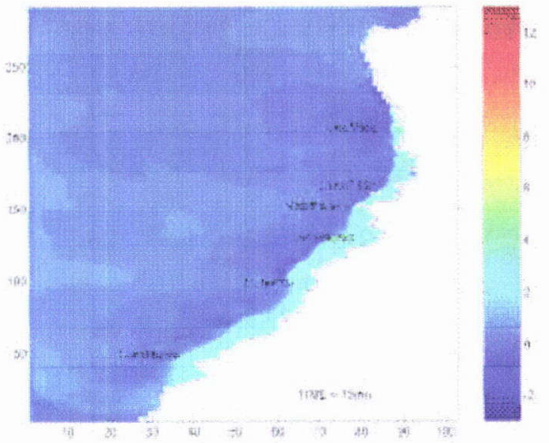
Two primary wavefronts are evident: one moving seaward with a celerity of approximately 600kph, and the leading wavefront propagating coastward with decreasing celerity as it enters shallow waters. Two secondary waves propagate to the Northwest and South, which gradually refracts towards the coast.

FIGURE 4.10 TIME HISTORY IN GRID A.
Time =10 min
Surface elevation in m.



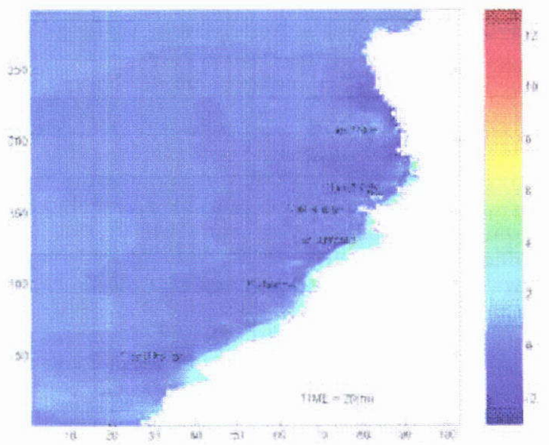
A large refraction pattern occurs as the wavefront approaches the coast. The leading wave initially travels perpendicular to the principal rupture axis but gradually refracts towards the shore. Secondary wavefronts initially travel parallel to shoreline and become clearly deflected at this stage.

FIGURE 4.11 TIME HISTORY IN GRID A.
Time = 15 min
Surface elevation in m.



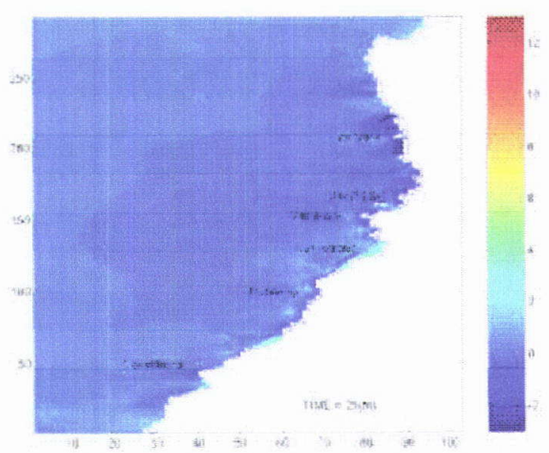
The height of the leading wave increases as approaching the coast while the seaward propagating wavefront becomes dispersed offshore. The extent of shoreline flooding is somewhat greater than the primary wavefronts as a consequence of the dispersion and refraction effects.

FIGURE 4.12 TIME HISTORY IN GRID A.
Time = 20 min
Surface elevation in m.



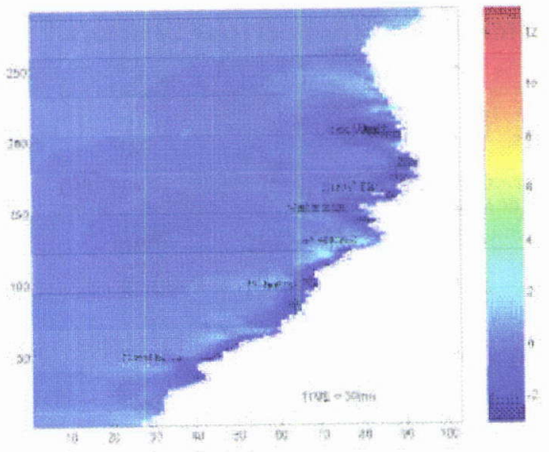
The leading wave reaches Quintero, increasing the water level to about 3 m above MSL in the entrance of the bay. Small-scale topographic features distort the uniform pattern along the coast. The initiation of the first trough is manifested in Los Vilos while the first peak is still in progress in the southern cities of San Antonio, Pichilemu and Constitución.

FIGURE 4.13 TIME HISTORY IN GRID A.
Time = 25 min
Surface elevation in m.



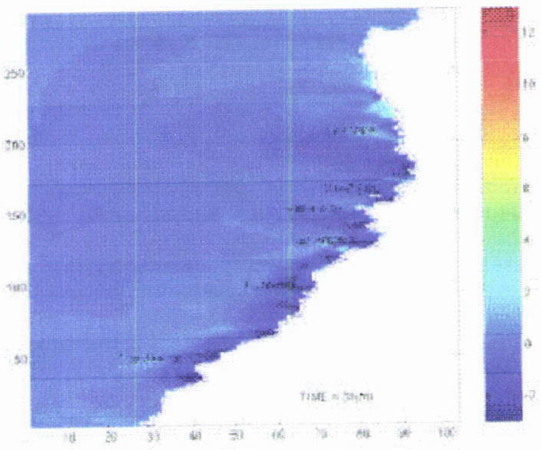
After maximum peaks of 4 m above MSL, a rapid downfall of the water level is experienced in the vicinity of Quintero bay. To the North, the water level drastically decreases 2 m below MSL. Southern areas experience the withdrawal of the first wave.

FIGURE 4.14 TIME HISTORY IN GRID A.
Time = 30 min
Surface elevation in m.



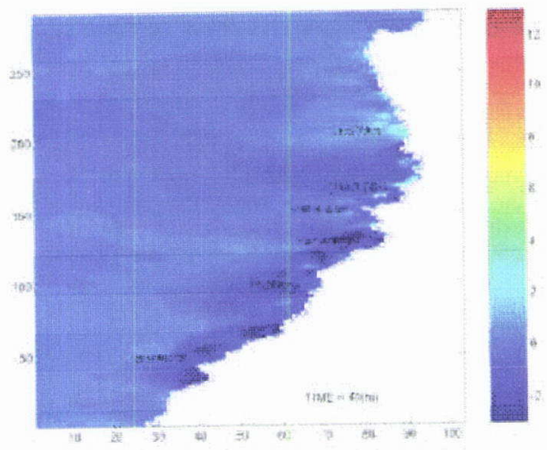
The first trough begins to affect Quintero with minimum height of 2m below MSL and is already in progress in the majority of the southern cities.

FIGURE 4.15 TIME HISTORY IN GRID A.
Time = 35 min
Surface elevation in m.



The downfall of the water surface keeps progressing in the central and southern cities whereas Los Vilos and northern areas become affected by the second wave.

FIGURE 4.16 TIME HISTORY IN GRID A.
Time = 40 min
Surface elevation in m.



The first trough reaches the minimum elevations of 3m below MSL in the entrance of Quintero bay. The second peak reaches Los Vilos. Multiple reflections along the coast result in a complex waterfront pattern.

FIGURE 4.17 TIME HISTORY IN GRID A.
Time = 45 min
Surface elevation in m.

Small-scale topographic features become a source of high frequency secondary oscillations in coastal areas which are gradually attenuated offshore.

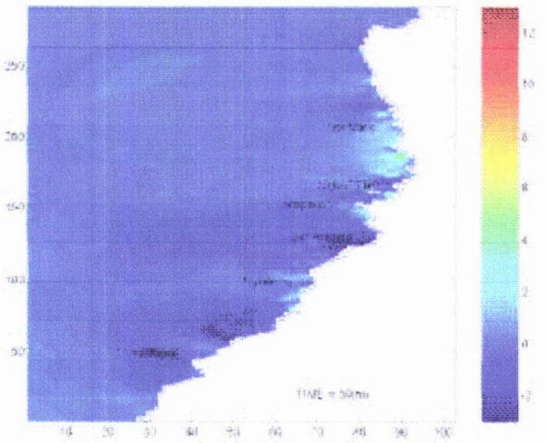


FIGURE 4.18 TIME HISTORY IN GRID A.
Time = 50 min
Surface elevation in m.

The effect of the second tsunami wave accompanied by short period secondary undulations begin to rise water levels in the vicinity of Quintero bay. Southern areas are still affected by negative levels whereas positive levels attack Los Vilos southern area.

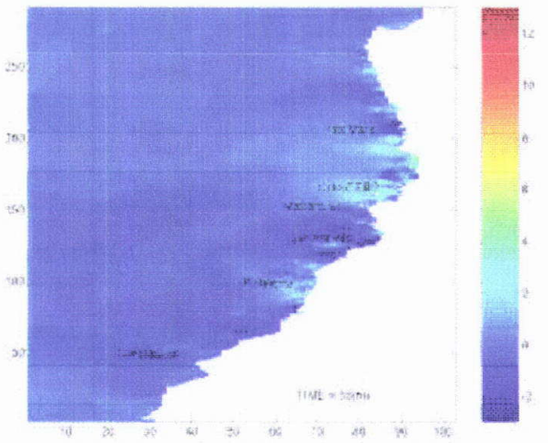
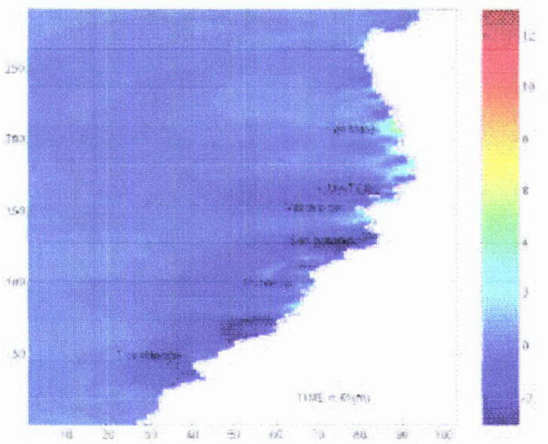


FIGURE 4.19 TIME HISTORY IN GRID A.
Time = 55 min
Surface elevation in m.

The second peak attacks Quintero with maximum amplitude of 4m above MSL in the entrance of the bay. The maximum trough affects San Antonio. A general pattern of the wavefront along the coast is vanished because of the local topographic effects and reflections along the coast.



4.3.2 GRID D

4.3.2.1 HEIGHT DISTRIBUTION ALONG THE COAST

Hypothetical stations were used to evaluate the space distribution of wave elevations within the bay. Station S1 (5.98) was selected to show wave progression in the entrance of the bay -approximately 100 m below MSL- while Stations S2 (40.30), S3 (65.35) and S4 (75.70) allow observing the amplitude along the coastline (Figure 4.20). Marigrams presented in Figure 4.21 show the water level throughout the computation for case 1730-10 (marigrams are depicted with 1min resolution during 3 h).

It is observed from Figure 4.21, that the leading wave resembles the actual bed deformation, showing an initial positive elevation of about 1.2m above MSL that coincides with the initial rise of the ocean bottom calculated in Section 3.4.4.

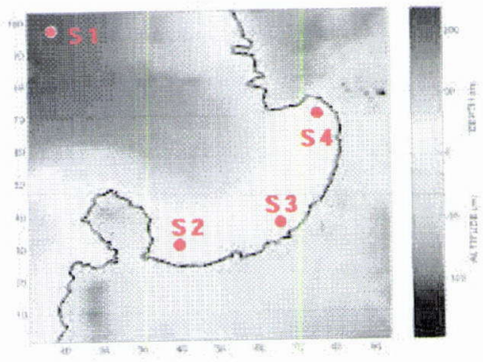


FIGURE 4.20 LOCATION OF THE MARIGRAMS

The estimated arrival time in the coastline is recorded with the first peak approximately 18 min after the occurrence of the earthquake. This result shows an excellent agreement with the estimations by Monge (1975), who predicted that a tsunami with similar characteristics (location and orientation of the rupture zone) would take between 18 to 20 min to reach the coast of Valparaíso. Similarly, Pilasi (1978) estimated an arrival time of 14 to 19 min for a tsunami generated offshore Quintero, using refraction analysis. This indicates an average celerity of about 330 km/h (calculated considering the distance of 110 km between the principal axis of the rupture zone and the coast.

Run-up is clearly observed through a considerable growth of tsunami elevations as the waves advances from the entrance (5,98) of the bay to the station located in the coastline. Waves ranging from 2 m to 4 m offshore are amplified to about 5m to 8m as approaching the coast. This amplification becomes significant with the arrival of the leading wave, approximately 25 min after the shock and becomes negligible 145 min after the shock.

Important peaks are registered 18, 46, 100 and 132 min after the shock -with maximum elevations ranging from 6 m to 8 m above MSL- whereas the major troughs are sharply defined 28, 76 and 120 min after the beginning of the simulation, with maximum values of 7m below MSL. An important attenuation is observed in the last 30 min, where short-period low-amplitude oscillations remain trapped in the bay.

Coastal stations (S2, S3 and S4) followed a similar pattern with regards to the temporal occurrence of the wavefront and showed only slight differences related more to the peak enhancement rather than the vertical displacement of the water surface, suggesting a regular profile along the coastline.

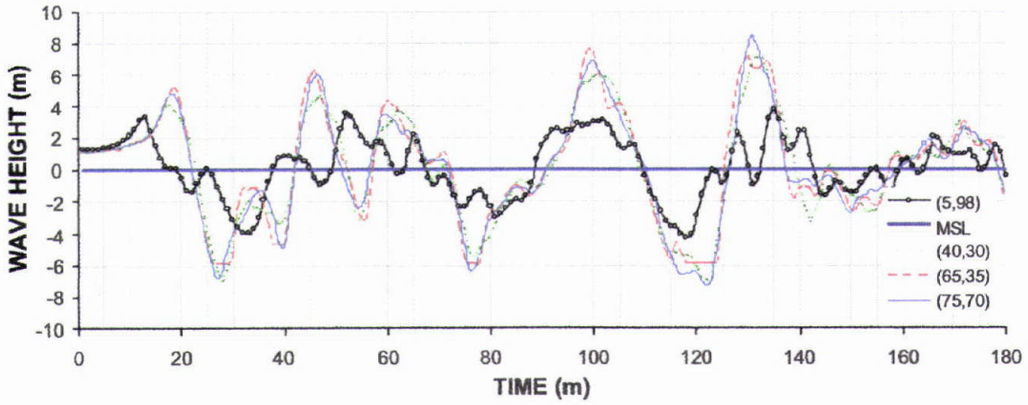


FIGURE 4.21 HYPOTHETICAL MARIGRAMS ALONG QUINTERO BAY.

4.3.2.2 RELEVANT ASPECTS IN TIME HISTORY FOR THE 1730 EVENT

A set of 2-dimensional diagrams showing an aerial view of the relevant features of the tsunami evolution in Grid D (i.e. the occurrence of peaks, troughs, and significant velocities) is depicted through Figures 4.22 to 4.36. The detailed sequence of wave elevations above MSL and velocity vectors (computed as $\vec{V} = M\hat{i} + N\hat{j}$) with a time step of 5 min is presented in Appendix 7 [5].

---

[5] *It should be said that the diagrams 4.22 to 4.33 represent the effect of a potentially destructive tsunami according to the classification given by Talandier (1993; cited by SHOA, 1999) and is not intended to characterise minor tsunamis.*

FIGURE 4.22 VELOCITY FIELDS
Time=0 min
Values in m/s

At the moment of the earthquake, a vertical uplift of the water surface is registered in the bay that is reflected in small currents coastward-oriented affecting the area.

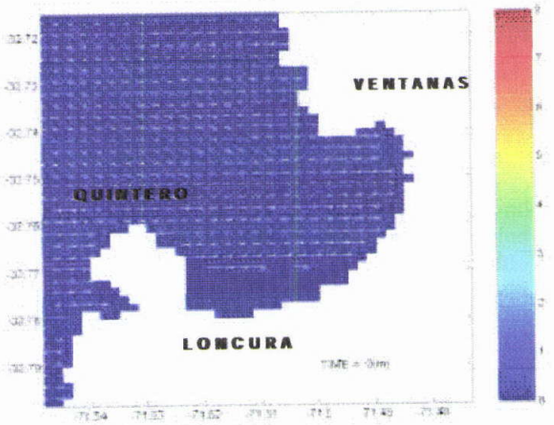


FIGURE 4.23 SURFACE ELEVATION!
Time= 20 min
Values in m

The leading wave arrives 18 min after the shock as a consequence of the initial bed deformation. Playa Loncura (see Figure 1.2) is moderately flooded by wave elevations of about 3 m above MSL.

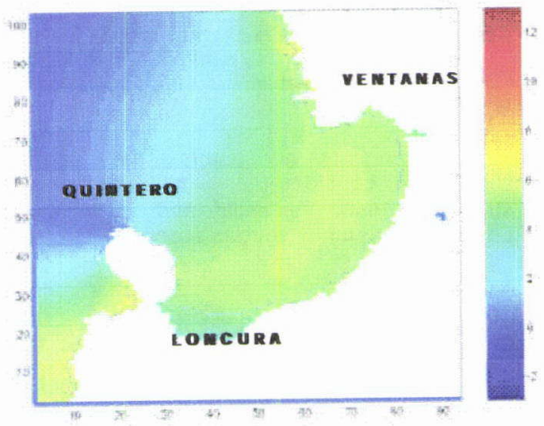


FIGURE 4.24VELOCITY FIELDS
Time=25 min
Values in m/s.

The coupled effects of refraction and diffraction become significant in the coastal boundary of Peninsula Los Molles. Velocity vectors adopt the shape of the coast, reaching up to 7 m/s in Punta Ventanilla.

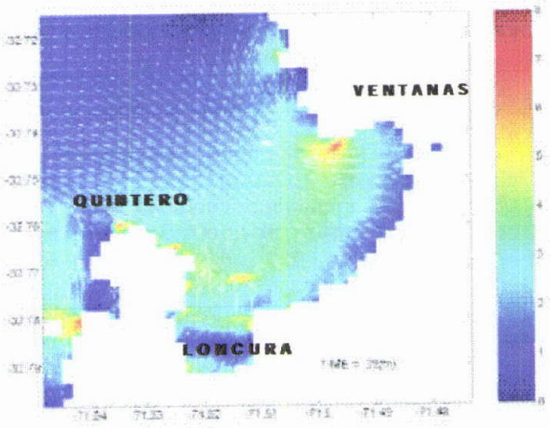
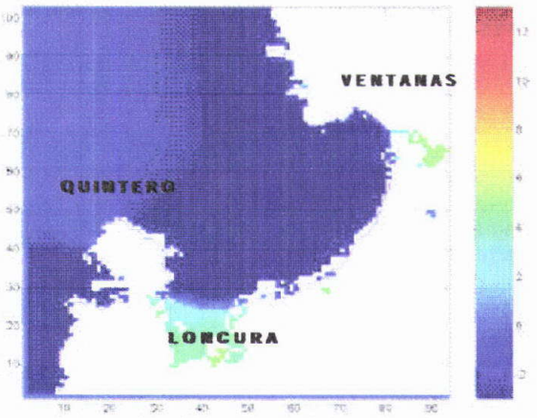
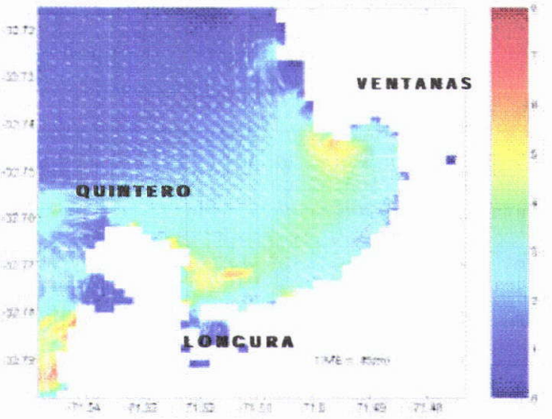


FIGURE 4.25 SURFACE ELEVATION
Time=40 min
Values in m



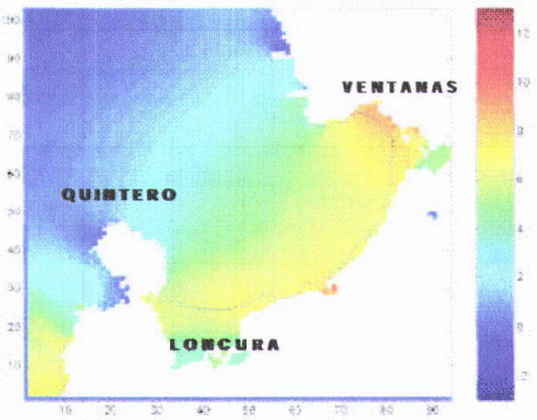
The first trough is recorded with a regular height distribution within the bay, approximately 38 min after the earthquake. A withdrawal of 200 m is observed in the relatively flat bottom of Playa de la Herradura.

FIGURE 4.26 VELOCITY FIELDS
Time =45 min
Values in m/s



The second wave enters the bay, showing considerable hydrodynamic stress in Punta Ventanilla and Península Los Molles. Velocity vectors reach 6m/s.

FIGURE 4.27 SURFACE ELEVATION
Time=50 min
Values in m



The second peak impacts the shoreline, flooding an extensive portion of Playa Loncura and impacting Ventanas with a considerable run-up of about 7 m above MSL.

FIGURE 4.28 VELOCITY FIELDS
Time=75 min
Values in m/s

The second wave begins to leave the bay with speeds of as much as 3 m/s.

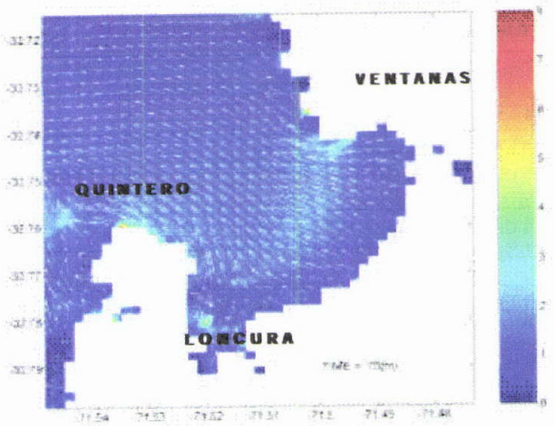


FIGURE 4.29 SURFACE ELVATIONS
Time=80 min
Values in m

Wavefronts are somewhat distorted as the second trough affects the bay. The withdrawal of the water level reaches almost 300m off the coastline in the northern portion of the bay.

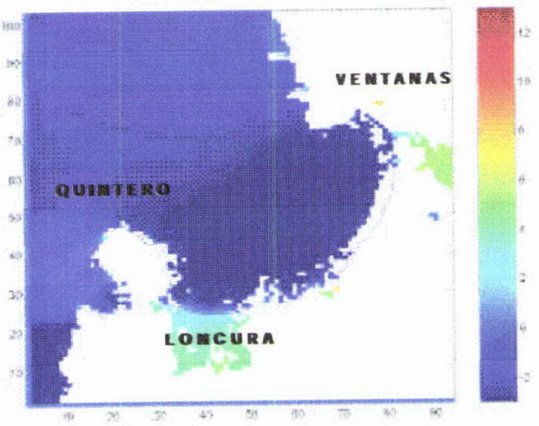


FIGURE 4.30 VELOCITY FIELDS
Time=100 min
Values in m/s

Velocity vectors are oriented coastward with moderate velocities as the third peak enters the bay.

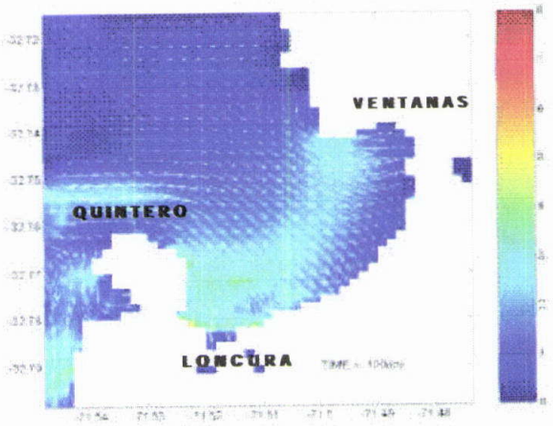


FIGURE 4.31 SURFACE ELEVATIONS
Time = 105min
Values in m

The third positive wave enters the bay 108 min after the shock (highest waves are not captured in this snapshot). Playa Loncura is attacked for the third time whereas Ventanas, and specially Estero Campiche are affected by wave elevations of 7 m above MSL.

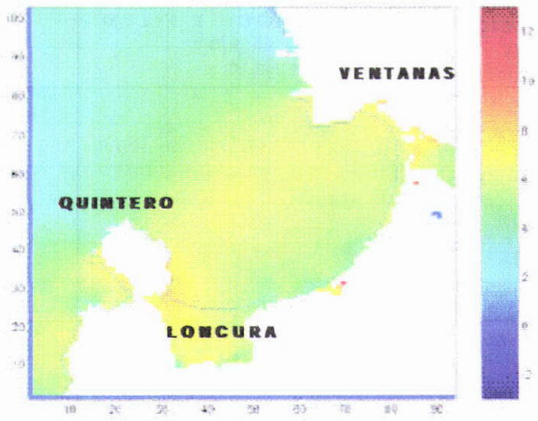


FIGURE 4.32 VELOCITY FIELDS
Time = 115 min
Values in m/s

Peninsula Los Molles is detected to be an important topographic feature in the definition of small-scale flow anomalies. Large-scale turbulent patterns are observed in front of Playa Loncura, with maximum speeds of 6 m/s.

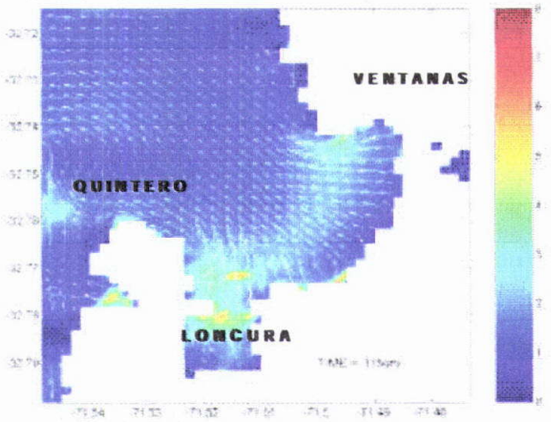


FIGURE 4.33 SURFACE ELEVATIONS
Time = 125 min
Values in m

The third trough generates a considerable withdrawal of about 250 m in the flat bottom areas of Playa de la Herradura. The signal becomes distorted in the last stage of the simulation.

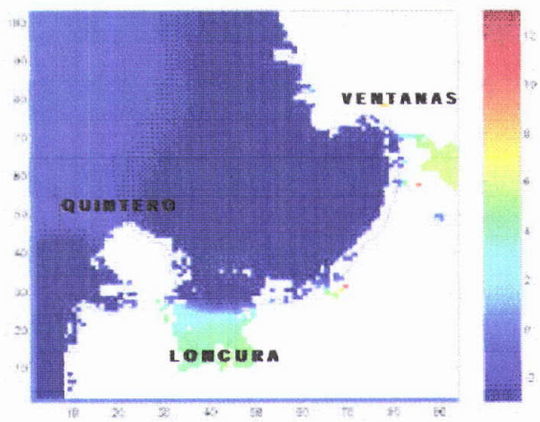


FIGURE 4.34 VELOCITY FIELDS
Time = 130min
Values in m

Deformation of the wavefront due to small scale topographic features are observed, showing a series of low amplitude oscillations and eddies where velocity reaches up to 6m/s.

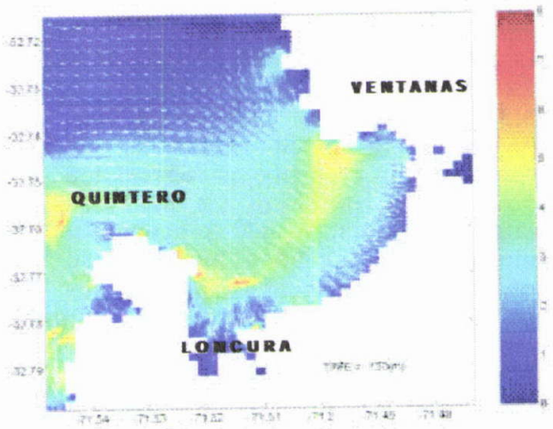


FIGURE 4.35 SURFACE ELEVATIOI
Time = 135min
Values in m

The fourth peak enters the bay approximately 135 min after the shock, showing the highest elevations of about 9m above MSL in Ventanas. Playa Loncura is drastically flooded inland with significantly lesser elevations of 5m above MSL.

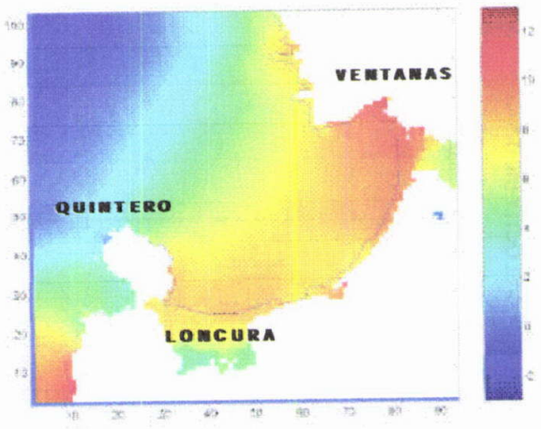
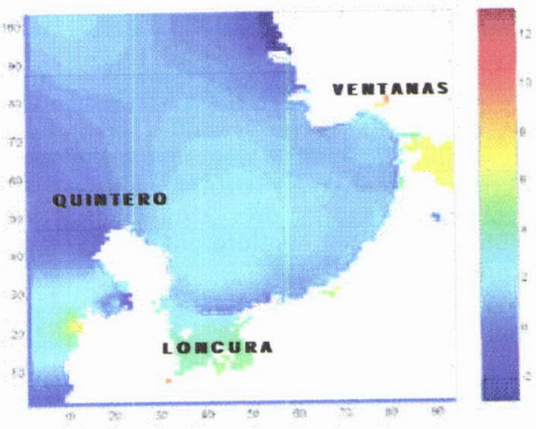


FIGURE 4.36VELOCITY FIELDS
Time = 140min
Values in m/s.

The signal to noise ratio becomes weak, mainly because the low amplitude oscillations of 5-10 min period. Subsequent diagrams are vague at this scale.



4.3.2.3 TSUNAMI WAVE ELEVATIONS V/S MAGNITUDE OF VELOCITY VECTORS

Grid point (40,30) was chosen to analyse the correlation between wave elevations and velocities[6]. Results are shown in Figure 4.37. In the first 25 min, an increasing velocity is associated with the arrival of the leading wave, showing a maximum of 5.4 m/s as the wave begins to retrieve. A low-speed plateau of about 5 min precedes the attack of the second wave, which is subsequently proceeded by about 50 min where there is no clear correlation between elevations and speed. This behaviour is manifested in small-period oscillations caused by diffraction, refraction and reflection in the surrounding area of Peninsula Los Molles. The maximum height of the third wave, approximately 100 min after the shock, is escorted by negligible speeds, followed by a rapid increment up to 6m/s as the wave leaves the bay. Important speeds, ranging from 4 m/s to 8 m/s are thereafter recorded for about 35 min, coinciding with the maximum and minimum elevations during the simulation.

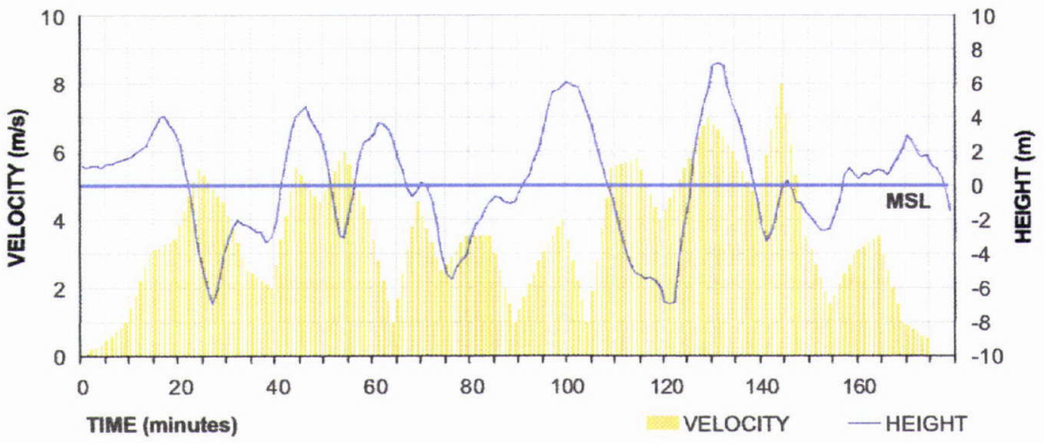


FIGURE 4.37.- WAVE HEIGHT V/S VELOCITY IN GRID D (40,30).

It should be noted that the resolution of the velocity record (5 min) is not enough to establish a robust correlation with wave elevations (1 min). Besides, it is accepted that TUNAMI model is accurate as far as tsunami elevations are concerned but shows significant deviations with regards to wave velocities (Shuto, 1991). Therefore, future efforts should be oriented to the study of this topic.

---

[6] *Since velocity represents the first temporal derivative of the particle position, wave velocities are expected to be delayed with respect to wave heights in T/4, so form a purely analytic approach, maximum heights should be associated to low speeds and vice-versa.*

4.3.2.4 3-D ANIMATION OF THE 1730 TSUNAMI

A 3-dimensional animation was produced with 1 min increment for a time period of 90 min. It is included in the attached CD-ROM and requires Matlab 5.3 to be executed (file:Tunamis/Tunami-N/1730-11/Danimacion.m). As an example three snapshots of the animation are shown as follows.

Figure 4.38 represents the beginning of the simulation, viewed from an aerial Northwestern location, where the undisturbed water surface is represented.

FIGURE 4.38.- 3D VIEW OF 1730 TSUNAMI IN QUINTERO BAY.
Case 1730-10. Time=0 min. Initiation of the rupture zone.

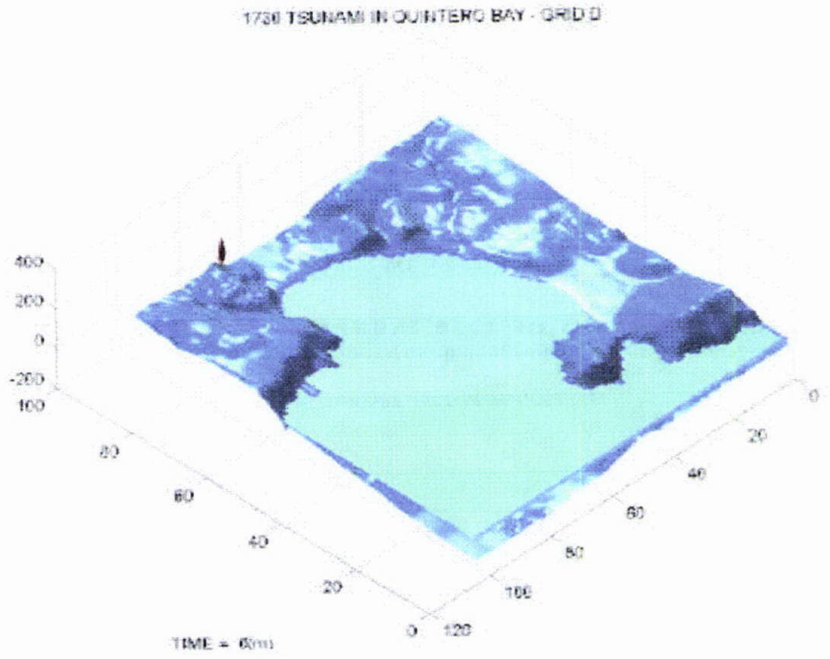


Figure 4.39 shows the instant immediately before the leading wave impacts the coastline, at the instant when Playa Loncura begins to be flooded. Figure 4.40 illustrates the maximum withdrawal approximately 30 min after the shock.

FIGURE 4.39.- 3D VIEW OF 1730 TSUNAMI IN QUINTERO BAY.
Case 1730-10. Time=20 min. Arrival of the first peak.

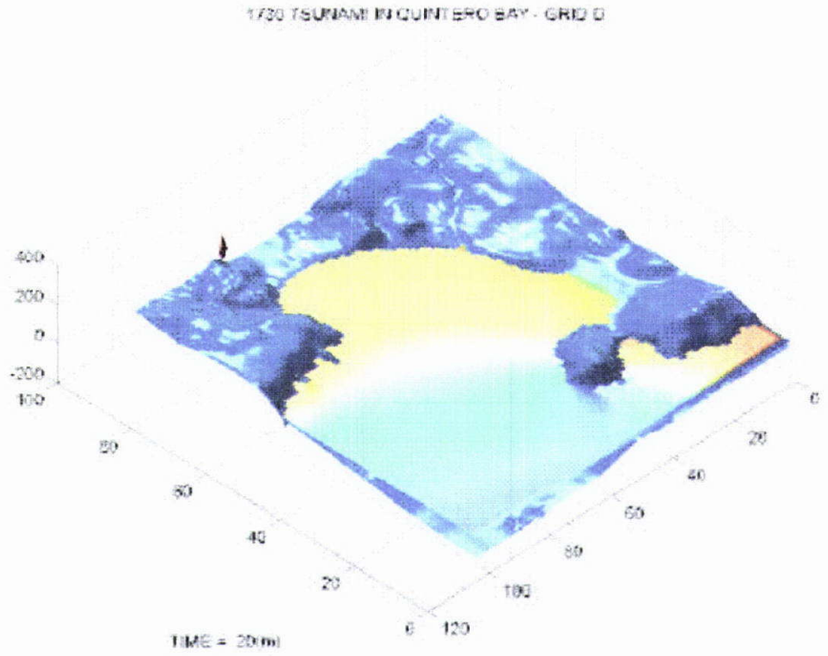
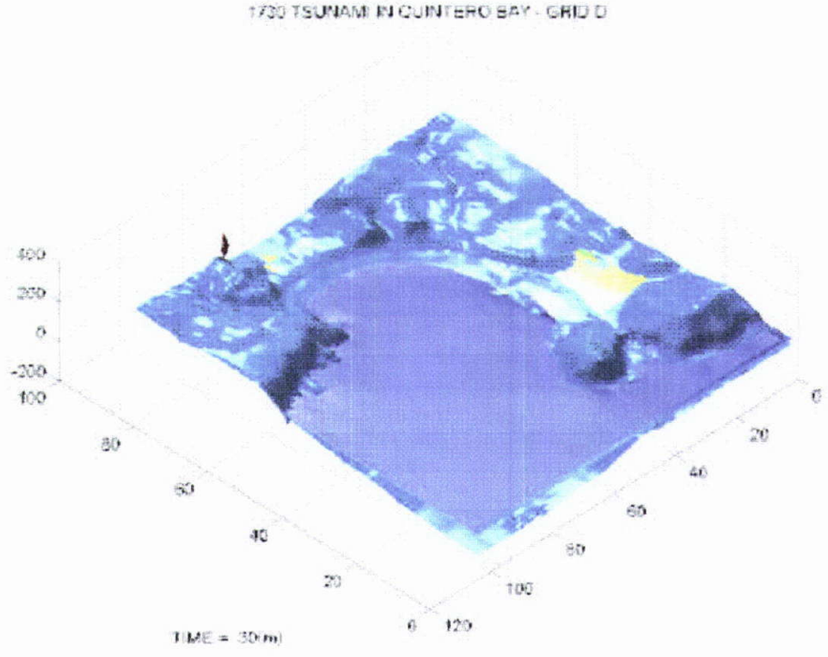


FIGURE 4.40.- 3D VIEW OF 1730 TSUNAMI IN QUINTERO BAY.
Case 1730-10. Time=30 min. Arrival of the first trough.



4.4 MAXIMUM ELEVATIONS AND VELOCITY

A summary of the maximum elevations and speeds computed in Grid D is shown in this section. Results are given in detail for the coastal stations S2, S3 and S4 in Tables 4.3 to 4.5 whereas the maximum flooding lines for the 1730, 1906 and 1985 tsunamis are depicted is Figures 4.41 to 4.43. A site-specific set of recommendations is proposed for the purpose of disaster preparedness and future planning for the area. Tsunami risk is evaluated as a function of the nature of the tsunami hazards (i.e. wave elevations, velocities and extend of the flooding), the vulnerability of coastal structures and the local community to damage, and the amount of development and people to the hazard. Risk is qualitatively evaluated considers land use, building types and occupancy, but exclude the possible tsunami effects on individual buildings.

Station S2 is intended to represent the small town of Ventanas, Estero Puchuncavi, the thermoelectric station, the copper refinery and the coastal installations of Terminales Quimicos Oxiquim S.A. and Puerto Ventanas S.A., the latter described in Appendix 8. It is clear from Table 4.3, that the 1730 event generates important wave elevations of 7 m above MSL and speeds up to 8 m/s, considerably greater than those of 1906 and 1985 tsunamis, cases that show wave elevations and currents speeds of the order of normal wind-type generated waves. The rapid drawdown of tsunami waves creates strong currents that can severely damage due to erosive scour around piers and pilings.

CASE	HEIGHT (m)	SPEED (m/s)	M_o (Nm)
1730-10	7.1	8.0	1.7×10^{22}
1906	2.1	1.2	5.6×10^{21}
1985	1.3	0.7	2.0×10^{21}

TABLE 4.3.- MAXIMUM HEIGH AND SPEED IN STATION S2, GRID POINT (40,30).

The industrial area of Ventanas is subject to a higher risk than residential and commercial zones of the town. A low level of risk should be mandatory for fire or hazardous material stored in the thermoelectric station while higher levels should be acceptable for areas with low replacement value.

Storage tanks in the surroundings of the power station are located in relatively risky area, where hydrodynamic forces associated to a potentially destructive event[7] could eventually cause ground failure or structural damage. Electrical vaults are not protected from wave and debris impact and would also be affected by the flooding. Since fire hazard is dependent on the ignition sources and the availability of fuel reservoirs, it is recommended to locate such facilities above flooding levels or to provide soil stability, protect with walls and anchor the tanks in order to avoid explosions and/or leaching of toxic chemical and hazardous substances to the environment.

It is clear that the industrial block of the power station would be severely affected by a potentially destructive event unless effective mitigating measures are implemented. Installations of Terminales Químicos Oxiquim S.A. are in a relatively safe position but could eventually be affected by secondary effects such as the ground erosion in the storage area. It is thus recommended also to undertake minor mitigating measures such as the provision of a stable revetment to guarantee the stability of the platform area under tsunami attack.

Large vessels are continuously berthed or waiting for bulk cargo transfer procedures in Puerto Ventanas and Terminales Químicos Oxiquim. Tsunami attack may produce the collision between berthed vessels and the port structure, impact with the bottom harbour or collapse of their mooring lines, issue which would require a specialised study which for the sake of brevity is not included in this report.

Station S3 is used to assess the risk in the coastal communities of El Bato and Playa de la Herradura. Model results are relatively similar to those found in S2 with respect to tsunami elevations but are significantly lower in the wave speeds. In consequence, pressure forces are comparable to those experimented in S2 while drag forces are significantly minor.

CASE	HEIGHT (m)	SPEED (m/s)	M_o (Nm)
1730-10	7.7	4.5	1.7 E+22
1906	2.3	0.8	5.6 E+21
1985	1.8	0.6	2.0 E+21

TABLE 4.4.- MAXIMUM HEIGH AND SPEED IN STATION S3, GRID POINT (65,35).

[7] *For comparative purposes, potentially destructive tsunamis will be referred as those with* $5x10^{21}Nm<M_o<2x10^{22}Nm$ *whereas minor tsunamis will be in the range* $10^{21}Nm<M_o<5x10^{21}Nm$, *as defined by Talandier (Table 2.2)*

The type of light constructions found in the coastal zone is expected to collapse under a great event but would remain with little damage in moderate episodes. Providing frictional characteristics to the coastline by landscaping with tsunami forests, building ditches, slopes and berms would be economic and sustainable alternatives to mitigate flooding and debris impact risks.

Station S4 is located immediately seaward from Playa Loncura. The military airfield is located in a highly vulnerable area, expected to experience up to 8.4m and speeds over 7.5 m/s (Table 4.5). These results are analogous to those found in S2 with respect both to tsunami elevations and speeds. It is observed that the flow is complex in this area, showing important variations in velocity vectors during wave attack.

CASE	HEIGHT (m)	SPEED (m/s)	M_o (Nm)
1730-10	8.4	7.8	1.7 E+22
1906	2.4	1.1	5.6 E+21
1985	1.6	0.7	2.0 E+21

TABLE 4.5.- MAXIMUM HEIGH AND SPEED IN GRID POINT (75,70).

The flooding extension in the military district could reach up to 1 km inland during a large event. Fortunately, this area is inhabited and the existing structures represent low replacement value. Landscaping with a dense barrier of tsunami forests in the upper bound of Playa Loncura would be efficient to mitigate flooding risks. Some areas in downtown Quintero (located in the Eastern section of Peninsula Los Molles) are partially flooded without producing major problems over coastal infrastructure.

Unanchored small crafts could become a source of debris if dragged inland by the currents. Boats may be destroyed again coastal defences or washed ashore and left grounded after the withdrawal of the seawater, with the resulting effects on local fishing industry. The Western coastline of Quintero is formed by steep cliffs, which become a natural protection to the high lands of the peninsula.

The maximum flooding lines for the 1730, 1906 and 1985 tsunamis are depicted in Figures 4.41 to 4.43:

FIGURE 4.41 FLOODING LINE 1730 (CASE 1730-10)

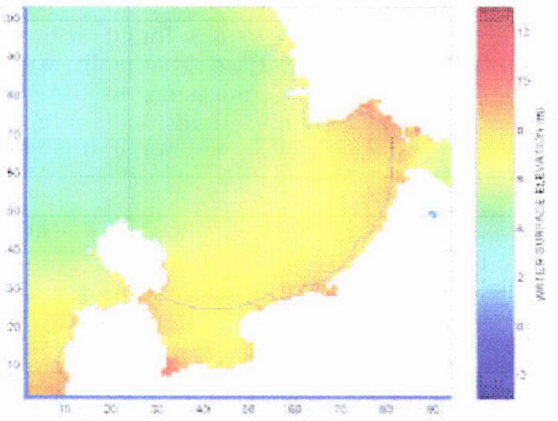


FIGURE 4.42 FLOODING LINE 1906 (CASE 1906-1)

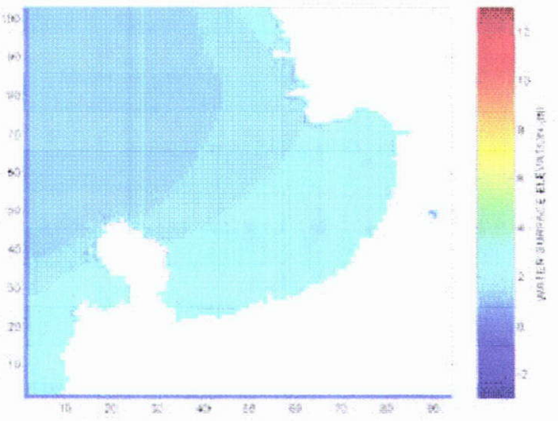
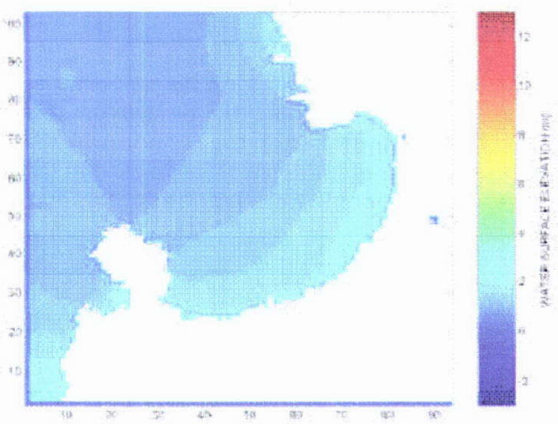


FIGURE 4.43FLOODING LINE 1985 (CASE 1985-1)



The computational boundaries of the flooding line obtained in Figures 4.41 to 4.43 were overlapped in the actual topographic map using AutoCad facilities (Figure 4.44).

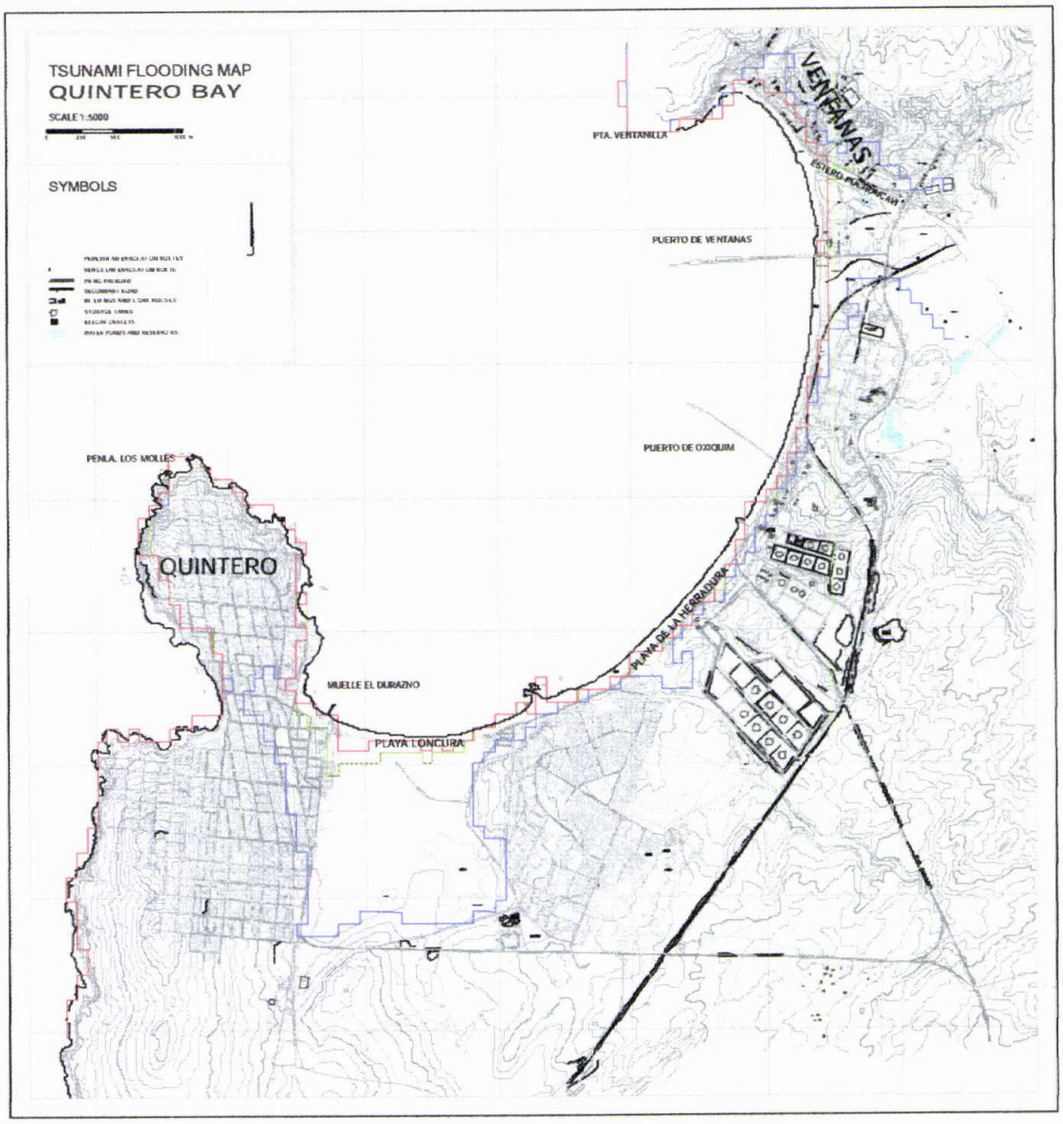


FIGURE 4.44.- FLOODING LINES FOR THE 1730, 1906 AND 1985 TSUNAMIS.

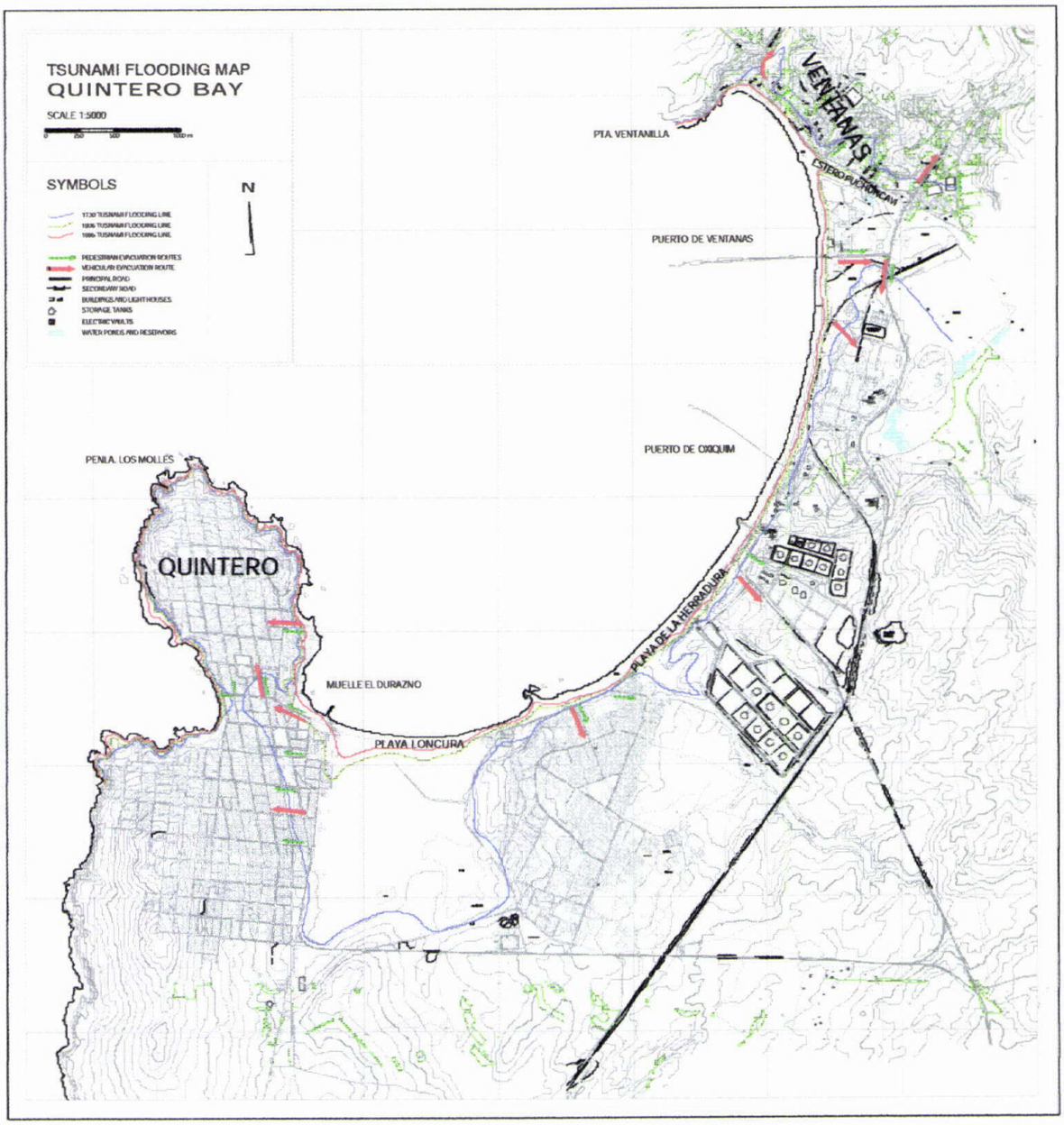
To facilitate the production of the tsunami flooding chart, a smooth line was interpolated between grid results according to the small-scale topographic features not described in the 92 x 92m grid.

4.5 TSUNAMI FLOODING MAP

The flooding map (Figure 4.45) represents the maximum run-up along the coastline for the 1730, 1906 and 1985 events, described in terms of their respective seismic moments. The map was plotted with a scale 1:5.000 and is attached in Appendix 11. The aim of the chart is to warn the local community and specially the authorities of Quintero of the risk posed to the population inhabiting the area. It designates zones along the coast of the bay with varying degrees of tsunami risk for the purpose of public preparedness, planning, building regulations and public evacuation.

The map is intended to provide and easy vehicular and pedestrian evacuation and to guarantee post disaster access to the site. The map shows the routes, which people must use to avoid tsunami waves and safety areas to receive evacuees. These routes will be informed to local authorities that should design a communication plan based in this study and provide with educational material for the community. The police entities should be responsible of the execution of evacuation plan by providing traffic controllers and transportation facilities at critical points of the bay.

FIGURE 4.45.- TSUMANI FLOODING MAP FOR THE 1730, 1906 AND 1985 TSUNAMIS.



CHAPTER 5
CONCLUSIONS

5.1 GENERAL COMMENTS

The increasing development pressures for the use of the coastal zone of Quintero bay prompted the assessment of tsunami risk in the area with the aim of advising upon the possible consequences of a tsunami attack and providing guidelines for mitigation measures to be adopted in the near future. Although the objective of tsunami risk analysis is to provide reliable statistical statements of the occurrence probability of a particular event at a given site during a given interval of time, this is yet not possible due to the scarcity of high quality field measurements in Quintero and because seismic characteristic of Central Chile are not sufficiently characterised.

Based on this fact, the contribution of this work is to include a range of possible scenarios for historical earthquakes in Central Chile (1730, 1906 and 1985 events), rather than providing a statistical approach or using no more than two historical events in the generation of flooding charts, as done until now in the CITSU project.

For the proposed objectives, the current state-of-the-art of numerical simulations represent the best available technology to provide tsunami risk forecast in Quintero. Regardless of the results herein presented, it should be stated that tsunami modelling still requires further research.

5.2 SEISMOLOGIC ASPECTS

Until improved information about seismologic features in Central Chile becomes available to characterise the initial bed deformation, it appears desirable to use the Mansinha and Smylie method (1971). It should be recognised however, that as this estimate is performed in a rather schematic way, resulting wavefronts resemble the input characteristics that could not strictly represent a particular real case.

With regards to the sensitivity of the simulation to the input parameters of the Mansinha and Smylie method, run-up and velocity fields are highly dependent on the strike angle, mean dislocation and length of the rupture zone, whereas less sensitive to variations in the dip angle, dislocation angle and to the rupture width. The effect of the depth of the epicentre is not clearly characterised with this method and should be reviewed in the future.

A challenge on the subject is to obtain a reliable description of the seabed deformation through highly developed analysis of seismic records in Central Chile or by means of the comparison between pre and post earthquake bathymetry in the rupture zone. Unfortunately, this is not yet possible due to technical and economic limitations.

5.3 TUNAMI-N MODEL

TUNAMI-N code in combination with Matlab 5.3 graphical facilities show an efficient performance concerning run times and memory consumption but requires excessive time in the preliminary digitising procedure. The latter could be optimised whether by unifying the available bathymetric records under a single database to be managed by SHOA or by improving the specialised software and computational facilities used in this stage. Digitation software should be capable to allow user-specified grid rotations to match the estimated rupture zone thus avoiding numerical disturbances in the simulation. With regards to the stability and convergence, the algorithm shows outstanding results since the time and space increments adopted in the simulation fulfil Courant's condition in 3-h simulation.

TUNAMI-N does not incorporate tidal and other hydrometeorological factors considered reasonable in Quintero. Therefore, worse scenarios than those herein presented could arise on tsunami attack during high tide, estimated as 76 cm above MSL in Quintero, whereas tsunamis occurring during low tide would eventually be less damaging for the area. Similarly, a tsunami happening in coincidence with wave storms is expected to be more significant than during a relative calm. Until more sophisticated methods are available in Chile, the combination of supplementary effects is not possible.

The effect of buildings and small-scale topographic features (not considered in the 92x92 m grid's resolution for Quintero bay) could be considered by incorporating a higher Manning's coefficient. As guidelines, Shuto (1991) suggested values of $n=1$ for Japanese harbours whereas Bretschneider and Wybro (1976) estimated the coefficient in $n=0.30\text{-}0.35$ for moderately developed areas with low density of buildings. However, until no field or experimental data is available, the adoption of specific values is an error source.
Alternatively, using building-scale grids based on a high-resolution topography could improve the definition of the flooded areas but would certainly introduce complex singular hydrodynamic effects. Nonetheless, this subject is not of main concern for the objectives herein proposed since long period waves are almost unaffected by small-scale topographic features and buildings.

Further research should be encouraged in the application of transoceanic models to Chilean ports.

5.4 THE HYPOTHESIS

Considering the presented results, it was concluded that tsunami inundation areas are strongly dependent on the Seismic Moment (Mo) of the triggering earthquake and on the topo-bathymetric features of each particular portion of the bay. The hypothesis was found to be extremely general regarding the characterisation of the earthquakes (restricted to those *"large earthquakes of* $M_O > 5x10^{21}$ *Nm"*) and vague in the description of the type and extent of tsunami risk. In spite of this, some comments are derived from the analysis of the hypothesis:

It was established that the Northeastern area of Ventanas and the military area in Quintero would be severely affected by *potentially destructive tsunamis*[1], with flooding areas affecting the local community and coastal installations. Maximum tsunami run-up would reach up to 8 m and velocities of 8 m/s would be experienced in particular areas within the bay. In contrast, *minor tsunamis* would imply negligible impacts in the coast, showing run-ups of 2 m and maximum velocities of 1 m/s. These results substantially differ from the previous assessment carried out by Pilasi (1978), who concluded that, by the end of year 1978, the area was not under tsunami risk. Since then, development pressures experienced in the coastal area of the bay have been enormous and land use has been dramatically modified, resulting in an increased tsunami risk.

5.5 TSUNAMI RISK IN QUINTERO BAY

The industrial area of Ventanas, including the thermoelectric power station and the installations of Puerto Ventanas, is exposed to a higher risk than residential and commercial zones because of the direct exposure to tsunami waves. Storage tanks in the thermoelectric station and copper refinery could be affected by ground failure or structural damage caused by a potentially destructive tsunami. Electrical vaults are not protected from wave and debris impact and could be dragged away by the flow. It is thus recommended to provide soil stability and tanks anchoring in order to avoid explosions and/or leaching of toxic substances to the environment.

Special consideration should be given to the protection and relocation, if necessary, of critical lifelines in the industrial zone (i.e. water systems, gas piping, sewers and the telephone service). Machinery and equipment in Terminales Oxiquim are in a relatively safe position and only minor mitigating measures, such as the provision a stable revetment to guarantee the stability of the platform, should be implemented.

---

[1] *This classification follows the definition given in Table 2.2.*

The type of light constructions found in the coastal zone is expected to collapse under a potentially destructive tsunami but would remain with no damage in minor episodes. Providing frictional characteristics to the coastline, by landscaping with tsunami forests or by building drainage nets, would be economic and sustainable alternatives to mitigate flooding risks.

The flooding extension in the military district would reach up to 1 km inland during a potentially destructive event. Fortunately, this area is quite inhabited and the existing structures are of low replacement value. Downtown Quintero is relatively protected for the direct tsunami attack because of the shadowing effect of Península Los Molles. Western Quintero is formed by steep cliffs, which become a natural protection to the communities settled in the high lands of Península Los Molles. Therefore, insignificant tsunami risk is therefore experienced in this area.

5.6 MITIGATION MEASURES

Even though the objective of tsunami inundation mapping is to provide guidance for forecasting and hazard assessment during a potential event, it also offers a good starting point for land use planning and for the definition of mitigation measures. Basically, there are two approaches to reduce tsunami risk which are ***a)*** the construction of engineered breakers intended to retard or block the volume of water or ***b)*** to propose risk management policies designed to control the risk through land use planning.

The first approach is intended to provide protection to the coastal structures with breakwaters, seawalls, dikes and revetments or by dredging in critical areas. Tsunami-based structural design implies massive structures, which are for sure economically not viable in Chile and therefore are not considered as a cost-effective mitigation measure for Quintero.

The second approach is thus recommended for the area based on the principle that possible effects of tsunamis can be mitigated with prevention, autoprotecction and prudent measures. A site-specific risk management plan should synthesise tsunami flooding risk herein evaluated, seismic considerations (such as ground failure, liquefaction and landslides), coastal erosion and fire hazards under an integrated land use proposal elaborated by specialists. The risk management plan should classify and delineate areas for building purposes according to the use, type and importance of structures and activities proposed, and put into operation through a geographic information system (GIS). It should restrict new development in tsunami run-up areas; protect existing areas through a re-development process and should take special precautions in locating infrastructure, critical facilities and lifelines.

Since the estimated time of arrival of a near-field tsunami to the coastal area of Quintero is estimated between 15 to 20 min, it is strongly recommended to prepare a communication plan with educational materials in order to encourage public awareness of the tsunami threat.

CHAPTER 6
REFERENCES

BOOKS

1 ABE, K. (1973). *Tsunami and mechanism of great earthquakes*. Phys. Earth, Planet. Inter.

2 AIRY, G. (1845). *On Tides and Waves*. Encyclopaedia Metropolitana.

3 ADAMS, W. (1974). *Tsunami anomalies and precursory phenomena having potential value of predictors*. Proc. 5th World. Conference Earthquake Engineering. 11: 2754-2762.

4 AKIMA, H. (1978). *A Method of Bivariate Interpolation and Smooth Surface Fitting for values given at Irregularly Distributed Points*. ACM-TOMS, vol. 4, no. 2,

5 AKIMA, H. (1984). *On Estimating Partial Derivatives for Bivariate Interpolation of Scattered Data*, Rocky Mountain Journal Of Mathematics, Vol. 14, no. 1.

6 BARRIENTOS, S. (1990). *Slip distribution of the 1985 Central Chile Earthquake*. Universidad de Chile. Santiago – Chile.

7 BRETSCHNEIDER, Ch. and WYBRO, P. (1976). *Tsunami Inundation Prediction*. Tsunami Hazard and Design of Coastal Structures. *Fifteenth Coastal Engineering Conference*. Washington D.C. – U.S.A.

8 CAMFIELD, F. ( ). *Tsunami*. Coastal Engineering Research Center (CERC). U.S. Army Engineer Waterways Experiment Station. Mississippi, U.S.A.

9 CAMPUSANO, A. (1984). *Nociones fundamentales sobre maremotos o tsunamis*. Instituto Hidrográfico de la Armada. Valparaíso – Chile.

10 CHISTENSEN, D. (1986). *Rupture process of the March 3, 1985 Chilean Earthquake*. Geophysical Research Letters. University of Michigan. Vol. 3. No. 8, pp 721-74.

11 COMTE et al. (1986). *The 1985 Central Chile Earthquake: A repeat of previous great earthquakes in the region*. Universidad de Chile. Santiago – Chile.

12 DEFANT, A. (1961). *Physical Oceanography*. Pergamon Press, Inc., New York, N.Y. 598 p.

13 DE LA CRUZ, J. (1997). *Estudio del riesgo de Tsunami en las ciudades costeras de la primera región*. Departamento de Ingeniería Civil, Facultad de Ciencias Físicas y Matemáticas, Universidad de Chile. Santiago – Chile.

14 DEPARTMENT OF THE ARMY ENGINEERING WATERWAYS EXPERIMENT STATION. (1984). *Shore Protection Manual, Vol. 1*. Mississippi, United States.

15 DEPARTMENT OF THE ARMY ENGINEERING WATERWAYS EXPERIMENT STATION. (1984). *Shore Protection Manual, Vol. 2*. Mississippi, United States.

16 DHI Water & Environment (2000). *MIKE 21. Coastal Hydraulics and Oceanography. Hydrodynamic Module. Reference Manual*. Denmark.

17 FARRERAS, S. (1995). *Tsunamis en México*. Monografía N°5 Unión Geofísica Mexicana.

18 GODOY, H. and MONGE, J. (1975). *Metodología para la evaluación del riesgo de Tsunami*. Publicación SES I 3-75. Facultad de Ciencias Físicas y Matematicas, Universidad de Chile. Santiago – Chile.

19 GUTEMBERG, B and RICHTER, F. (1941). *Seismicity of the Earth*. Geological Society of America.

20 HAMMACK, J. and RAICHLEN, F. (1972). *Tsunami generation and propagation. Thirteenth Coastal Engineering Conference*. Washington D.C.

21 HEALTH, R. and CRESSWELL, M. (1974). *Tsunami Research Symposium 1974*. Published jointly by The Royal Society of New Zealand, Wellington and The Unesco Press, Paris. ISBN 92-3-101330-0.

22 IIDA, K. (1956). *Earthquakes accompanied by tsunamis occurring under the sea off the islands of Japan*. J. Earth Sci., Nagoya University. 4: 1-43.

23 IIDA, K. (1970). *The generation of tsunamis and the focal mechanism of earthquakes*. pp. 3-18. *In* W.M. Adams (ed.) Tsunamis in the Pacific Ocea, East West Center Press, Honolulu, Hawaii.

24 IMAMURA F. and SHUTO, N. (1991). Analysis of the OBS Data and Numerical Simulation for the 1990 Mariana Earthquake Tsunami. in TINTI, S. (ed.). *Tsunamis in the World. Fifteenth International Tsunami Symposium, 1991*. Kluwer Academic Publishers. pp. 95-106.

25 INN-Chile (1996). *NCh 433.Of96. Earthquake Resistant Design of Buildings*. 1Ed. Instituto Nacional de Normalización, Chile.

26 INTERNATION TSUANMI INFORMATION CENTER (2001). *Tsunami Glossary.* Honolulu, Hawaii. U.S.A.

27 IOC (1998). *Post-Tsunami survey field guide. IOC Manuals and Guides No. 30.* First Edition. UNESCO 1998 (English).

28 IPPEN, A. (1966). *Estuary and Coastline Hydrodynamics.* McGraw-Hill Book Company Inc., United States of America.

29 IUGG/IOC (International Union of Geodesy and Geophysics).Time Project. *IOC Manuals and Guides No. 35.* UNESCO 1997 (English).

30 KAUSEL, E. (1986). Cap.2: Proceso Sísmico, Parámetros Focales y Réplicas del Sismo del 3 de Marzo de 1985. *El Sismo del 3 de Marzo de 1985 – Chile.* ACERO COMERCIAL S. A.. Santiago de Chile.

31 LIZANA, J. (2000). *Evaluación del efecto de Tsunami sobre edificios.* Departamento de Ingeniería Civil, Facultad de Ciencias Físicas y Matemáticas, Universidad de Chile. Santiago – Chile.

32 LOMNITZ, C. (1970). *Major Earthquakes and tsunamis in Chile during the period 1535 to 1955.* Geol. Rundschau. 59,3 938-960.

33 LORCA, E. (2001). Ex-Director of the Chilean Seismological Service. Personal conversation

34 MANSINHA, L and SMYLIE, D. (1971). *The displacement of the earthquake fault model.* Bull. Seismol. Soc. Amer. 61. pp. 1433-140077.

35 MONGE J. (1996). Aspectos Sismológicos. *in* BONELLI, P. (ed.). *Diseño sísmico de Edificios.* Universidad Técnica Federico Santa María, Chile. pp. 29-84.

36 MORANDE, A. and LAMAS, V. (1995). *Chile País Puerto.* Lamas y Cía. Ltda. ISBN 956-7055-08-4.

37 MURTY, T. (1977). *Seismic Sea Waves – Tsunamis.* Bulletin of the Fisheries Research Board of Canada. Ottawa. ISBN 0-660-00565-4.

38 MYERS, E.; BAPTISTA A. AND PRIEST, G., (1999). *Finite Element Modeling of Potential Cascadia Subduction Zone Tsunamis. Science of Tsunami Hazards,* **17**(1):3-18.

39 NEWMARK, N. and ROSENBLUETH, E. (1971). *Fundamentals of Earthquake Engineering.* Prentice-Hall. London.

40 OKAMOTO, S. (1973). *Introduction to Earthquake Engineering.* University of Tokio Press. Japan. ISBN 0 470-65307-8.

41 ORTIZ, M. (1996). *Manual de instrucción sobre la simulación numérica de un Tsunami. Proyecto Time.* Servicio Hidrográfico y Oceanográfico de la Armada de Chile.

42 PARARAS-CARAYANNIS, G. (1976). Tsunami Hazard and Design of Coastal Structures. *Fifteenth Coastal Engineering Conference.* Washington D.C.

43 PARDO, M.; COMTE, D. and EISEMBERG, A. (1989). Sismicidad histórica y evaluación del peligro sísmico en la zona central de Chile. in MINISTERIO DE VIVIENDA Y URBANISMO (eds.). *5AS Jornadas Chilenas de Sismología e Ingeniería Antisísmica.* Vol.1. Pontificia Universidad Católica de Chile. Santiago, Chile.

44 PICKERING, K and OWEN, L (1995). *An Introduction to Global Environmental Issues.* Rautledge, London. pp. 226–229. ISBN 0-415-10228-6.

45 PILASI, J (1978). *Riesgo de Tsunami en bahía de Quintero.* Departamento de Obras Civiles, Facultad de Ciencias Físicas y Matemáticas, Universidad de Chile. Santiago – Chile.

46 PONCE, L. Et al. (1985). *El terremoto de la zona Central de Chile.* CERESIS/UNESCO. Lima – Peru.

47 PRENAFETA, S. (1983). *Alerta vía satelite contra los tsunamis.* ACHIPEC. Chile.

48 PREUSS, J (1988). *"Planning for Risk: Comprehensive Planning for Tsunami Hazard Area. Urban Regional Research".* USA.

49 RICHTER, C. (1958). *Elementary Seismology.* W.H. Freeman. San Francisco California.

50 SARAGONI, R.; GONZÁLEZ, P. and FRESARD, M. (1986). Cap.3. Análisis de los Acelerogramas del Terremoto del 3 de Marzo de 1985. *El Sismo del 3 de Marzo de 1985 – Chile.* ACERO COMERCIAL S. A.. Santiago de Chile.

51 SECCATORE, I. (2000). *Modelación numérica en Diferencias Finitas de corrientes en lagunas de geometría irregular.* Universidad Técnica Federico Santa María, Chile.

52 SHOA (1994). *Atlas Oceanográfico para la Educación.* Valparaíso – Chile. ISBN 956-235-016-9.

53 SHOA (1997). *Atlas Hidrográfico de Chile.* Valparaíso – Chile. ISBN 956-235-018-5.

54 SHOA (1999). *Carta de Inundación por Tsunami para la Bahía de Valparaíso*. Valparaíso – Chile.

55 SHOA (2000). *Cómo sobrevivir a un maremoto. 11 lecciones del Tsunami ocurrido en el sur de Chile el 22 de Mayo de 1960*. Valparaíso – Chile.

56 SHOA (2000). *Instrucciones generales sobre el Sistema Nacional de Alarma de Maremotos, 4°Ed*. Valparaíso – Chile.

57 SHOA (2001). *Tablas de Marea de la Costa de Chile*. Valparaíso – Chile.

58 SHUTO, N. (1991). Numerical Simulation of Tsunamis – Its Present and Near Future. in BERNARD E. (ed.). *Tsunami Hazards. A Practical Guide for Tsunami Hazard Reduction*. Kluwer Academic Publishers. Pp. 171-192.

59 SORENSEN, R. (1978). *Basic Coastal Engineering*. John Wiley & Sons, Inc. United States. ISBN 0.471-81370-2.

60 STEETER, V. (1962). *Fluid mechanics*. New York. McGraw-Hill.

61 TAKAHASI, R. (1961). *Report on the Chilean tsunami of 1960*. Proc. 2nd World Conf. Earthquake Eng. pp. 639-647.

62 TITOV, V. and GONZALEZ, F (1997). *Implementation and testing of the method of splitting tsunami (MOST)*. NOAA Technical Memorandum ERL PMEL-112. Pacific Marine Environmental Laboratory.

63 TITOV, V. and SYNOLAKIS, C ( ). *Extreme inundation flows during the Hokkaido-Nansei-Oki Tsunami*.

64 TSUTSUMI, A. et al. (2000). *Nearshore Flow Velocity of Southwest Hokkaido Earthquake Tsunami*. Journal of Waterway, Port, Coastal and Ocean Engineering. May/Jun. 2000, Vol.126, No.3. American Society of Civil Engineers. ISSN 0733-950X.

65 TURISMO Y COMUNICACIONES S.A (1997). *Guía turística de Chile – TURISTEL*. Compañía de Telecomunicaciones de Chile S.A.. Santiago – Chile. ISBN 956-7264-33-3

66 UNIVERSIDAD CATOLICA DE VALPARAISO. FACULTAD DE RECURSOS NATURALES. INSTITUTO DE GEOGRAFIA (1996). *Atlas V Región Valparaíso*. Valparaíso, Chile.

67 VAN DORN, W. (1961). *Some characteristic of surface gravity waves in the sea produced by nuclear explosions*. J. Geophys. Res. 66: 3845-3862.

68 VAN DORN, W. (1968). *Tsunami*. Contemp. Phys. 9: 145-164.

69 VASQUEZ, J. (2001). Instituto Nacional de Hidráulica. Personal conversation.

70 VILLABLANCA, R and PAREDES, R. (1983). C-9. Efecto de tsunamis cercanos en bahías de Concepción y San Vicente. *in* CASSIS, J.; ASTROZA, M. and YAÑEZ, F. (eds.). *Coloquia '83, VII Simposio Panamericano de Estructuras*. Vol. 2. Universidad de Chile, Santiago.

71 WILSON, B. and TORUM, A. (1968). The tsunami of the Alaskan earthquake, 1964: engineering evaluation. U.S. Army Corps. Eng. Coastal Eng. Res. Cent. Tech. Memo 25: 401 p.

WEB SITES

72 DEPARTAMENTO DE CLIMA MARÍTIMO - PUERTOS DEL ESTADO, ESPAÑA. *Modelos*. <http://www.puertos.es/Modelos/props.html>(accessed 28TH September 2000)

73 NATIONAL EARTHQUAKE INFORMATION CENTER WORLD DATA CENTER. <http://wcatwc.gov/message.txt> (accessed 11TH November 2000).

74 NASA. *Tsunami, the big wave.* <http://observe.ivv.nasa.gov/nasa/exhibits/tsunami/tsun_bay.html> (accessed 30TH January 2001).

75 OXIQUIM. *Terminal Marítimo Oxiquim S.A. – Bahía de Quintero.* <http://www.oxiquim.cl/areas/terminal/ter_tbq.htm> (accessed 21RD October 2001).

76 SERVICIO HIDROGRÁFICO Y OCEANOGRÁFICO DE LA ARMADA DE CHILE (2000). Valparaíso, Chile. <http://www.shoa.cl> (accessed 14TH September 2000).

77 UNIVERSITY OF WASHINGTON, Geophysics Department (2000). *Tsunami.* <http://www.geophys.washington.edu/tsunami/welcome.html> (updated on 8 June, 2000, accessed 26TH September 2000).

78 USA NATIONAL OCEANIC AND ATMOSPHERIC ADMINISTRATION, NOAA. *Tsunami Research Program.* <http://www.pmel.noaa.gov/tsunami/> (accessed 26TH September 2000).

DATE DUE

GAYLORD No. 2333 PRINTED IN U.S.A.

memoria, carta de Inundación en la Bahía de Quintero A-0187 -

DATE	ISSUED TO

memoria carta de Inundación en la Bahía de Quintero

A-0187

GAYLORD S